ANALYSIS AND DESIGN OF ANTENNA PROBES FOR DETECTION / IMAGING APPLICATIONS

AYMAN ELBOUSHI

A THESIS

IN

THE DEPARTMENT OF

ELECTRICAL AND COMPUTER ENGINEERING

PRESENTED IN PARTIAL FULFILLMENT OF THE REQUIREMENTS

FOR THE DEGREE OF DOCTOR OF PHILOSOPHY

CONCORDIA UNIVERSITY

MONTREAL, QUEBEC, CANADA

August 2014

CONCORDIA UNIVERSITY
SCHOOL OF GRADUATE STUDIES

This is to certify that the thesis prepared

By: Ayman Mohamed Fekri ElBoushi

Entitled: Analysis and Design of Antenna Probes for Detection/Imaging Applications

and submitted in partial fulfillment of the requirements for the degree of

Doctor of Philosophy (Electrical & Computer Engineering)

complies with the regulations of the University and meets the accepted standards with respect to originality and quality.

Signed by the final examining committee:

_____ Chair
Dr. S. Bergler

_____ External Examiner
Dr. M.C.E. Yagoub

_____ External to Program
Dr. A. Youssef

_____ Examiner
Dr. T.A. Denidni

_____ Examiner
Dr. R. Paknys

_____ Thesis Supervisor
Dr. A. R Sebak

Approved by: _____
Dr. A.R. Sebak , Graduate Program Director

July 21, 2014

_____
Dr. C. Trueman, Interim Dean
Faculty of Engineering and Computer Science

Abstract

Analysis and Design of Antenna Probes for Detection / Imaging Applications

Ayman Elboushi, Ph.D.
Concordia University.

As a result of increasing international terrorist threats, the need for an efficient inspecting tool has become urgent. Not only for seeing through wall applications, but also to be employed as a safe human body scanner at public places such as airports and borders. The usage of microwave and millimeter wave antennas and systems for detection / imaging applications is currently of increasing research interest targeting the enhancement of different security systems. There are many challenges facing researchers in order to develop such systems. One of the challenges is the proper design of a low cost, reduced size and efficient antenna probe to work as a scanning sensor.

In this thesis, two different technology choices of antenna probes for the feasibility of constructing detection / imaging systems are investigated. The first one covers the Ultra Wide Band (UWB) range (3.1 GHz to 10.6 GHz), while the second operates over the Millimeter-Wave (MMW) range. In addition to the development of several antenna probes, two detection / imaging systems are demonstrated and showed reasonably accurate detection results.

Three different UWB monopole antenna prototypes, with different radiator shapes (circular, crescent and elliptical) have been introduced. These antennas are designed using a standard printed circuit board (PCB) process to work as probing sensors in a proposed UWB detection / imaging system. In order to enhance the resolution and the detection

accuracy of the probe, 4-element Balanced Antipodal Vivaldi Antenna (BAVA) array fed by 1-to-4 UWB modified Wilkinson power divider has been developed. Some successful experiments have been conducted using the proposed UWB detection / imaging system combined with the fabricated antenna probes to detect the presence of a gap between two walls made of different material types, to evaluate the gap width and to estimate the size and exact location of a hidden target between the walls.

The second research theme of this thesis is to develop small-sized, light-weight and high gain MMW scanning antenna probes. For the realization of such probes, several gain enhancement techniques have been adopted, including hybridization and a multi-element array principle. Several high-gain hybrid antennas have been designed, fabricated and tested. For demonstration purposes, experiments have been carried out for detecting and imaging a small metallic coin under the jeans layer of a three-layer target emulating a human body's covering layers. A performance comparison between a standard metallic MMW horn and hybrid microstrip patch/conical horn antenna has been made. The proposed reduced size antenna sensor shows increased efficiency compared with the bulky horn antenna.

Resolution enhancement of the reconstructed image of the hidden target is implemented using a new triple-antenna MMW sensor. The triple-antenna sensor consists of three adjacent microstrip patch / conical horn antennas separated by 1.5 wavelengths at the center frequency for coupling reduction between these elements. The middle element of the sensor is used for monitoring the time domain back-reflected signal from the target under inspection, while the side elements are used for monitoring the scattered signals. By the aid of a special signal processing algorithm, an enhanced image of the concealed object

can be obtained by combining the three readings of each point in the area under study. The proposed system shows a great ability for detecting a hidden target and enhances the reconstructed image resolution.

Acknowledgement

All my thanks to God, for the successful completion of this work.

I express my deepest gratitude and thanks to Prof. Dr. A.R. Sebak for his continuous supervision and generous support. Prof. Sebak is behind all analytical, technical and even spiritual actions throughout this work. Without his encouragement, the thesis could not reach this level.

Besides my advisor, I would like to thank Prof. Dr. Tayeb Denidni for his encouragement, help, and support.

I would like to express the deepest appreciation to my colleagues in the microwave group for their help.

Special thanks also to Mr. Jeff Landry for his technical support in circuit fabrication.

I would like also, to offer my special thanks for my mother, and father for their great hearts which looked after me all these years.

Last but not least many thanks to my wife Rehab, who always encourages me for further progress, also, my lovely kids Youssef and Yehya,

Table of Contents

LIST OF FIGURES

LIST OF TABLES

LIST OF SYMBOLS

λ	Wavelength.
Ω	Ohms.
θ	Elevation angle.
ϕ	Azimuth angle.
λ_o	Wavelength in free space.
Δ	Image resolution (azimuth resolution).
ε_o	Permittivity of free space, 8.854×10^{-12} F/m.
ε_r	Relative permittivity of the medium.
δ	Image resolution.
Γ	Reflected signal.
ΔL	In-depth resolution (range resolution).
B	Bandwidth.
c	The speed of electromagnetic waves in vacuum (299792458 m/s).
d	Tunnel width.
dB	Decibels.
f_o	The resonant frequency.
GHz	Gigahertz, 10^9 hertz.
h	Substrate thickness.
L_a	Synthetic aperture length.
L	Length of the substrate.
L_{50}	50Ω microstrip line length.

N	The number of the antenna elements.
R	Distance from center of effective aperture to imaging target.
S_{11}	Reflection coefficient, expressed as an S parameter.
T	Transmitted signal.
Δt	Time difference between the second and third reflected signals.
$tan\delta$	Loss tangent.
THz	Terahertez, 10^{12} hertz.
T_i	Estimated propagation time.
V	Overall received signal.
W	Width of the substrate.
W_{50}	50Ω microstrip line width.
w_i	Weighting factors.
$y_i(t)$	Received signal from a single antenna.

LIST OF ABBREVIATIONS

1D	One-Dimensional
2D	Two-Dimentional
3D	Three-Dimensional
ABOSCA	ABbildender BOdenSCAnner
ADS	Advanced Design System
BAVA	Balanced Antipodal Vivaldi Antenna
BW	Bandwidth
CAD	Computer Aided Design
CSTMWS	Computer Simulation Technology Microwave Studio
DR	Dielectric Resonator
DRA	Dielectric Resonator Antenna
DUT	Device Under Test
EBG	Electromagnetic Bandgap Structure
EM	Electro-magnetic
FCC	Federal Communication Commission
FDTD	Finite Difference Time Domain
FEM	Finite Element Method
FIT	Finite Integration Technique
GPR	Ground Penetrating Radar
GO	Geometrical Optics
HEM	Hybrid Electromagnetic

HFSS	High Frequency Structure Simulator
IEEE	Institute of Electrical and Electronics Engineers
IFFT	Inverse Fast Fourier Transform
ISAR	Inverse Synthetic Aperture Radar
LPAS	Laborsystem zur Personen-Abbildung mit Scanner
LTR	Late Time Response
MMW	Millimeter-Wave
NDE	Non-Destructive Test
PCB	Printed Circuit Board
PMMW	Passive Millimeter Wave Imaging
PNNL	Pacific the Northwest National Laboratory
RF	Radio Frequency
SAR	Synthetic Aperture Radar
SIW	Surface Integrated Waveguide
TDR	Time Domain Reflectometry
TM	Transverse Magnetic
TTD	True Time Delay
TWI	Through Wall Imaging
TWMI	Through Wall Microwave Imaging
UWB	Ultra-Wideband
VNA	Vector Network Analyzer
VSWR	Voltage Standing Wave Ratio

Chapter 1

Introduction

1.1 Introduction

Microwave detection / imaging [1] is a well-known technique using Electromagnetic (EM) waves at microwave frequencies (300 MHz – 300 GHz) for detecting the internal or external structure of an object and to provide images according to the electrical properties of the object under study. The majority of the electromagnetic spectrum can be used for imaging with different operating frequencies, providing different information about the object being imaged.

A very wide range of applications for the microwave detection / imaging arises in this era which encourages many researchers to exert more effort to develop different antenna sensors to be integrated in various detection / imaging systems. These applications include:

a. *Medical and healthcare*: microwave imaging could be used instead of traditional X-rays for early diagnosing some types of cancer especially breast cancer. Microwave imaging is recommended for such applications not only for having zero level of ionized radiation that may be considered as a health risk on the patients, but also for its superior ability for detecting a very small tumor (less than 3mm) [1].

b. *Security*: the increasing demand for monitoring concealed weapons and explosives with the passengers at the airport gates has led to the potential use of microwave imaging as a very suitable tool for this purpose where scanning and surveillance of people cannot use ionizing radiation for safety reasons. Also, the current metal detection solution is

limited as it cannot see underneath clothing and it cannot detect the plastic explosives (e.g. C4 & RDX) or the non-metallic guns.

c. *Defense*: Ground Penetrating Radars (GPRs) are widely used for detecting buried mines and ammunitions in the battlefields.

d. *Space and remote sensing*: Synthetic Aperture Radar (SAR) is used to draw some images for the earth and other planets. (SAR) technique based on transmitting multiple radar pulses then receiving them at different locations and different later times. They are processed together to yield images of mostly stationary scenes with higher resolution than could be possible with conventional beam-scanning means.

e. *Through Wall Microwave Imaging (TWMI)*: microwave imaging can be used in securing buildings in which hidden tunnels and vacancies behind walls could be detected and to monitor any sign of life in collapsed buildings after earthquakes and natural disasters.

1.2 Brief Overview of Microwave Detection / Imaging Scanning Probes

The scanning antenna probe is the core component for any detection / imaging system. Therefore, designing an efficient antenna sensor should take the first priority through detection / imaging system development. Although antenna sensors may have different application, shape, and operating frequency, there are some general characteristics should be satisfied by all of them. These characteristics can be summarized as high and stable gain over the operating band, directional radiation, good impedance matching over the operating band (i.e. S_{11}< -10 dB), low metallic losses, high radiation efficiency, compact size, easy for fabrication, and small group delay (less than 2 ns) and minimal time domain distortion especially for Ultra Wideband (UWB) antenna probes.

1.3 Brief Overview of Microwave Detection / Imaging Systems

Microwave imaging systems can be classified according to many common characteristics including:

i. Nature of scanning

a. Active system: the target is illuminated by an external electromagnetic pulse(s) in different locations, then the image is constructed by detecting the scattered waves from the target.

b. Passive system: the image is constructed by detecting the emitted electromagnetic radiation from the targets, where the radiation emitted by bodies or things complies with a continuous spectrum known as black body radiation.

ii. Operating frequency

a. UHF (less than 3 GHz), usually this range is used for high penetrating imaging systems (e.g. GPR); standard radio frequency (RF) segments are shown in Table 1.1.

b. UWB (3.1-10.6 GHz), this range is widely used in medical applications for its ability to go through the human skin. Also this range is suitable for many security applications including through wall microwave imaging (TWMI) for detecting hidden tunnels and hiding persons behind walls.

c. Millimeter wave (MMW) (30 GHz- 300 GHz) "EHF", very suitable for security applications (e.g. hidden weapons detection) where the radiated EM wave cannot penetrate the human skin.

d. Terahertz (300 GHz- 3THz) "THF", used in some security applications detecting very small metallic objects concealed on people such as miniature explosives. Also, due to High resolution images produced by using this range, it is very suitable for remote

sensing applications like creating high quality images of the surface of the earth and other planets.

Table 1.1 Standard radio frequency bands.

Name	*Frequency Range*	*Applications*
Low Frequency (LF)	30 KHz-300 KHz	Time standards, Navigation
Medium Frequency (MF)	300 KHz-3 MHz	AM radio
High Frequency (HF)	3 MHz-30MHz	Amateur radio
Very High Frequency (VHF)	30 MHz-300 MHz	FM/TV broadcasting
Ultra High Frequency (UHF)	300 MHz-3 GHz	Cell phones, WLAN, GPR
Super High Frequency (SHF)	3 GHz-30 GHz	Satellite, 5G mobile
Extremely High Frequency (EHF) "MMW"	30 GHz-300 GHz	Imaging / detection applications, 5G mobile
Tremendously High Frequency (THF)	300 GHz-3 THz	High resolution microwave imaging

iii. Antenna arrangement

a. Monostatic type (reflection type)

In this configuration, the same antenna is used for both transmitting and receiving a microwave signal, i.e. the transmitter performs the function of a reflectometer. The monostatic system configuration is shown in Fig. 1.1.

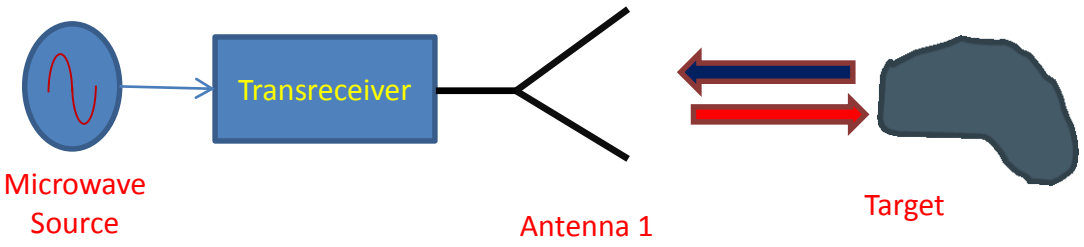

Figure 1.1 Monostatic system configuration.

b. Bistatic type (transmission-reflection type)

In this configuration, the system uses two antennas, which are displaced by some distance. Sometimes numerous antennas are used for receiving the transmitted signal from one transmitting antenna. The bistatic system configuration is shown in Fig. 1.2.

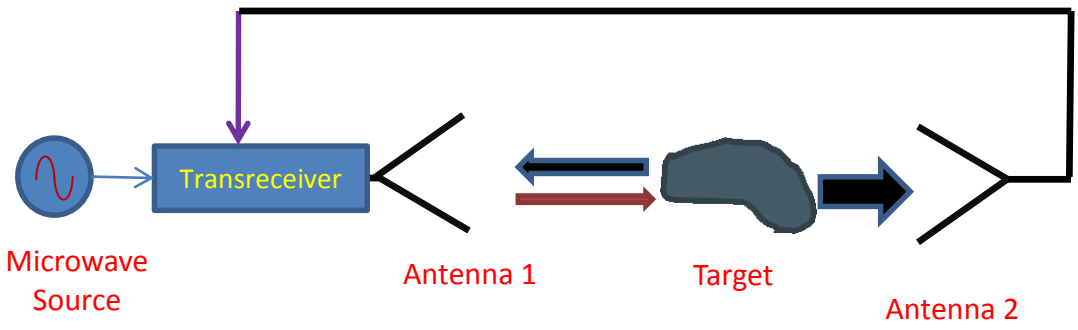

Figure 1.2 Bistatic system configuration.

1.4 Motivation

Recently, many research efforts have been exerted for developing modern microwave detection / imaging systems for homeland security and other applications.

In this thesis, two distinct detection applications from an operating frequency band point of view will be explored. The distinction is made between through wall and long range on one hand using UWB sensors and short range screening of people using MMW sensors on the other hand.

UWB technology has been used for some time in GPR applications [2], [3] and early breast cancer detection [4], [5]. Recently, as a new trend, it is used to help police to detect the existence of any hidden tunnels or hidden people behind walls [6], [7]. The UWB range (3.1 GHz – 10.6 GHz) [8] is chosen as operating band for such imaging / detection

systems because the informational content of the UWB imaging systems increases due to the smaller pulse volume of the signal. For example, when the length of a sounding pulse changes from 1 μs to 1 ns, the depth of the pulse volume decreases from 300 m to 30 cm [9]. In this case, the imaging system instrument probing the surveillance space becomes finer and more sensitive. So this reduced signal length may increase the informational content, increase the probability of target detection, improve detected target range measurement accuracy, enhance the penetration of optically opaque materials (e.g. concrete and wooden walls) and reduce the effects of passive interference from rain, mist, aerosols, metalized strips, etc. This is because the scattering cross section of an interference source within a small pulse volume is reduced relative to the target scattering cross section [9].

The deployment of such UWB detection systems requires antennas with ultra-wideband performance. Designing an antenna to cover the entire ultra-wideband range and to work as a scanning element is considered a great challenge. A UWB antenna should be operated over the entire UWB frequency range. It should be capable of achieving high impedance matching bandwidth of 7.5 GHz. In addition, it should have a small group delay (not more than 2 ns) and a linear phase over the operating bandwidth. For increasing the penetration capability of EM waves through thick and lossy (conductive) walls, more directive antenna sensor is required. Many techniques can be adopted to enhance the overall antenna probe gain. In addition, the sensor cost, weight and size should be taken into consideration in the design process. These sensors are intended to be used later as a replacement of heavy metallic UWB horn sensors without any sacrifice of the detection level accuracy. One of the possible approaches is using high gain and low-profile elements

like Tapered Slot Antennas (TSA) or applying array technologies to enhance the overall gain of the scanning antenna.

Detection of concealed weapons, knives, and guns in public spaces is becoming increasingly relevant in the field of policing and security. Although metallic detectors, presented for the first time in 1920 by Fisher [10], can be considered as an efficient tool for detecting hidden metallic weapons, it fails to detect non-metallic weapons and modern plastic explosives. An effective non-ionizing imaging system becomes highly attractive. A MMW imaging system is considered a potential candidate for doing this job. MMW-based imaging systems have good characteristics, including high penetration ability of different types of clothes, very low penetration for living tissues, less physically intrusive upon human and using safer non-ionizing radiation. These systems could be used instead of traditional X-rays systems which have ionizing radiation, and a limited usage per person. Active and passive scanning systems are considered as the main technologies for developing MMW human scanning systems. Although a Passive Millimeter Wave Imaging (PMMW) system allows detection of hidden weapons without any need for an RF generator, its use for indoors imaging of concealed weapons under clothing poses a formidable challenge for MMW imagers due to the sub-pico watt signal levels present in the scene. Moreover, video-rate imaging requires a large number of pixels, which leads to a very complex and expensive front end for the imager. Therefore, a small size active scanning system is desired to meet the above concealed weapons detection challenge. MMW antenna design is considered as the first and the most important step for realizing the detection / imaging system. Many MMW antenna sensors have been developed to be integrated within such systems. A flexible printed antenna sensor for crack detection was

presented in [11]. However, it lacks a directive beam which is mandatory for imaging and detection applications. An active corrugated lens antenna sensor, as part of interferometer system, was used in [12], [13] at W-band for homeland security imaging and detection applications. Parabolic dish reflector sensors are employed in the ABOSCA (ABbildender BOdenSCAnner) radiometer, LPAS-2 (Laborsystem zur Personen-Abbildung mit Scanner) radiometer systems [14], [15] and in the passive imaging system presented in [16]. Moreover, 2D multistatic multi-modules sparse array is adopted as human body scanning sensor in Rohde and Schwarz imaging system introduced in [17]. In [18], a 32–element circular array sensor was used in a radar interferometer for topographic imaging in industrial environment in the steel industry. One reported limitation of the system is the crosstalk between the receiving antenna elements. A 2-element microstrip patch antenna array based sensor was adopted in [19] to remotely monitor structural displacements.

Despite the good performance of the former antenna sensors, most of them are characterized by the bulky size, big volume and heavy weight or by the lack of a directive beam which reflects on the overall performance of a MMW imaging system. In this perspective, an efficient, small size and low cost antenna sensor for MMW detection and imaging applications is considered as a critical design requirement.

1.5 Thesis Objectives

This thesis mainly focuses on two distinct aspects from operating frequency band point of view:

(a) UWB detection / imaging for tunnel detection, gap estimation and Through Wall Microwave Imaging (TWMI) as a tool for securing buildings form any suspected human beings / object presented behind the wall.

(b) MMW detection / imaging of hidden targets, including weapons, knives and explosives concealed by the passengers at the inspection gates.

The main objective of the first research aspect will be addressed through the design, optimization, fabrication and testing of different UWB antenna probes and study their geometrical shapes and operation mechanism that lead to desired UWB characteristics. As a secondary objective and proof of concept, the fabricated antenna probes will be used as a scanning element in a detection / imaging system. In order to examine the designed probes performance, multiple practical experiments will be conducted. Some of these experiments will be done on various types of wall materials for hidden tunnel "gap" detection and its width estimation. Moreover, another experiment will be carried out to detect the exact location of a hidden metallic ball, and plot its approximate shape.

For the second research aspect, multiple hybrid high gain MMW antenna sensors will be designed and fabricated. Hybrid configurations will include patch / waveguide, patch / horn, patch / DRA, slots / horn and patch / superstrate. All the realized antenna elements should be characterized by a small size, low cost and light weight. Similar to the UWB work and as a proof of concept, fabricated antenna probes will be used as elements in MMW scanning systems for hidden target detection / imaging applications. The experiments will include comparative studies between the standard horn antenna and some of proposed antenna probes. In addition, to enhance the detection / imaging sensitivity a triple antenna sensor will be introduced. The sensor consists of three adjacent high gain

microstrip/horn hybrid antenna elements. The central antenna acts as bistatic radar, while the two side antennas are used to receive the scattered back signals from a hidden object.

1.6 Organization of the Thesis

This thesis is organized in seven chapters as follows:

Chapter 2 provides a literature review and background introduction to UWB, MMW antenna probes and imaging system operation principles. In Chapter 3, we discuss the theoretical background and associated methodology of the proposed work. The chapter also focuses on the design procedure and the governing equations of some techniques used for antenna probes design. These techniques include SIW, DRA, hybrid configurations and a brief discussion about the numerical techniques used in the simulation software. The implemented UWB antenna probes results are presented and discussed in details in Chapter 4. Two types of UWB antenna sensors are introduced; slot-coupled UWB and high gain BAVA array. In Chapter 5, different MMW antenna probes are presented. Multiple gain enhancement techniques are studied to achieve an optimal scanning antenna probe. UWB and MMW detection / imaging experimental results are presented and discussed for several scenarios in Chapter 6. Finally, Chapter 7 presents the overall conclusion and main contributions of this research followed by suggestions for future work.

Chapter 2

Literature Review

2.1 Introduction

Microwave imaging field is not a new research topic since it has been used for some time in a different application areas. Synthetic Aperture Radar (SAR) [20]-[22], Inverse Synthetic Aperture Radar (ISAR) [23], Time Domain Reflectometry (TDR) [24], and Ground Penetrating Radar (GPR) [25]-[27] are such classical examples. Recently, microwave imaging has received a considerable amount of interest compared with other imaging techniques. It has a wide range of applications including remote sensing, Non-Destructive Testing (NDE) for materials [28], medical tests as well as Through Wall Microwave Imaging (TWMI) [6], [7] and other security applications. In this thesis, we will revisit the problems associated with TWMI for hidden tunnel detection and other important imaging applications of concealed weapons detection in public places. According to the nature of each imaging system, two different frequency bands will be used. The UWB range (3.1-10.6 GHz) is considered as a good candidate for a TWMI system, while the MMW range (28-32 GHz) is chosen for short range hidden weapons detection system. The greatest challenge for such systems realization is the antenna sensing probe. Many detection /imaging systems available in the market utilize expensive bulky metallic probe antennas, which result in heavy, costly and large scanning systems. In addition, these systems suffer from long scanning time due to the slow mechanical scanning systems.

To overcome these problems, novel, high efficient, low profile and low cost scanning antenna elements should be designed. Also, an efficient mechanical scanning

system should be investigated for enhancing the overall scanning time of the imaging system. These issues will be the backbone of this proposed research.

This chapter presents a brief survey about different antenna sensor types used for detection / imaging applications and explaining briefly the working principles of some practical detection / imaging systems.

2.2 Microwave Imaging Systems

In this section we will focus on the principles of some well-known microwave imaging systems, including SAR, ISAR, GPR and TWMI.

2.2.1 SAR and ISAR Systems

Synthetic Aperture Radar (SAR) [20]-[22] can be defined as a type of imaging technique whose defining characteristic is its use of relative motion between an antenna and its target region (which is stationary) to provide distinctive long-term coherent-signal variations that are exploited to obtain finer spatial resolution than is possible with conventional beam-scanning means, where pulses of microwave signals are sent from airborne radar to ground and received during its movement. By taking a large number of echo signals, an image of the ground in terms of its reflectivity can be produced [20]-[22]. The image resolution δ depends on the synthetic aperture L_a, distance from center of effective aperture to imaging target R and the wavelength of the probing signal λ as shown in Eq. (2.1) [29]. The factor 2 in Eq. (2.1) is added because the SAR beam is formed by two-way transmission. SAR images have wide applications in remote sensing and mapping of the surfaces of both the Earth and other planets. The image resolution is [29]:

$$\delta = \frac{\lambda R}{2L_a}. \tag{2.1}$$

Inverse Synthetic Aperture Radar (ISAR) has the same principles of operation as SAR except the observation of a moving target over a substantial time is done with a stationary antenna.

2.2.2 GPR System

Ground Penetrating Radar (GPR) [25]-[27] is a geophysical method that uses radar pulses to image the subsurface. This non-destructive method uses EM radiation in the microwave bands (always UHF or VHF) of the radio spectrum, and detects the reflected signals from subsurface structures. It uses a similar principle of microwave imaging. However the difference is that the scanned surface is usually in the near field region and the objects to be detected are buried under these surfaces. With the GPR there is a particular interest in obtaining a high in-depth resolution, which can help in detecting underground objects such as cracked pipes or land mines [9]. In order to obtain the required in-depth resolution, the transmitted signal has to have sufficiently large bandwidth, as the in-depth resolution is inversely proportional to the bandwidth of the signal. In particular, when the medium is a homogeneous dielectric, in-depth resolution is given by Eq. (2.2) [29].

$$\Delta L = \frac{c}{2B/\sqrt{\varepsilon_r}} \tag{2.2}$$

where c is the velocity of EM wave, B is the bandwidth and ε_r is the relative dielectric constant of the medium.

2.2.3 TWMI System

Through Wall Microwave Imaging (TWMI) is a classical imaging application for sensing of moving and stationary targets through visually opaque obstacles such as walls [6], [7].

TWMI is considered a powerful tool in both military and commercial applications including the rapid detection of human maneuvering, rescue missions in avalanches or collapsed buildings, target feature extraction, and surveillance and reconnaissance and even sensing through smoke and dust. Besides the TDR technique, many numerical analysis techniques have been employed for through wall imaging, including Geometrical Optics (GO), ray tracing [30], [31] and 2D Method of Moments (MOM) [32]. Narrowband Doppler radar in the millimeter-wave or infrared spectrum has been shown to provide good resolution through clothing and packaging [33]. However, penetration through denser materials like concrete, wood, sheetrock, plaster, brick, and concrete blocks requires operating below 10 GHz [34]-[35]. But working over this band yields poor resolution and limiting applications.

2.3 UWB Probe Antenna

Recently, there has been a great attention paid to ultra-wideband system design and its application not only in imaging purposes, but also in personal wireless communications, especially since the Federal Communication Commission (FCC) released its report in 2002 [8]. There are significant demands for small size antenna elements with broader bandwidth for realizing a practical detection / imaging system. The antenna sensor is considered to be a key component of these systems and it affects its overall performance. There are many challenges for designing UWB antenna includes the ultra-wideband performance of the impedance matching, (i.e. good impedance matching "S_{11}< -10 dB" in the band of 3.1 to 10.6 GHz), small size, minimum distortion, stable radiation pattern, and stable gain. Currently, there are many antenna designs that can achieve broad bandwidth to be used in

UWB systems. These antennas can be grouped into four different categories as 3D volumetric antennas, slot coupled antennas, printed monopole antennas, and frequency independent antennas.

3D volumetric UWB antennas include suspended radiator, mono-cone, bi-conical and DRA based antennas [36]-[40]. Although they have good radiation characteristics, their bulky structure with large physical dimensions limits their possible application. As shown in Fig. 2.1 (a), the design presented in [37] based on a suspended quad tripod kettle antenna (TKA) over a large ground plane. This design realizes quasi-omnidirectional radiation pattern with 70% coverage of the UWB range. Monocone and biconical shaped radiators [38], [39], shown in Fig. 2.1 (b-c), can provide good UWB performance, but with limitation in terms of their fabrication difficulty and large size. A Pawn-shaped dielectric ring resonator (DDR) exited by a monopole antenna [40] provides UWB performance obtained as a result of the multi-resonance of its hybrid monopole-DDR structure.

Unlike patch antennas, slot coupled UWB antennas [41]-[46] possess good characteristics such as wide impedance bandwidth, less copper losses, better isolation …etc. The coupling slot can take many shapes, including elliptical [41], triangular [42], rectangular [43], and circular [45], [46]. The main focus of these slot antenna designs is to enhance the impedance bandwidth using a widened slot and a fork like stub [42], which increases the design complexity.

Planar monopole antennas with different shapes [47]-[53] of polygonal rectangular, triangle, crescent, trapezoidal, circular, elliptical, etc… have been proposed for UWB applications. Due to their wide frequency bandwidth, simple structure, easy fabrication, and stable radiation patterns, planar monopole antennas are considered as promising

candidates for applications in UWB communications. Many modern designs try to add more enhancements in terms of side lobe level (SLL) and the size. EBG based structures [50] can be used to reduce both SLL and the transient distortion. Fractal radiators [51]-[53] are adopted to increase the current path over the radiating monopole and accordingly, reduce the overall antenna dimensions.

Another technique for obtaining UWB performance is by using frequency independent antennas, which include, antipodal Vivaldi [54], [55], log periodic [56], [57] and spiral antennas [58]. An Antipodal Vivaldi antenna is a very good candidate for microwave imaging applications because of its superior directivity and wide bandwidth. Although both log periodic and spiral antennas can operate in the UWB frequency band (3.1-10.6 GHz), they are not suitable for imaging applications because they have large physical dimensions as well as their dispersive characteristics and severe ringing effect [59].

(a) TKA UWB antenna [36].

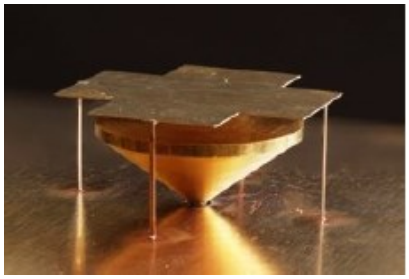

(b) Monocone UWB antenna [37].

(c) Biconical UWB antenna [38].

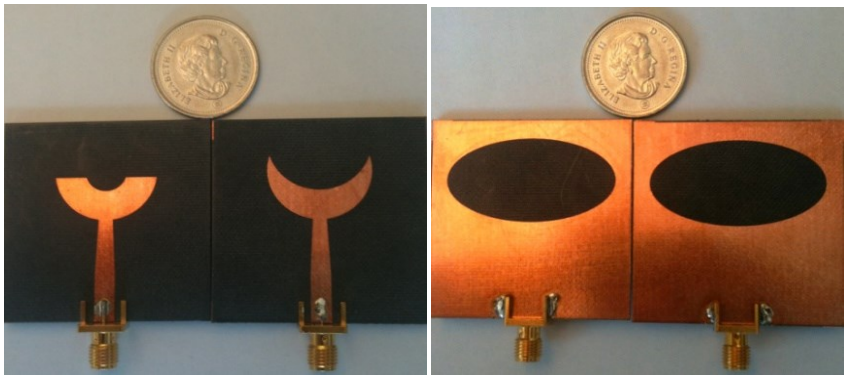

(d) Slot-coupled UWB with different radiator shapes.

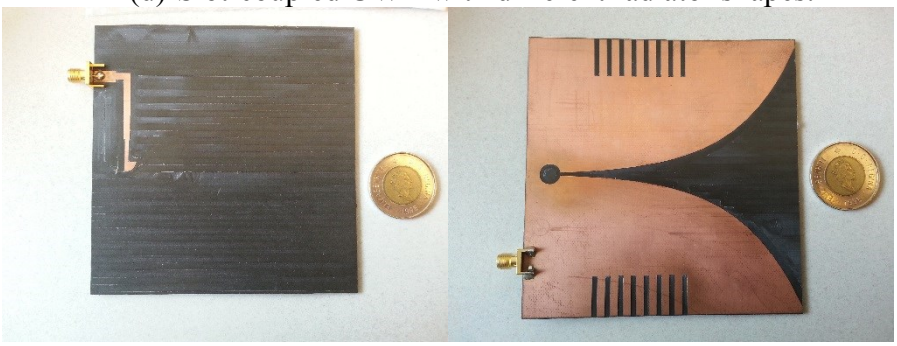

(e) UWB Vivaldi Antenna.

(f) Balanced Antipodal Vivaldi Antenna (BAVA).

Figure 2.1 Various types of UWB antennas.

2.4 Millimeter-Wave (MMW) Antenna Probes

Millimeter-Wave technology is considered as an innovative solution for the next generation of human scanners for concealed weapons detection. It allows high penetration for most

types of clothes (cotton, wool and synthetics), which enhances the image quality. However, millimeter-wave propagation at frequencies around 30 GHz suffer from relatively high propagation losses due to absorption by oxygen molecules in the atmosphere [60]. Accordingly, improving the gain is considered as one of the most important targets in antenna design for such frequencies.

Surprisingly, the first MMW trans-receiver system was presented by Bose [61] in 1879. In his system, shown in Fig. 2.2, he used a metallic pyramidal horn antenna as a receiving antenna. However, working in MMW range stopped after his work for many years. Recently, many different types of antennas have been investigated [62]-[75] for MMW applications such as wireless LANs, microwave imaging and hidden object detection. For realizing such antennas different technologies have been proposed, including metallic horn antennas, metallic waveguides [62], patch antennas [63], dipole antennas [64], [65], DRA-based antennas [66], [67], stacked antennas [68], SIW-based antennas [69], [70], Yagi-Uda based antennas [71], Bow-tie antennas [72], Tapered Slot Antennas (TSA) [73], superstrate based antennas [74], and lens antennas [75]. Some photos of these antennas are shown in Fig. 2.3. Hybrid antennas are considered to be the optimum choice for designing a MMW scanning element, in which it has very good characteristics, including: low profile, low cost, high gain and high efficiency.

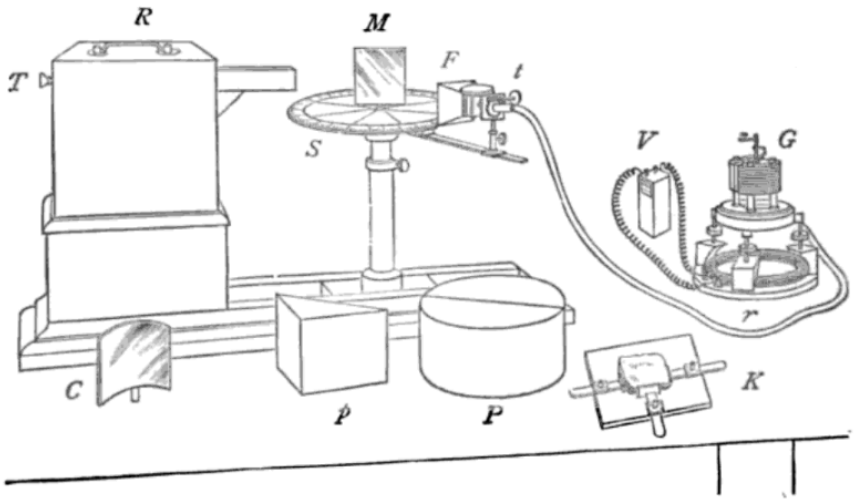

Figure 2.2 Bose's trans-receiver demonstrated to the Royal Institution in 1897 [61].

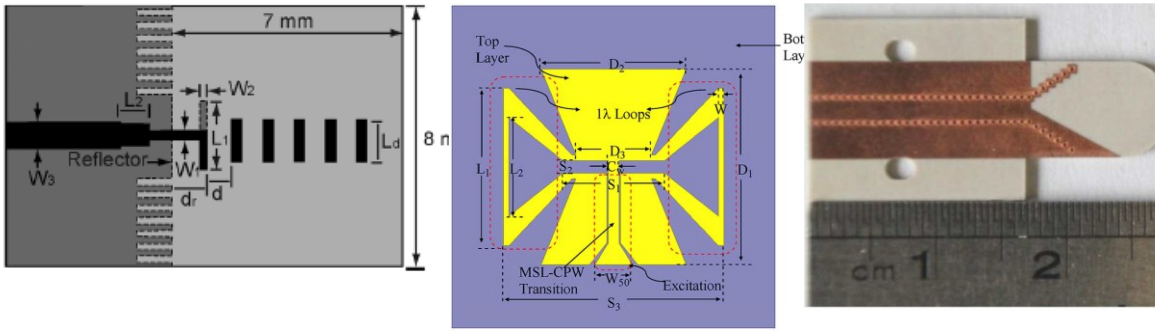

(a) Microstrip-fed Yagi-Uda antenna [71].

(b) Reflector-backed one-wavelength bowtie antenna [72].

(c) Elliptical dielectric-loaded TSA [73].

Figure 2.3 Various types of MMW antennas.

2.5 UWB Imaging

Narrowband signals limit the information capability of imaging systems since the amount of the information transmitted in a unit of time is proportional to the signal frequency band. Accordingly, increasing the system's capacity requires expanding its operating frequency

band. Alternatively, the information transmitting time should be increased. UWB signals are characterized by a bandwidth greater than 500 MHz or one exceeding 20% of the center frequency of radiation [76]. The advent of practical high-speed sampling and pulse generation in recent years, coupled with the approval of the FCC unlicensed band from 3.1-10.6 GHz in 2002, has led to the commercial use of UWB technology in fast-rate communications and precision ranging. These characteristics make the UWB a very good alternative to Doppler radar for TWMI systems. It compensates for the significant drop in the center frequency by boosting the bandwidth which translates into one range resolution. UWB also offers immunity to interference and low probability of interception, in particular for military applications.

2.5.1 UWB Microwave Imaging System with Step-Frequency Synthesized Pulse

The operation principle behind the UWB imaging system, presented in [29], is based on sending a short duration pulse that is synthesized by transmitting continuous wave (CW) signals at equidistant frequencies covering the entire UWB range from 3.1 GHz to 10.6 GHz. The signal is produced by a Vector Network Analyzer (VNA) after proper calibration over the pre-stated frequency range. The time domain representation of the pulse can be obtained by performing Inverse Fast Fourier Transform (IFFT) on both transmitted and received signals. The synthesized pulse resulting from a signal having a constant magnitude in frequency domain, which is lunched in the direction of the target, is shown in Fig. 2.4. The previous principle is used by Khor et al. [29] for building a complete UWB imaging system for breast cancer detection, where the experimental setup, shown in Fig. 2.5, consists of a circular cylindrical plastic container with a diameter of 12.5 cm with thickness of 1 mm. The container can be filled with air or liquid dielectric. A solid material

representing a target can be located inside the container. Other solid dielectric material like rubber can be put around the container to represent, for example, a lossy skin layer.

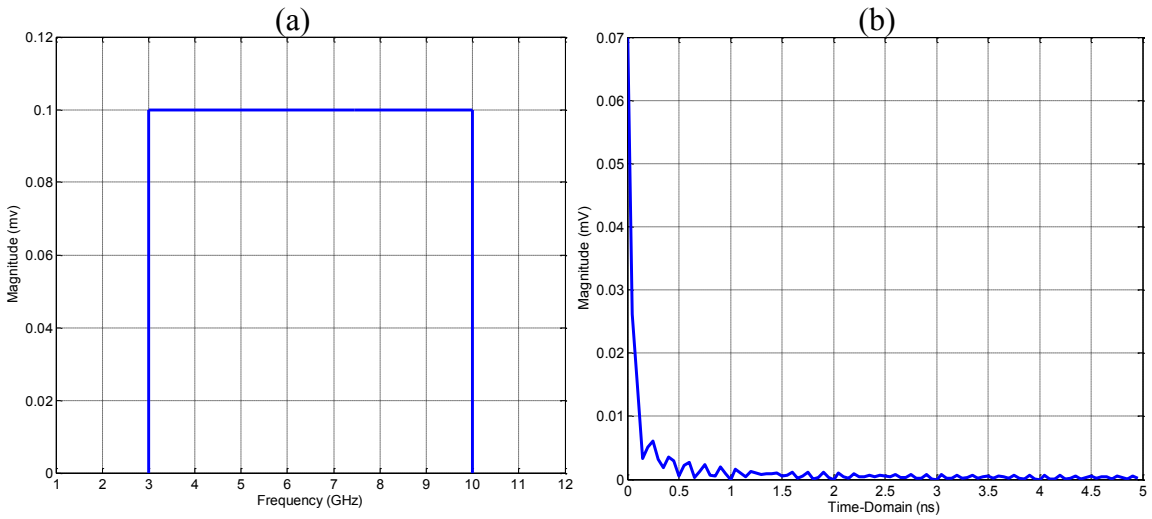

Figure 2.4 Synthesized pulse (a) Frequency domain (b) Time domain.

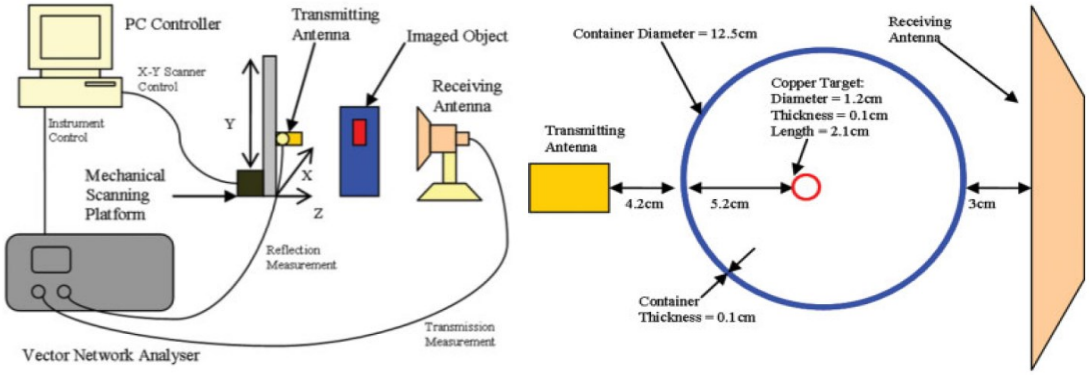

Figure 2.5 Configuration of the experimental setup [29].

Figure 2.6 shows the reflection coefficient in the time domain for a single position of the scanning antenna probe when it is centrally located in front of the plastic container [29]. The first reflection at time zero is due to the coaxial – to – rectangular waveguide transition. The second peak is due to the internal reflection at the junction between the rectangular to the circular waveguide end. The third peak in Fig. 2.6 is due to the reflection

occurring at the end of the coaxial waveguide. Also, it is clear that the fourth peak is due to the first plastic interface and the fifth one is due to the copper target.

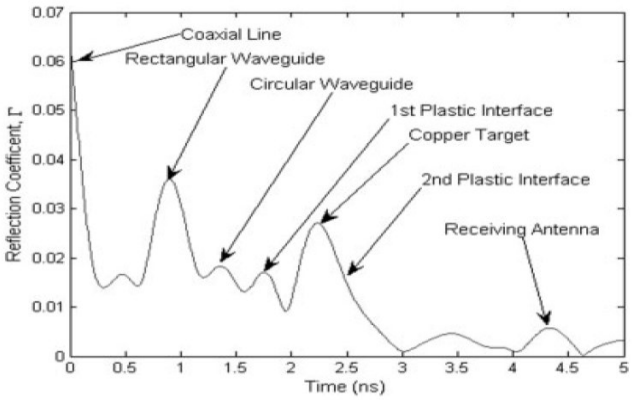

Figure 2.6 Reflection coefficient vs. time for the previous configuration [29].

The idea of using a stepped Frequency Synthesized Pulse can be used in many other imaging applications like TWMI and some security application includes ceiling mounted antenna arrays for security scanning without interfering with the movement of people.

2.5.2 Delay-and-Sum UWB Imaging System

Delay-and-sum imaging system [77] uses multiple antennas for receiving and transmitting, in which every time just one antenna works as a transmitter while the others work as receivers that can be done by attaching a switching circuit to the antenna array system. After converting the frequency domain received signals $Y_i(F)$ to a time domain signals $y_i(t)$, where i is the antenna number. A simple delay-and-sum applied, where the recorded data are synthetically focused at any point of interest in the volume, as shown in Fig. 2.7, by time-aligning the received signals $y_i(t)$ using the estimated propagation time T_i from the transmit antenna a to the receive antenna b via the point of interest c. The return from c is then computed by integrating the data over a window corresponding to the transmit pulse width. The overall received signal at a point c can be evaluated by [77]:

$$V = \int_0^{\tau} \left(\sum_{i=1}^{N(N-1)/2} w_i y_i (t - T_i) \right)^2 dt \tag{2.3}$$

where w_i are the weighting factors that are applied to compensate for differences in the predicted attenuation between the round-trip paths (depending on the depth of point c and the spacing from antenna a to antenna b). Assuming that we have 16 antennas, there are 120 unique bistatic signals which give considerable immunity to clutter, certainly far more than a monostatic approach.

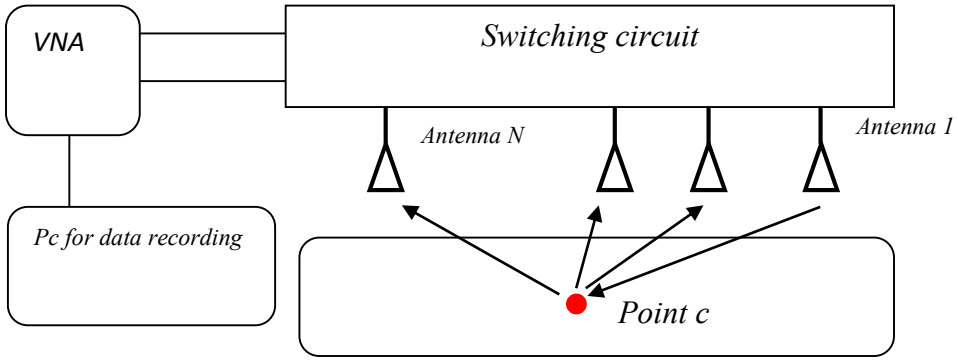

Figure 2.7 Delay-and-Sum imaging system.

2.5.3 Commercial UWB Detection / Imaging Systems

In the last few years, multiple TWMI systems have been introduced in the market. The main objective of these systems is to serve as an early warning tool providing quick location of people hidden by barriers and walls, enabling tactical troops and rescue teams to step into the known and obtain the required information about the targeted location. As shown in Fig. 2.8, three different TWMI system are introduced. The reconstructed images can be displayed on a separate LCD monitor module as in Xaver 800 [78], or mounted on the transmitting / receiving system as in Prism 200 [79] and Soldier vision system [80].

(a) Xaver 800 TWMI system [78].

(b) Prism 200 through-wall radar system [79].

(c) Soldier vision system [80].

Figure 2.8 Commercially available TWMI systems.

2.6 MMW Imaging

The increasing number of terrorist attacks has drawn attention to the development of new imaging technologies for wide area surveillance as well as for the detection of concealed dangerous objects and weapons. Many systems were developed for hidden weapon detection starting with metal detectors, which are not very efficient tools for detecting non-metallic weapons and plastic explosives. In addition, some microwave detectors based on polarized Late Time Response (LTR) [81], which use the complex resonances excited by illuminating the target with a microwave pulse, is not applicable in the case of non-metallic weapons. Nowadays, there is a new trend of using MMW-based imaging devices for concealed weapons detection. MMW imaging systems offer great penetration capability which provides accurate detection of objects through atmospheric obstacles like bad weather, fog or dust, vapor and smoke, as well as through thin non-metallic materials and clothing. In the meantime, it does not penetrate human skin. Table 2.1 shows the electrical properties of some human tissues at 30 GHz [82], while Table 2.2 shows the transmission and attenuation of some clothing materials. As indicated in [83] there is an uncertainty in

the measurements around 40 GHz, that leads to errors of the order of 3 to 7% as the frequency increases. This produces the attenuation values above 0dB and transparency over 100%. For the latter the detection of hidden objects like weapons, explosives, and contraband is possible by monitoring dielectric anomalies.

Table 2.1 The electrical properties of some human tissues at the frequency of 30 GHz [82].

Tissue Name	Conductivity [S/m]	Relative Permittivity	Loss Tangent
Muscle	0.65803	91.812	4.2944
Fat	0.033246	8.1106	2.4561
Dry Skin	0.34168	152.94	1.3386
Wet Skin	0.43444	108.33	2.4028

Table 2.2 The transmission and attenuation of some clothing materials [83].

Transmission / attenuation	40 GHz		90 GHz	
	dB	% Trans	dB	% Trans
Embroidered cotton	0.1	103	-0.4	92
Jeans	0	99	-0.7	84
Rain coat	0.2	106	-0.5	90
Wool	-0.1	96	-0.1	96

2.6.1 Passive vs. Active MMW Imaging

Two major techniques used for the realization of MMW imaging systems. The first technique is passive MMW imaging (PMMW), which depends on the fact that all bodies emit electromagnetic radiation. The radiation emitted by bodies, complies with a continuous spectrum, is known as the black body radiation. The intensity of the radiation depends on the temperature of the body and also very critically on how effectively the body radiates. This effectiveness, emissivity is close to one for a water-containing material such as a skin. On the other hand, metals have an emissivity which is very close to zero. All other materials lie between these extremes and can be observed according to the

radiometric temperature thereof. By receiving these radiations we can plot an image of the target showing any abnormality around a body, so there is no need for an external EM source. PMMW systems were developed in the 1950s for military applications and the first reported use of this technology for security screening was by Barker in 1975 [84]. The second MMW imaging technique is active MMW imaging [12], [13], which depends on illuminating the human body with an EM pulse generated by an external source. The incident wave, e.g. planar or spherical is supposed to produce a scattered field which can be thought of as being generated by secondary sources located within and on the surface of the object. The distribution of the scattered field is measured by the imaging system to an extent which depends on the imaging system.

2.6.2 Passive MMW Imaging Systems (PMMW)

The ABOSCA system, presented in [14], [15], is considered as far-field scanner and it is based on passive imagining approach where the imaging process is dependent on measuring the natural thermally caused electromagnetic radiation of a matter at temperature higher than 0 K. The system is capable of scanning a complete hemisphere. Although this system is more immune for atmospheric impacts like humidity and rain, it is considered as very large, heavy and power consuming scanning system and not suitable for high-resolution imaging of persons.

The LPAS-1 system and its upgrade LPAS-2 [14], [15], are mainly designed for near field scanning as a detecting tool for the concealed weapons in a range of 2.5 m to 3 m, in which it is based on passive imaging approach. LPAS-2 has better image sensitivity compared with LAPS-1, and faster scanning time, where it just requires 27 s to complete the image.

2.6.3 Active MMW Imaging Systems

The Munchen University MMW imaging system, presented in [85], [86], was fabricated in 2004. It is based on a monostatic radar principle for detecting weapons and other non-metallic explosives. This system utilizes the active approach where the system illuminates the scanned object by 89-99 GHz microwave signal with a frequency increment of 100 MHz and frequency sweep time of around 15 s. Although good imaging quality for the suspected objects produced by this system, it requires a very high precision mechanical moving system.

The wideband holographic MMW System , illustrated in [87], was developed at Pacific National Laboratory (PNNL).This system can be used for detecting concealed metal or plastic weapons also it can detect all kinds of new explosives like (C4 and RDX). This system is based on an active scanning approach where the scanned target is illuminated by a wideband MMW pulse, then at each point over the 2-D aperture of the system. Coherent wideband data (phase and magnitude) reflected from the target is collected using wide-beamwidth antenna array and after that the received data is focused by using an image reconstruction algorithm in order to obtain a full 3-D image. The operating frequency of this system is between 27-33 GHz. In order to complete the scanning process the 128 element array is mechanically swept over a vertical aperture of 2 m.

The Active MMW Imaging System, elaborated in [88], is based on a planar multistatic sparse array design utilizing a digital-beamforming (DBF) technique. The system employs a sparse array for an exceptional reduction in the used number of RF

modules, without any sacrifice of the imaging details. The system was designed and verified from 72 to 80 GHz and demonstrated lateral resolution down to 2 mm.

2.6.3 Commercial MMW Detection / Imaging Systems

Many countries all over the world started in using MMW imaging systems for passenger scanning at the airports. As an example of these widely used systems, there is the GEN-2 passive imaging system [89] and Pro-Vision MMW imaging system [90]. These systems provide good quality images for any hidden objects behind the clothes. The scanning time of these systems can be as short as 1.5 s, as in the case of Pro-vision system. Actual photographs of these systems are shown in Fig. 2.9.

GEN-2 passive imaging system [89].

Pro-Vision MMW imaging system [90].

Figure 2.9 Commercially available MMW imaging systems.

2.7 Summary

In this chapter, a brief survey explaining different working principles of some practical detection / imaging systems is introduced. In addition, a literature review of various types

of antenna sensors used for detection / imaging applications is presented. Finally, both UWB and MMW imaging basics are discussed.

Chapter 3

Theoretical Background

3.1 Introduction

This chapter will focus mainly on the methodology and the theoretical background required for designing high performance antenna elements. Section 3.2 explains how the antenna radiated fields are estimated using Maxwell's equations. Section 3.3 introduces some basic antenna parameter definitions. Section 3.4 introduces the SIW structure showing its advantages and disadvantages compared with an ordinary metallic waveguide. Design equations and restrictions related to SIW structures will be discussed. Section 3.5, a brief discussion about the operation basics of metallic conical horn antennas will be introduced. In Section 3.6 a brief review related to circular DRA antennas is presented to illustrate the possible radiation modes and the main design equation governing the DRA performance. In the Section 3.7, we will try to highlight the most up to date research work about the hybrid configurations and loaded horn antennas. Finally, an overview of the simulation software packages and the numerical techniques they adopt is presented in Section 3.8.

3.2 Electromagnetic Waves and Antenna Analysis

Solutions of electromagnetic systems, including radiated fields by antennas involve solving Maxwell's equations subject to appropriate boundary conditions. These equations consist of a set of four vector-differential equations that describe all of electromagnetic field behavior. The four Maxwell's equations [91] in both integral and differential forms are listed in Eq. (3.1) to Eq. (3.4).

Differential form	***Integral form***	
$\nabla \cdot \vec{D} = \rho_v$	$\oiint \vec{D} \cdot d\vec{S} = Q_{enc}$	(3.1)
$\nabla \cdot \vec{B} = 0$	$\oiint \vec{B} \cdot d\vec{S} = 0$	(3.2)
$\nabla \times \vec{E} = -j\omega\mu\vec{H}$	$\oint \vec{E} \cdot d\vec{l} = -j\,\omega \iint \vec{B} \cdot dS$	(3.3)
$\nabla \times \vec{H} = j\omega\varepsilon\vec{E} + \sigma\vec{E} + \vec{J}$	$\oint \vec{H} \cdot d\vec{l} = j\omega \iint \vec{D} \cdot dS + \iint \sigma\vec{E} \cdot dS + \iint \vec{J} \cdot dS$	(3.4)

where $\vec{D}$ is the electrical flux density, ρ_v is the volume charge density, σ is the conductivity, $\vec{B}$ is the magnetic flux density, $\vec{E}$ is the electrical field intensity, $\vec{H}$ is the magnetic field intensity, Q_{enc} is the total enclosed charge, and $\vec{J}$ is the source current density.

The solution of the Maxwell's equations will not be unique unless the proper boundary conditions are satisfied. The boundary conditions can be summarized as [91]:

$$\hat{n} \times \left(\vec{H}_2 - \vec{H}_2\right) = \vec{J}_s \tag{3.5}$$

$$\left(\vec{E}_2 - \vec{E}_1\right) \times \hat{n} = \vec{M}_s \tag{3.6}$$

$$\hat{n} \cdot \left(\vec{D}_2 - \vec{D}_1\right) = \rho_s \tag{3.7}$$

$$\hat{n} \cdot \left(\vec{B}_2 - \vec{B}_1\right) = 0 \tag{3.8}$$

where $\vec{J}_s$ is the electrical surface current, $\vec{M}_s$ is the magnetic surface current, ρ_s is the electrical charge density, and $\hat{n}$ is the unit vector normal to the boundary between the two media directed from medium 1 to medium 2, as shown in Fig. 3.1.

The boundary condition equations should be evaluated and the equations apply to each point along the boundary between the two media.

(a) General case (b) PEC medium case

Figure 3.1 Boundary Conditions of two mediums.

Both Eq. (3.3) and Eq. (3.4) (also known as Faraday's law, and Ampere's law) are governing the electromagnetic radiation. The spatial variation of the fields is represented by the curl operator, which are coupled to the time variation. When the E-field propagates, it is altered in space, which gives rise to a time-varying magnetic field. A time-varying magnetic field, then varies as a function of position in free space, which gives rise to a time varying electric field. From Eq. (3.2), it can be concluded that the field $\vec{B}$ possesses only a circulation so, a new vector $\vec{A}$ (the magnetic vector potential) can be defined as:

$$\vec{H} = \frac{1}{\mu}\nabla \times \vec{A} \tag{3.9}$$

The antenna field determination consists of solving for the fields that created by an impressed current distribution $\vec{J}$ [91]. After some mathematical manipulations for Eqs. (3.3), (3.4) and (3.9), the wave equation can be obtained as:

$$\nabla^2 \vec{A} + \omega^2 \mu \varepsilon \vec{A} = -\mu \vec{J} \tag{3.10}$$

The solution of this equation leads to the evaluation of the potential vector $\vec{A}$, and consequently the electrical field can be easily found from:

$$\vec{E} = -j\omega\vec{A} - j\frac{\nabla(\nabla.\vec{A})}{\omega\mu\epsilon} \tag{3.11}$$

3.3 Antenna Parameters

In this section, brief definitions of some basic antenna parameters will be introduced [91] and how these parameters affect the overall behavior of transmitting / receiving antennas.

1. **Radiation Pattern:** according to [91], a mathematical function or a graphical representation of the radiation properties of the antenna as a function of space coordinates, including: directive, single or multiple narrow beams. The radiation property of most concern is the radiation intensity $U(\theta, \emptyset)$ which can be given by:

$$U(\theta, \emptyset) = r^2 \cdot W_{rad} \tag{3.12}$$

$$W_{rad} = \frac{1}{2} Re[\vec{E} \times \overrightarrow{H^*}] \tag{3.13}$$

where r is the distance from the antenna, and W_{rad} is the average radiation density.

2. **Directivity *D***: Ratio of the radiation intensity ($U(\theta, \phi)$) in the direction of the pattern maximum (i.e. the strongest emission direction) to the average radiation intensity (U_{ave}) at the same distance from the antenna.

$$D(\theta, \phi) = \frac{U(\theta, \phi)}{U_{ave}} = \frac{U(\theta, \phi)}{\frac{1}{4\pi}\iint U(\theta, \phi) d\Omega} \cdot \tag{3.14}$$

3. **Gain *G***: Directivity reduced by the losses of the antenna.

$$G(\theta, \phi) = e_o \frac{U(\theta, \phi)}{U_{ave}} = e_o D(\theta, \phi) \tag{3.15}$$

where e_o represents the overall antenna efficiency, and it can be estimated from:

$$e_o = e_c e_d e_r \tag{3.16}$$

and e_c is the conduction efficiency, e_d dielectric efficiency, and e_r is the mismatch efficiency.

4. **Side Lobe Level (SLL):** It is a measured value that indicates how the radiated power are concentrated into the main lobe. The SLL can be calculated from:

$$SLL_{dB} = 20log\frac{|U(SLL)|}{|U(max)|} \tag{3.17}$$

where $|U(max)|$ is the maximum value of the pattern magnitude, and $|U(SLL)|$ is the maximum value of the highest value of the side lobe magnitude.

5. **Polarization:** a quantity that describes the vector nature of electric fields radiated by an antenna, antenna polarizations may be: linear, circular, and elliptical.
6. **Axial Ratio (*AR*):** The axial ratio is the ratio of orthogonal components of an E-field. A circularly polarized field is made up of two orthogonal E-field components of equal amplitude (and 90 degrees out of phase).
7. **Antenna Radiation Efficiency:** The ratio of the total power radiated by an antenna (P_{rad}) to the net power accepted by the antenna from the connected transmitter (P_{in}).

$$\eta = \frac{P_{rad}}{P_{in}}. \tag{3.18}$$

8. **Input Impedance ($\boldsymbol{Z_A}$):** The measured impedance at the antenna terminal (i.e. feeding probe). Input impedance is composed of real and imaginary parts:

$$\boldsymbol{Z_A} = R_A + jX_A. \tag{3.19}$$

The input resistance R_A represents dissipation that can be accounted for the power leaves the antenna and never returns, or the ohmic losses associated by heating the antenna. Furthermore, X_A represents the stored energy in the near field of the antenna.

9. **Impedance Bandwidth:** Range of frequencies in which the antenna performance is acceptable (i.e. reflection coefficient $S_{11} \leq$ -10 dB).

10. **Group Delay (GD):** It is the rate of the change of the antenna phase shift ($\phi(\omega)$) w.r.t. the angular frequency(ω). It can be calculated from:

$$GD = -\frac{d\phi(\omega)}{d\omega} \cdot \tag{3.20}$$

11. **Friis Equation:** it is a formula used to estimate the power received (P_r) by one antenna as a function of the transmitted power of the other antenna (P_r), the transmitter and receiver antenna gains G_r, G_t, respectively, and the distance between them R as follow:

$$P_r = P_t G_t G_r (\frac{\lambda}{4\pi R})^2 \cdot \tag{3.21}$$

If the effects of impedance mismatch, and attenuation are considered the received power can be evaluated as:

$$P_r = P_t G_t G_r (1 - |\Gamma_t^2|)(1 - |\Gamma_r^2|)(\frac{\lambda}{4\pi R})^2 e^{-\alpha R} \tag{3.22}$$

where Γ_t, and Γ_r are the transmitter and the receiver mismatch, and α is the absorption coefficient of the propagating medium.

3.4 Substrate Integrated Waveguide (SIW)

Conventional metallic waveguides have been widely used for many years in microwave and millimeter-wave radars and communication systems for its high efficiency, ease of design, reliability and durability.

However, their relatively high cost and difficult integration prevent them from being used in low-cost high-volume applications. As a new alternative for these metallic waveguides a new via-hole synthetic waveguide called substrate integrated waveguide has been introduced in [92], [93] to facilitate the integration of active planar components with high-Q passive components. A typical geometry is illustrated in Fig. 3.2 The substrate's top and bottom ground planes form the broad walls of the waveguide and a discrete metallic via-hole array forms the narrow walls. According to [94], in order to assure the operation of these arrays the via-hole diameter (*d*) should be less than or equal to ($\lambda_g/10$) and the via-hole separation (*p*) should be less than or equal to (*d*). Other formulas, governing the relation between *(d)* and *(p)*, was presented in [95]. These formulas are based on the fact that the dominant losses in the SIW structure can be accounted to the dielectric losses not the leakage.

The design equations that relate the SIW to the conventional waveguides can be found in [96] as:

Width of the equivalent waveguide $a_e = a \cdot \bar{a}$

Where:

$$\bar{a} = \zeta_1 + \frac{\zeta_2}{a/p + (\zeta_1 + \zeta_2 - \zeta_3)/(\zeta_2 - \zeta_3)} \tag{3.23}$$

$$\zeta_1 = 1.0198 + \frac{0.3465}{a/p - 1.0684}$$
$$\zeta_1 = -0.1183 + \frac{1.2729}{a/p - 1.2010}$$
$$\zeta_1 = 1.0082 + \frac{0.9163}{a/p + 0.2152}$$

a : is the SIW width
$\bar{a}$: is the waveguide normalization factor

The selection of different surface mounted SIW parameters is very critical to obtain a performance close to the metallic waveguide. According to [94], there are two main conditions must be satisfied:

$$d \leq \frac{\lambda_g}{5} \tag{3.24}$$

$$p \leq 2d \tag{3.25}$$

where, d is the via diameter and p is the distance between two successive vias. Alternative conditions given in [95] elaborated that:

$$p = \pi d \tag{3.26}$$

$$p \leq 0.2\lambda_g \tag{3.27}$$

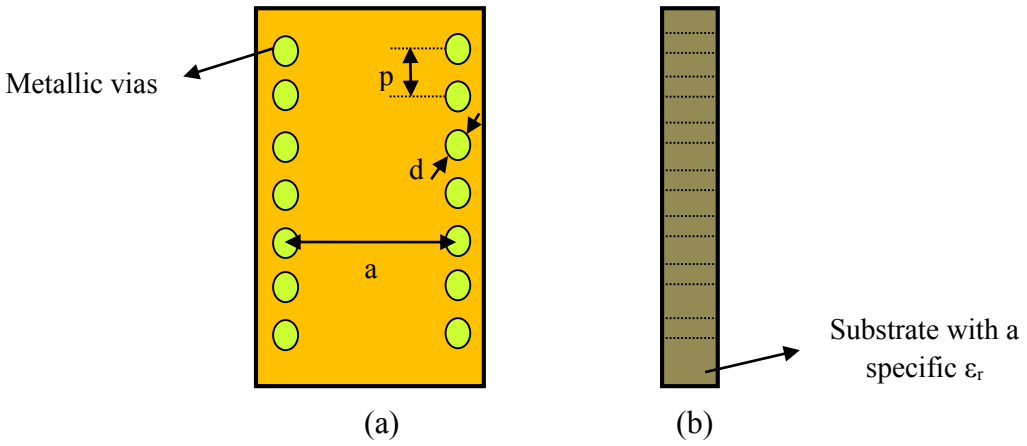

Figure 3.2 Geometry of the SIW (a) front view (b) side view.

3.5 Conical Horn Antenna

The conventional conical horn antenna [97], [98], shown in Fig. 3.3, is a well-known type of antennas consists of a flaring metal circular waveguide shaped like a horn to direct the radio waves. It can be used for many applications over a very wide range of microwave and millimeter-wave frequencies including a feed horn for parabolic antennas, a standard calibration antenna to measure the gain of other antennas, a radar gun, and a microwave radiometer. It characterized by high directivity (gain), low SWR, broad bandwidth, and simple construction and adjustment while its major disadvantages are relatively high cost and heavy weight.

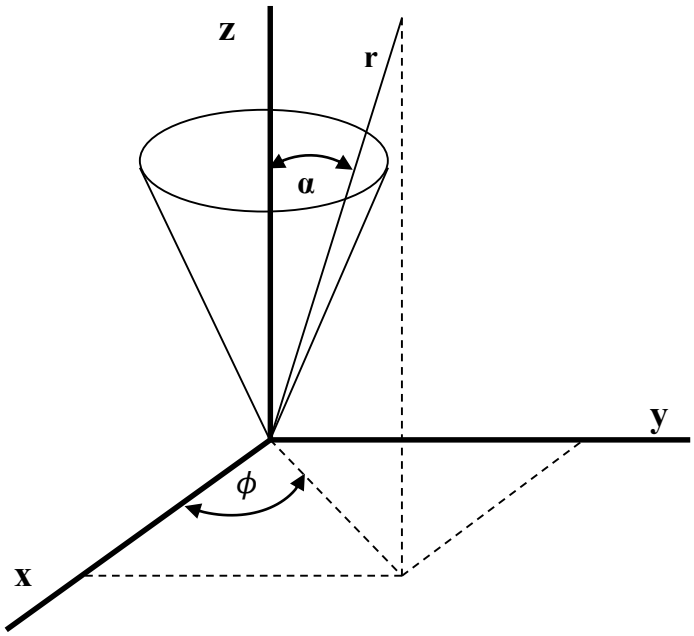

Figure 3.3 Geometry of the conical horn.

The field components within an infinite long conical horn antenna can be found in [99] as:

For TM waves:

$$E_r = -jC_A \frac{n(n+1)}{\omega \epsilon_r} h_n^{(2)}(kr) P_n^m(cos\theta)\, sin\, m\phi \tag{3.28}$$

$$H_r = 0 \tag{3.29}$$

$$E_\theta = jC_A \frac{ksin\theta}{\omega \epsilon_r} [h_n^{(2)}(kr) + kr h_n^{(2)\prime}(kr)]\, sin\, m\phi\, P_n^{\dot{m}}(cos\theta) \tag{3.30}$$

$$H_\theta = jC_A \frac{ksin\theta}{\omega \epsilon_r} h_n^{(2)}(kr) P_n^m(cos\theta)\, cos\, m\phi \tag{3.31}$$

$$E_\phi = -jC_A \frac{mk}{\omega \epsilon_r sin\theta} [h_n^{(2)}(kr) + kr h_n^{(2)\prime}(kr)]\, sin\, m\phi \cos\theta\, P_n^m(cos\theta) \tag{3.32}$$

$$H_\phi = C_A\, sin\, \theta\, h_n^{(2)}(kr) P_n^{\dot{m}}(cos\theta)\, sin\, m\phi \tag{3.33}$$

For TE waves:

$$E_r = 0 \tag{3.34}$$

$$H_r = -jC_A \frac{\dot{n}(\dot{n}+1)}{\omega \mu_r} h_{\dot{n}}^{(2)}(kr) P_{\dot{n}}^m(cos\theta)\, sin\, m\phi \tag{3.35}$$

$$E_\theta = -C_F \frac{mk}{sin\theta} h_{\dot{n}}^{(2)}(kr) P_{\dot{n}}^m(cos\theta)\, cos\, m\phi \tag{3.36}$$

$$H_\theta = jC_A \frac{ksin\theta}{\omega \epsilon_r} [h_{\dot{n}}^{(2)}(kr) + kr h_{\dot{n}}^{(2)\prime}(kr)]\, sin\, m\phi\, P_{\dot{n}}^{\dot{m}}(cos\theta) \tag{3.37}$$

$$E_\phi = -C_F\, ksin\, \theta\, h_{\dot{n}}^{(2)}(kr) P_{\dot{n}}^{\dot{m}}(cos\theta)\, sin\, m\phi \tag{3.38}$$

$$H_\phi = -jC_F \frac{mk}{\omega \mu_r sin\theta} [h_{\dot{n}}^{(2)}(kr) + kr h_{\dot{n}}^{(2)\prime}(kr)]\, sin\, m\phi \cos\theta\, P_{\dot{n}}^m(cos\theta) \tag{3.39}$$

Where:

$h_n^{(2)}$ is a Hankel function of the second kind of order *n*,

P_n^m is Legendre function of order n and degree m,

and k is the wave number.

From the previous equations we can conclude that the cut off frequencies are not dependent on the wave number k so, the fields near the aperture is said to be well matched to free space. Also the finite length cone with a length r_h for which $kr_h >> n+0.5$ has a field distribution around the aperture not much different from the fields at the aperture of an infinite cone, i.e. it can propagate any frequency to free space without any restrictions.

3.6 Circular Dielectric Resonator Antenna (DRA)

In the late 1960s, dielectric resonators were proposed as high-Q elements in microwave circuits, such as filters and oscillators, [100]. In the early 1980s, dielectric resonators were used as antennas (DRAs) [101]. Many researchers have shown great interest in using DRAs in many different applications because of their unique feature of low-loss and high-efficiency compared to metallic patches [102]. Dielectric resonator antennas (DRA) [103]-[105] can be considered as the best alternative for the conventional microstrip patch radiators due to some attractive features including small size, wide bandwidth, low cost, ease of manufacturing, high radiation efficiency and different radiation characteristics according to the excited mode in the DRA.

There are many modes that can be excited in the circular DRA, shown in Fig. 3.4, such as $HEM_{11\delta}$, TE_{10}, TM_{01}, $HEM_{12\delta}$,….etc. From all these modes there are only two radiative modes that can be excited to make the DR works as an antenna, these two modes are $HEM_{11\delta}$ and TM_{01}. However, some recent studies [105] show that the DR can work as an antenna with mode $HEM_{12\delta}$.

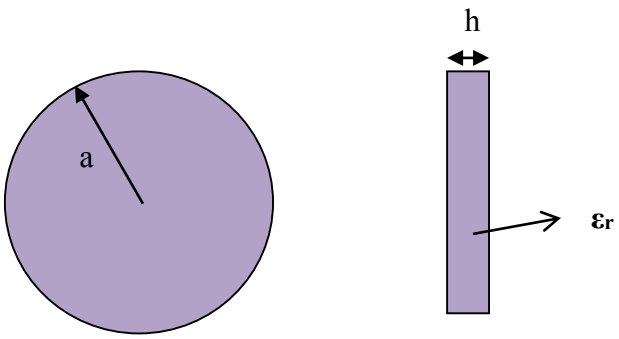

Figure 3.4 Geometry of circular DRA.

Empirical expressions are obtained for the resonant frequency and the radiation Q-factor for the $HEM_{11\delta}$ and TM_{01} modes[104] as:

For the TM_{01} mode:

$$k_o a = 0.8945(1 + 3.017x^{0.881} + e^{0.962-1.6252x})/{\varepsilon_r}^{0.45} \quad (3.38)$$

For the $HEM_{11\delta}$ mode:

$$k_o a = (1.6 + 0.531x + 1.392x^2 - 0.575x^3 + 0.088x^4)/{\varepsilon_r}^{0.45} \quad (3.39)$$

where:

k_o is the free space wave number

a is the radius of the circular DRA

h is the height of the DRA

and

x=a/ (2h).

3.7 Hybrid Antenna Configurations

Many gain enhancing techniques have been used before to increase the overall antenna gain. One of the main techniques is using an array principle but the antenna size becomes a serious problem. In recent years, researchers have been trying to adopt new techniques not only to enhance the gain but also to keep the overall antenna size within the accepted limits. The most attractive technique is to use hybrid configurations [106]-[111] where multiple antennas are excited together with the same or different modes over the same frequency range of operation.

In [106], circular waveguide elements can be electromagnetically coupled trough circular apertures to a stripline and the overall radiation becomes a combination from both the strip line plus the open ended waveguide which reflects on the overall gain of antenna array. A surface mounted pyramidal horn is excited by a rectangular patch antenna and a dipole in [107] or by a patch surrounded by a resonating ring as in [108], while in [109] stacked patches are used to feed a horn antenna. To increase the overall antenna efficiency the microstrip patch antenna is replaced by a rectangular DRA in [110]. Merging an antenna array and surface mounted horn is described in [111].

3.8 Simulation Software Packages

For antenna design verification, simulation software enables us to use virtual prototyping before physical trials, and optimization instead of experimentation. In the proposed work, simulations are performed using two different commercial software packages. The first simulator is the ANSYS High Frequency Structure Simulator (HFSS) software [112]. HFSS is considered to be one of the industry-standard software programs these days and a

powerful 3D electromagnetic (EM) field simulation tool. It is based on a 3D full-wave Finite Element Method (FEM) which is a frequency-domain numerical technique for solving Maxwell's equations shown in Eq. 3.1 to Eq. 3.4. Due to its accuracy, capacity, and performance, HFSS is used by scientists and engineers to analyze and design different high-frequency and high-speed applications.

The other simulator is Computer Simulation Technology Microwave Studio (CSTMWS) [113]. CSTMWS is a specialist tool for the fast and accurate 3D EM simulation of high frequency problems. Currently, it is considered one of the industry-standard software programs and a powerful 3D EM field simulation tool. CSTMWS is based on Finite Integration Technique (FIT) [114] which is equivalent to Finite Difference Time Domain (FDTD). Unlike FEM, FIT is a time-domain numerical technique for solving Maxwell's equations.

3.8.1 Finite Element Method (FEM)

The Finite Element Method is certainly widespread. Flexibility is its greatest advantage with respect to traditional finite-difference methods. Elements can have various shapes, and can be easily adapted to any shape of the boundary and interface geometries. Flexibility can even be a little excessive, since it introduces a strong influence of the user on the results obtained, so that it must be exploited with caution. Besides flexibility, another advantage lies in the form of the algebraic system of equations obtained, which generally has a symmetric positive definite matrix of coefficients. This property is not ensured in finite-difference schemes, and can facilitate the solution. Another advantage claimed is to have simpler programming on account of the easier introduction of the boundary conditions [115].

The finite element method (FEM) has its origin in the field of structural analysis and in complicated thermal systems; such as nuclear power plants. It is also applied to fluid mechanics. Although the earlier mathematical treatment of the method was provided by Courant [116] in 1943, the method was not applied to electromagnetic (EM) problems until 1968 by Arlett [117]. Since then the method has been employed in diverse areas such as waveguide problems, electric machines, semiconductor devices, microstrips, antennas, and absorption of EM radiation by biological bodies.

The finite element method consists primarily of replacing a set of differential equations which have a number of unknown variables with an equivalent, but approximate set of algebraic equations where each of the unknown variables is evaluated at a nodal point. Several different methods may be used in the evaluation of these algebraic equations, and finite element methods are often classified as to the method used. Unfortunately, no one method is suitable for all problems likely to be encountered in engineering today, so several methods have to be examined in order to choose the proper one for a particular problem.

The finite element analysis of any problem involves basically five steps [115]:

- Discretizing the solution region into a finite number of sub-regions or elements.
- Deriving governing equations for a typical element.
- Assembling of all elements in the solution region.
- Applying the boundary conditions.
- Solving the system of equations obtained.

One of the challenges for FEM programmers is to minimize the solution errors. These errors have three main sources in a typical FEM solution, which are discretization errors, formulation errors and numerical errors. Discretization error results from transforming the physical system (continuum) into a finite element model, Fig. 3.5, and can be related to modeling the boundary shape, the boundary conditions, etc. Formulation error results from the use of elements that don't precisely describe the behavior of the physical problem. Elements which are used to model physical problems for which they are not suited are sometimes referred to as ill-conditioned or mathematically unsuitable elements. For example a particular finite element problem might be formulated on the assumption that displacements vary in a linear manner over the domain.

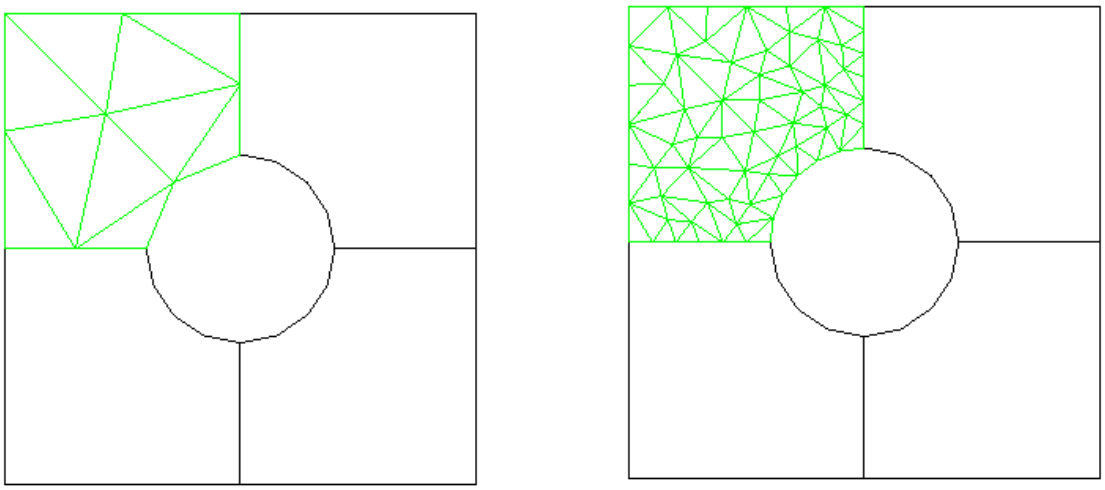

a) Discretization error due to poor geometry representation

b) Discretization error effectively eliminated

Figure 3.5 The discretization error manipulation.

3.8.2 Finite Integration Technique (FIT)

Both FIT and FDTD are numerical time domain methods for solving Maxwell's equations whose origins call be traced ill the work of Yee in 1966 [118]. The FIT was first proposed by Weiland in 1977 [114] and the FDTD was applied by Taflove in 1980 [119]. The power of FIT method comes from its high efficiency and flexibility in geometrical modeling and boundary handling as well as incorporation of material properties and arbitrary material distributions such as non-linearity, dispersion, and anisotropy. Moreover, the use of a consistent dual orthogonal grid in conjunction with an explicit time integration scheme leads to compute and memory-efficient algorithms where, the solution time required increases more slowly with bigger problem size.

The steps required for solving any problem using FIT can be summarized as [115]:

2. Dividing the solution region into a grid of nodes.
3. Approximating the given differential equation by finite difference equivalent that relates the dependent variable at a point in the solution region to its values at the neighboring points.
4. Solving the difference equations subject to the prescribed boundary conditions and / or initial conditions.

3.9 Summary

In this chapter, the methodology and theoretical background required for designing high performance antenna elements are presented. Recent research work on hybrid antenna configurations and loaded horn antennas is highlighted. In addition, a brief discussion about commercial software packages used in this work and their associated numerical techniques is presented.

Chapter 4

UWB Antenna Probes

4.1 Introduction

This chapter consists of three main sections. The first one focuses on the methodology and the design principles behind the UWB antenna design. The second section introduces three proposed UWB monopole antenna prototypes and shows an investigation of their operating principles and mechanism that lead to the UWB characteristics. While, in the third section of this chapter, an ultra-wideband (UWB) directive array for through-wall microwave imaging / detection (TWMI) applications is presented. This detection probe consists of 4-element Balanced Antipodal Vivaldi Antenna array (BAVA) fed by 1-to-4 UWB modified Wilkinson power divider.

All the proposed antenna probes are optimized, realized on Teflon substrates (Rogers RT-5880 and 6002) using thin film technology and photolithographic technique and tested using a Vector Network Analyzer (VNA). Good agreement is found between numerical and experimental results.

4.2 UWB Antenna Probe Design

The antenna element is considered as a key component of UWB detection / imaging systems and affects their overall performance. There are significant demands on antenna designers to design small size, and stable gain elements with broader bandwidth to cover the entire UWB range [8]. The printed disc monopole antenna is selected as our first choice for having a stable gain UWB scanning probe. To determine the initial parameters of the

printed disc monopole antenna, we should first understand their operation mechanism. The idea behind achieving this huge UWB bandwidth is due to overlapping closely spaced multiple resonance modes and choosing the appropriate feeding mechanism supporting the wide band operation. The design procedure starts by creating a simple disc, where the size of the disc determines the frequency of the first resonant mode (f_o) which is chosen to be in the middle of the UWB range. At the first resonance, the disc antenna tends to behave like a quarter wavelength monopole antenna. This is why the diameter of the circular disc is almost λ/4 at this frequency. Then the higher order modes ($f_1, f_2, \dots, f_N$) will be excited as a result of modifying the disc by cutting different shapes (semi-circle, ellipse, overlapped circle, etc.). In addition, the ground plane should be of a finite length and width. The width of the ground plane is found to be approximately twice the diameter of the disc or λ/2 at the first resonant frequency [120].

Although monopole based UWB antennas are characterized by a stable radiation pattern over the operating band, the total realized gain of such antennas is about 6 dB. This gain is not sufficient in some detection / imaging applications, especially for lossy wall penetration. So, the need of alternative probes to overcome this limitation becomes urgent. One of the possible solutions is to use the Balanced Antipodal Vivaldi Antenna (BAVA) [121].

In order to verify the proposed designs before fabrication, commercial simulation software packages become a critical issue. In this work two different software packages were used. The first one is HFSS [112] while the other one is CSTMWS [113]. Later, an optimization process can be carried out on these simulators for achieving the optimum results of the proposed design. Verification of the simulated results is carried out by

comparing results obtained using the two simulators before prototyping the antenna elements. Finally, the proposed antenna prototypes are fabricated using thin film technique and their performance are measured using Vector Network Analyzer (VNA).

4.3 UWB Monopole Antenna Probes

In this section, three different UWB monopole antennas with elliptical slot, introduced in [J1], and [C1], are presented. The proposed antenna designs offer UWB radiation with compact size, simple feed structure, and stable gain. The proposed designs have a reduction in the antenna size compared with [34] and a better gain at lower frequencies than [36]. The calculated results show that the proposed antenna designs can achieve a reflection coefficient S_{11} less than -10 dB over an UWB range from 2.5 GHz to beyond 14 GHz. Detailed design and associated results are presented in the following sub-sections.

4.3.1 Elliptical Slot (UWB) Antenna with Circular Radiator

Fig. 4.1 shows the geometry and configuration of the circular radiator antenna. The proposed antenna is designed and realized on RT5880 substrate (ε_r = 2.2, $tan\delta$ = 0.0009 and thickness h = 1.575 mm). The antenna consists of an elliptical aperture, with an area of ($2A \times 2B$) mm^2, etched out from the ground plane of a PCB and a microstrip line with half circular shaped ring stub for excitation. Design of the elliptical aperture is determined by minimizing the aperture area while satisfying the input impedance matched over the entire UWB band. The excitation of the antenna is formed by a 50Ω microstrip line of width W_{50} = 4.3 mm and length L_{50} = 10 mm and a tapered line of width W_1 and length L_1 for impedance transformation to match with the radiator element. The radiating element is a half circular shaped ring stub of only three parameters: the inner radius R_1, the outer radius R_2, and the extrusion depth S, as shown in Fig. 4.1. Due to the substrate's stable

behavior at high frequency, an optimization process has been carried out using full-wave electromagnetic simulators. The optimization process led to the optimal parameters listed in Table 4.1.

The measured and calculated reflection coefficient S_{11} against the frequency of the designed antenna is plotted in Fig. 4.2. It is observed from the results that the calculated return loss using HFSS and CSTMWS show some differences, especially around 13 GHz because of different meshing schemes used by both programs. The designed antenna exhibits an impedance bandwidth of 11 GHz starts from 2.5 GHz to beyond 14 GHz theoretically, but it is around 9.5 GHz practically that is may accounted to the connector and cable effects at high frequency. Generally there are good agreement between the measured and the simulated results. Fig 4.3 shows both the measured and the CSTMWS calculated E-plane and H-plane radiation patterns at frequencies 3 GHz, 5 GHz, 7 GHz, and 9 GHz. As expected, the antenna exhibits a dipole-like radiation patterns in the E-plane and good radiation patterns in the H-plane.

Table 4.1 Optimized dimensions for the circular radiator antenna (in mm).

Parameter	*W*	*L*	W_1	L_1	*S*	R_1	R_2	*A*	*B*
Value	*45*	*45*	*3*	*12.4*	*1.4*	*4.5*	*11*	*9.6*	*19*

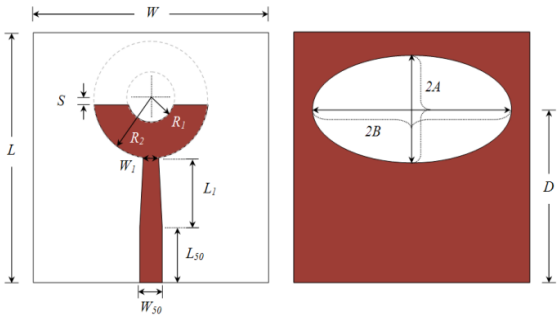

(a) (b)

Figure 4.1 Geometry of the circular radiator antenna (a) front view (b) back view.

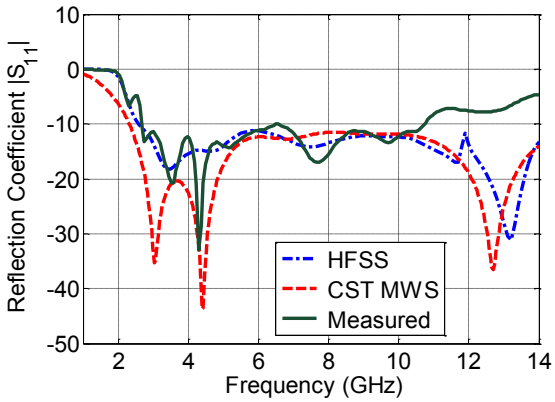

Figure 4.2 Simulated and measured return loss S_{11} of the circular radiator design.

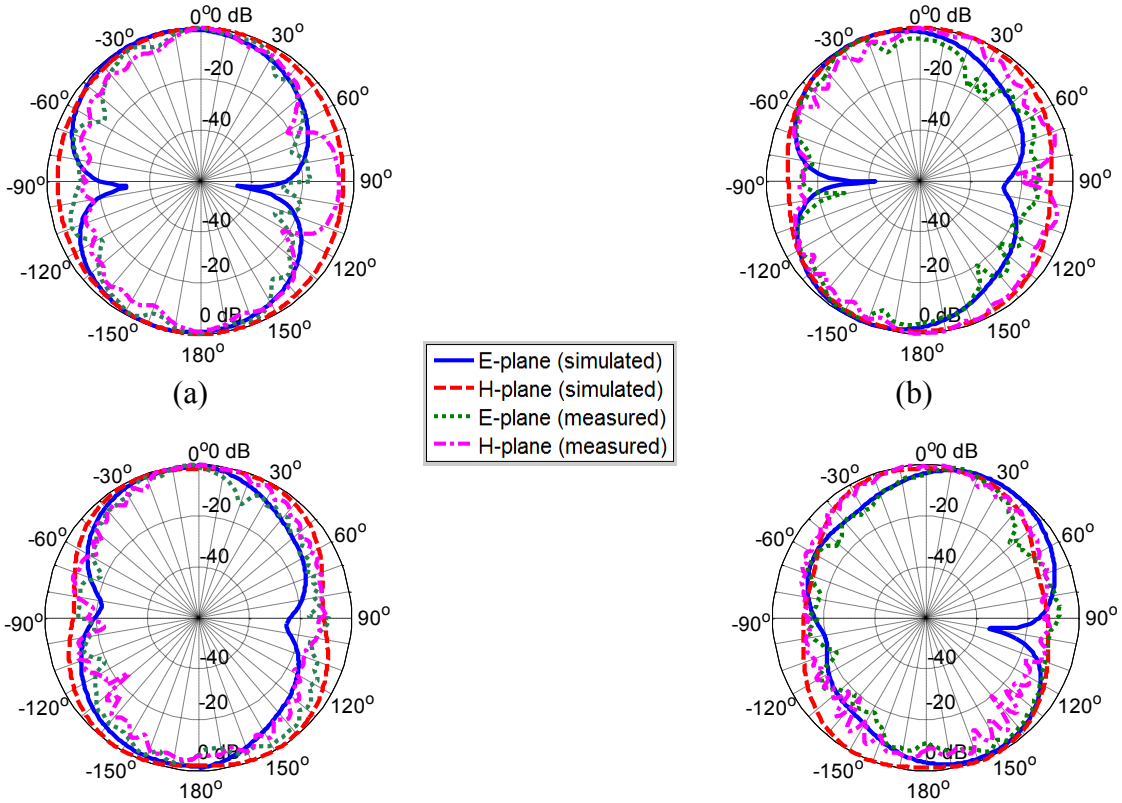

Figure 4.3 Measured and Calculated E-plane and H-plane radiation patterns for circular radiator antenna at (a) 3 GHz (b) 5 GHz (c) 7 GHz and (d) 9 GHz.

4.3.2 Elliptical Slot (UWB) Antenna with Crescent Radiator

The geometry and configuration of the crescent radiator design are shown in Fig. 4.4. The proposed antenna has a crescent shaped ring stub for excitation. The antenna excitation is accomplished by using a 50Ω microstrip line with the same parameters as the one used in previous designs. The radiating element is a crescent shaped ring stub with three design parameters: the inner radius R_1, the outer radius R_2, and the extrusion depth S, as shown in Fig. 4.4. The optimized parameters, obtained by CSTMWS, have been tabulated in Table 4.2.

The measured and simulated results for the reflection coefficient S_{11} of the crescent radiator are shown in Fig. 4.5. It can be seen from the results that the calculated return loss using HFSS and CSTMWS agrees reasonably well with measured results over the UWB band. The designed antenna exhibits a simulated impedance bandwidth of 11 GHz starts from 3 GHz to 14 GHz but the measured value is around 9.5 GHz for the same reasons stated before, but still covers the whole UWB frequency band. Fig 4.6 shows a comparison between the measured and the CSTMWS simulated E-plane and H-plane radiation patterns at frequencies 3 GHz, 5 GHz, 7 GHz, and 9 GHz. It can be noted that the antenna also exhibits good radiation patterns in H-plane with a stable shape over the operated bandwidth.

TABLE 4.2 Optimized dimensions for the crescent radiator antenna (in mm).

Parameter	*W*	*L*	W_1	L_1	*S*	R_1	R_2	*A*	*B*	*D*
Value	*45*	*45*	*3*	*12.5*	*6.65*	*11*	*11*	*9.5*	*20*	*31.2*

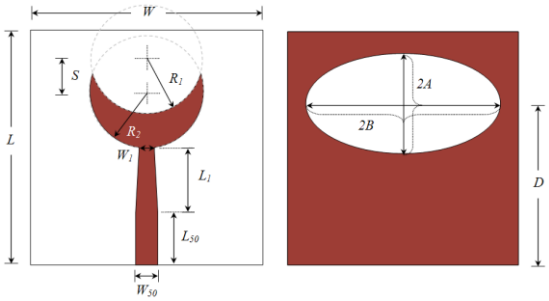

(a) (b)

Figure 4.4 Geometry of the crescent radiator antenna (a) front view (b) back view.

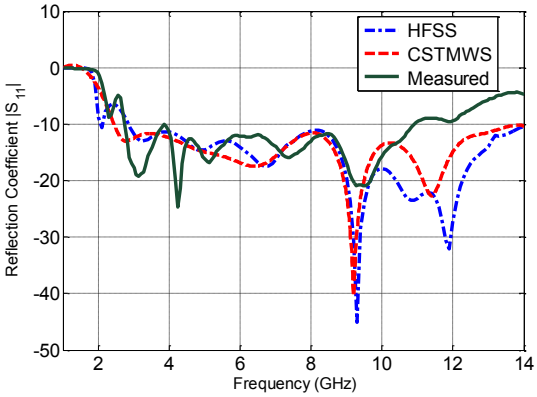

Figure 4.5 Simulated and measured return loss S_{11} of the crescent radiator.

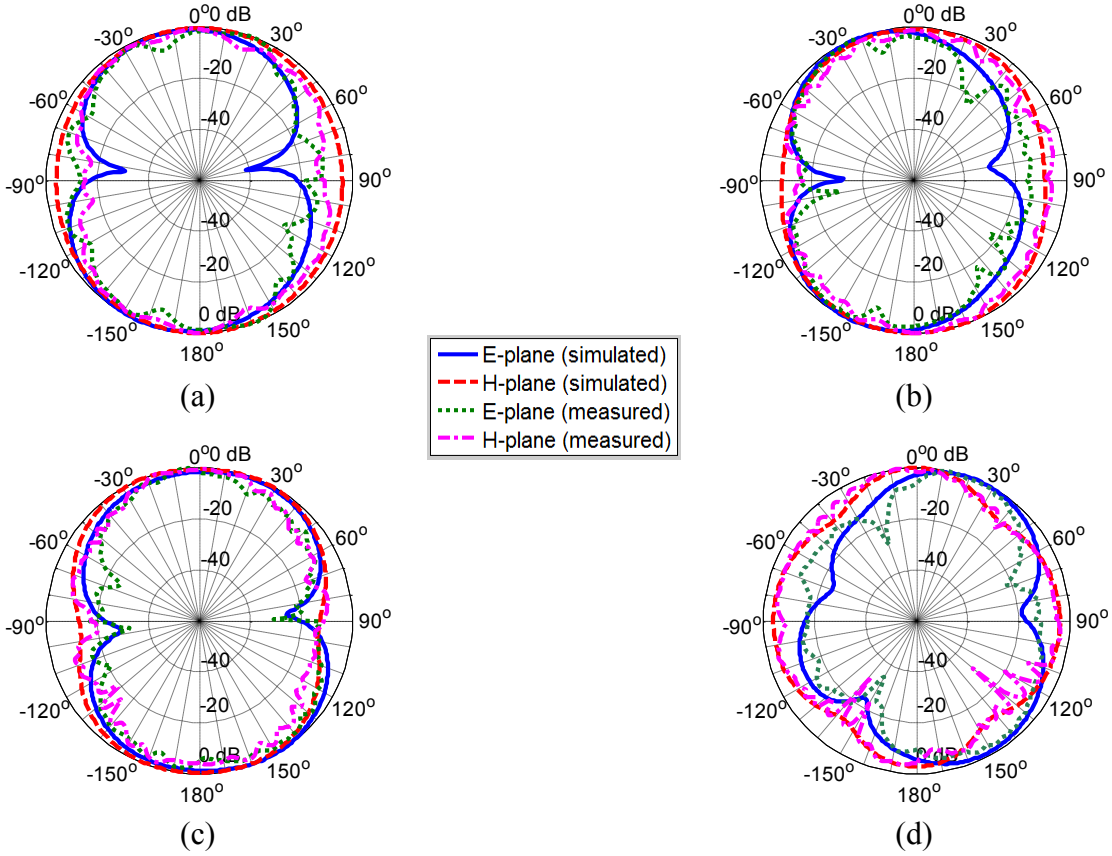

Figure 4.6 Measured and calculated E-plane and H-plane radiation patterns of the crescent radiator antenna design at (a) 3 GHz (b) 5 GHz (c) 7 GHz and (d) 9 GHz.

4.3.3 Elliptical Slot (UWB) Antenna with Elliptical Radiator

The geometry and configuration of the elliptical radiator antenna is illustrated in Fig. 4.7. The proposed antenna has a half elliptical shaped ring stub for excitation. The excitation of the antenna is formed by a 50Ω microstrip line of width W_{50} = 4.3 mm and length L_{50} = 10 mm and a tapered line of width W_1 and length L_1. The radiating element is a half elliptical shaped ring stub of five parameters: the outer major diameter R_x, the outer minor diameter R_y, the inner major diameter R_{xi}, the inner minor diameter R_{yi}, and the extrusion depth S as shown in Fig. 4.7. An optimization process has been carried by CSTMWS and the optimized parameters have been tabulated in Table 4.3.

TABLE 4.3 Optimized dimensions for the elliptical radiator antenna (in mm).

Parameter	*W*	*L*	W_1	L_1	*S*	R_1	R_2	*A*	*B*	*D*
Value	*45*	*45*	*3*	*12.5*	*6.65*	*11*	*11*	*9.5*	*20*	*31.2*

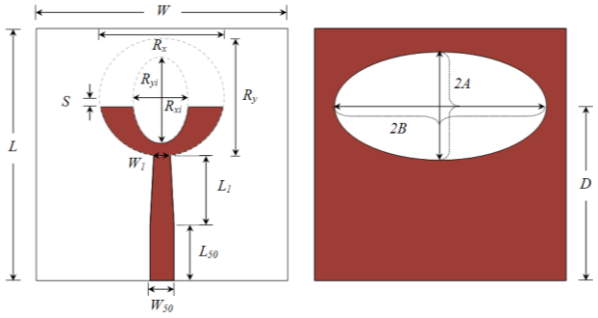

(a) (b)

Figure 4.7 Geometry of the elliptical radiator antenna (a) front view (b) back view.

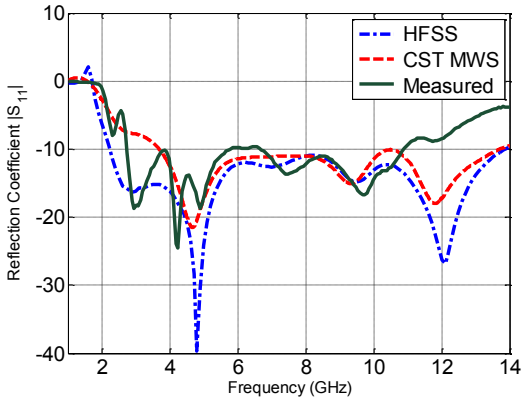

Figure 4.8 Simulated and experimental return loss S_{11} of the elliptical radiator antenna design.

Fig. 4.8 presents a comparison between the calculated and the measured reflection coefficient S_{11} against the frequency for the proposed antenna. The designed antenna exhibits an impedance bandwidth of 12 GHz starts from 2 GHz to 14 GHz (HFSS) and an impedance bandwidth of 10.5 GHz starts from 3.5 GHz to 14 GHz (CSTMWS). The measured and the calculated E-plane and H-plane radiation patterns for the proposed antenna at frequencies 3 GHz, 5 GHz, 7 GHz, and 9 GHz are shown in Fig. 4.9. The antenna also exhibits a dipole-like radiation patterns in E-plane and good radiation patterns in H-plane with good radiation pattern stability with frequency. A photo of the fabricated three antenna designs is shown in Fig. 4.10.

The calculated gain curves in the boresight (θ = 180°) direction for the three proposed designs are plotted in Fig. 4.11. It can be noticed that the proposed antenna gain is almost stable over the whole frequency band.

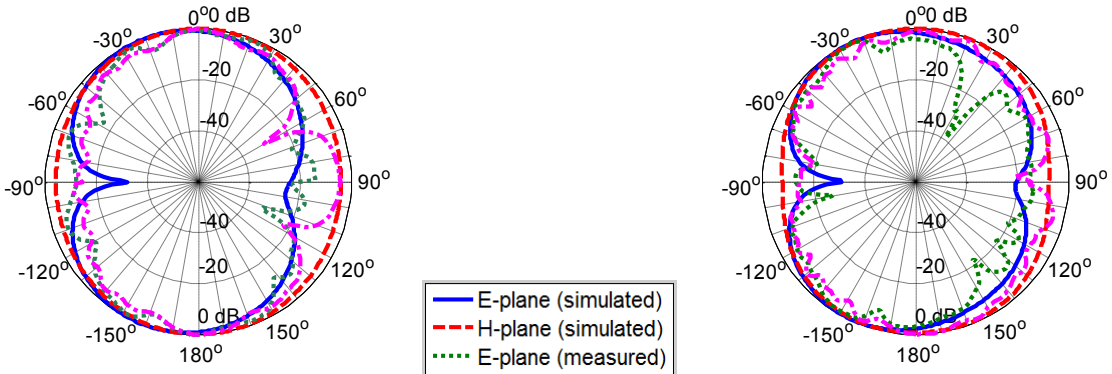

(a) (b)

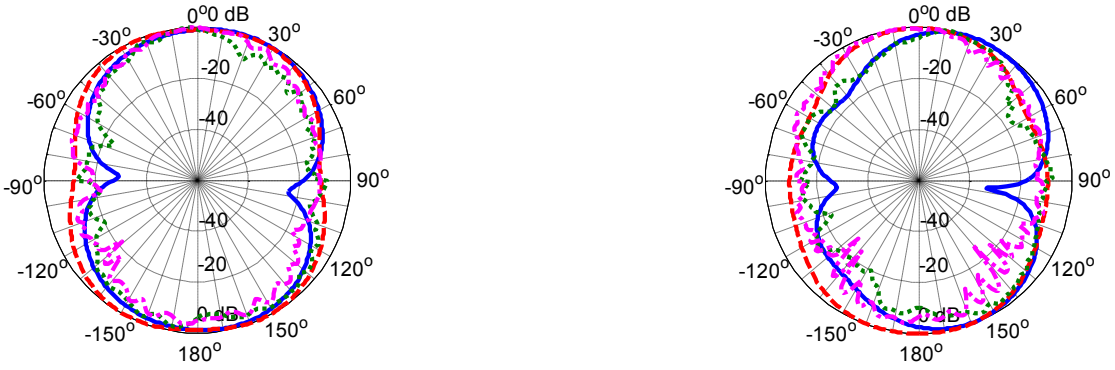

Figure 4.9 Measured and calculated E-plane and H-plane radiation patterns for the elliptical radiator antenna design at (a) 3 GHz (b) 5 GHz (c) 7 GHz and (d) 9 GHz.

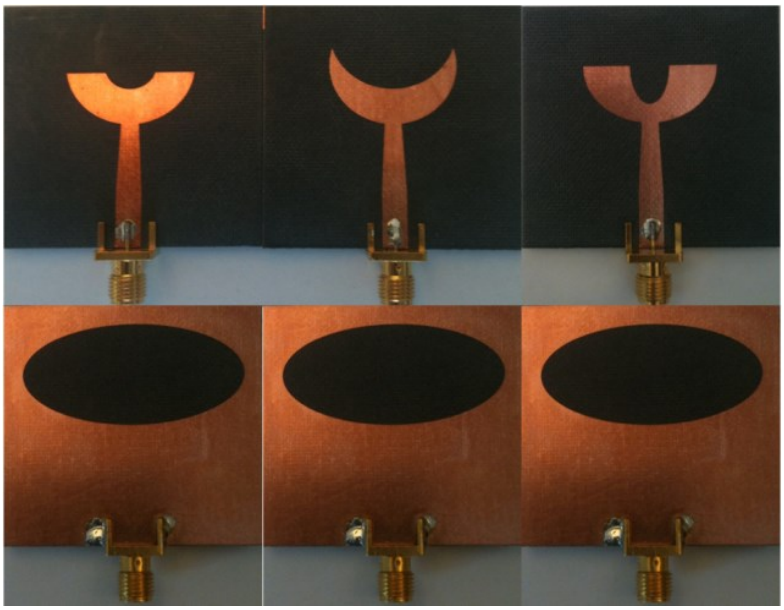

Figure 4.10 A photo of the three fabricated UWB antennas.

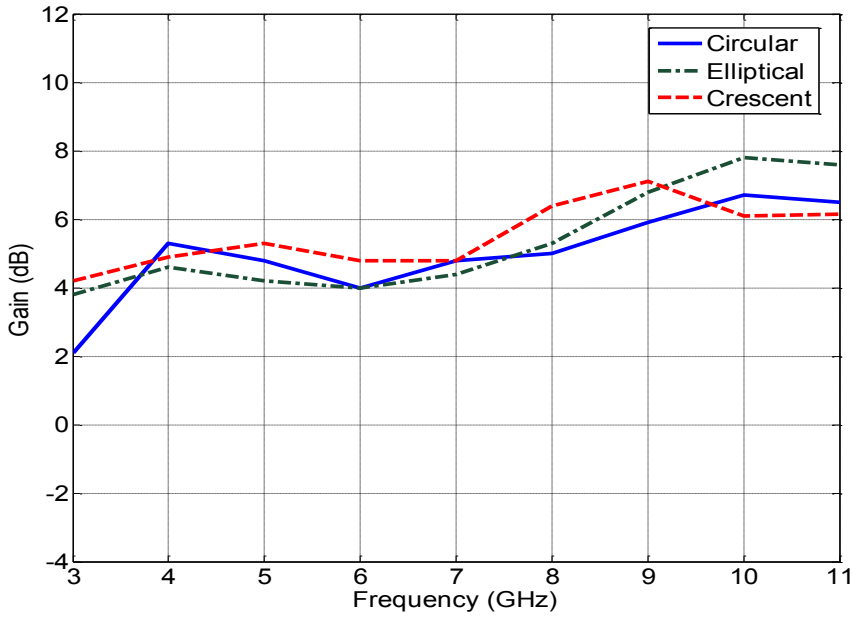

Figure 4.11 Calculated gain curves for the three slot coupled UWB antenna prototypes.

4.4 UWB BAVA Antenna Array Design

In some TWMI application, the walls under study are very lossy causing the EM waves to attenuate rabidly. In such case, there are only two possible solutions. The first one is to use higher power levels of the input signal power which in not convenient due to the cost increasing. The other solution is to employ very high gain UWB antenna probe (i.e. larger than 11 dB).

In order to come out with such antenna probe, an antenna array system consists of high directive elements are required. Furthermore, not only very high gain and low sidelobe level (SLL) are needed in such array system integrating the antenna array with its feeding network, but also good impedance matching over the UWB is required. The BAVA antenna element is considered as a good candidate for this application. The proposed antenna array

system in [C6] is considered as a very good alternative to replace the heavy metallic UWB horn sensor maintaining a high accuracy detection level.

4.4.1 UWB BAVA Antenna Element Design

The BAVA antenna presented in [121] is considered as a good choice to be implemented in this system because of its superior performance, including the high gain, the wide operating band that meets the UWB requirements and the low SLL. However, the design in [119] consists of a stacked four layers which adds a complexity to the fabrication process and increases the antenna weight.

In the proposed design [C6], a modified and improved BAVA antenna etched on single substrate of Rogers RT/Duroid 6002 with thickness of 1.524 mm and ε_r= 2.94. The antenna, shown in Fig. 4.12, includes the addition of nine slits on both arms of heights C_1 through C_4, governed by the following equation (all dimensions are in mm):

$$C_2=C_1-2,$$

$$C_3=C_2-2,$$

$$C_4=C_3-2. \tag{4.1}$$

This design shows a remarkable experimental performance in terms of the operating bandwidth (from 3.4 GHz to 10.2 GHz), the overall gain (around 10 dB) and the SLL (around 20 dB). Extensive parametric studies are carried out using CSTMWS to study the effect of different parameters on the antenna performance to select the proper number and dimensions of the slits. Fig. 4.13 shows a comparison between the CSTMWS simulated results for BAVA with and without slits and the experimental results. The optimized

dimensions for modified BAVA prototype are presented in Table 4.4. A photograph of the fabricated antenna prototype is shown in Fig. 4.14.

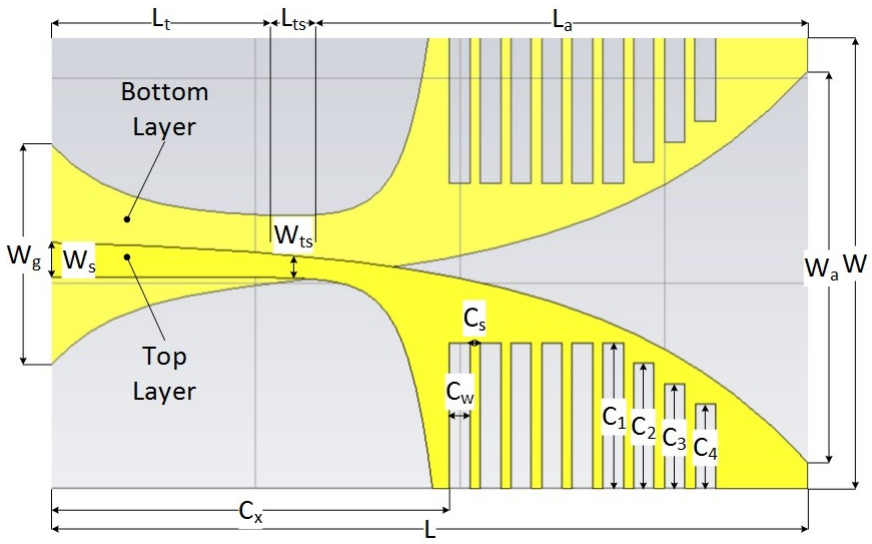

Figure 4.12 Modified BAVA antenna schematic diagram.

Table 4.4 Optimized dimensions of the modified BAVA antenna (in mm).

Parameter	C_1	C_2	C_3	C_4	C_5	C_w	C_x	L
Value	14.2	12.2	10.2	8.2	1	2	39	74
Parameter	L_a	L_t	L_{ts}	W	W_a	W_g	W_s	W_{ts}
Value	50	23	1	44	41	14	2	0.5

4.4.2 1-to-4 Modified UWB Wilkinson Power Divider

The feeding network in the proposed TWMI system is based on the UWB Wilkinson power divider presented in [122]. It consists of two stages 1-to-2 UWB Wilkinson power dividers printed on a Rogers RT/Duroid 5880 with thickness of 0.7874 mm and ε_r= 2.2. In order to enhance its performance, some modification has been made on the original design, including curved corners instead of the sharp ones to reduce the unintentional radiation from the feeding network and some modifications in the matching stubs lengths.

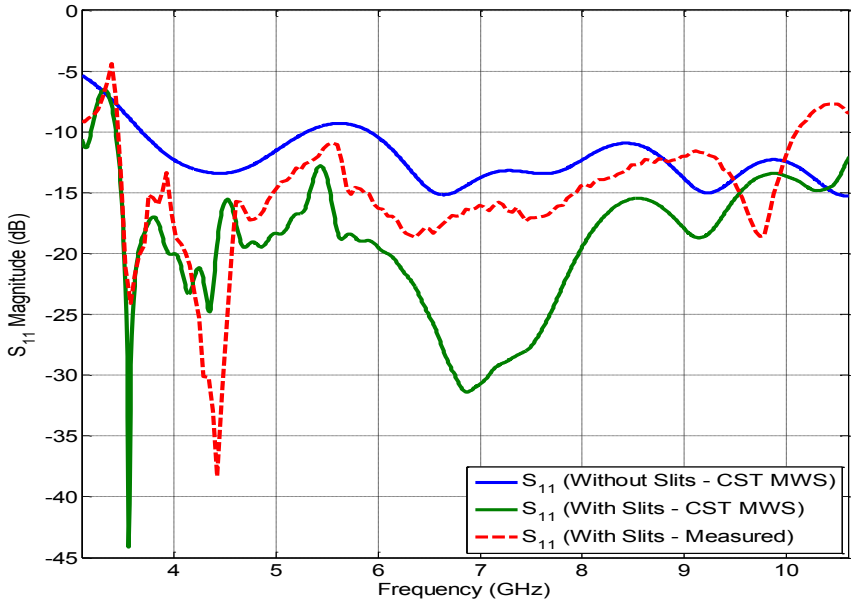

Figure 4.13 The reflection coefficient (S_{11}) of the proposed BAVA antenna.

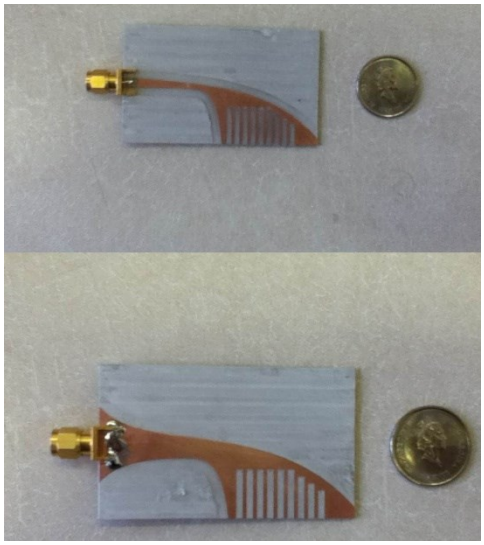

Figure 4.14 Top and bottom layers of modified UWB BAVA design.

Both CSTMWS simulation and fabrication results, as illustrated in Fig. 4.15, show very good agreement between each other. The impedance bandwidth of the proposed divider covers the entire UWB. In addition, the maximum insertion loss over the band does

not exceed 2 dB over the entire band except for the port no.4. It has a 4 dB insertion loss around 8.6 GHz which can be attributed to improper SMA connector soldering, as well as some minor fabrication mistakes.

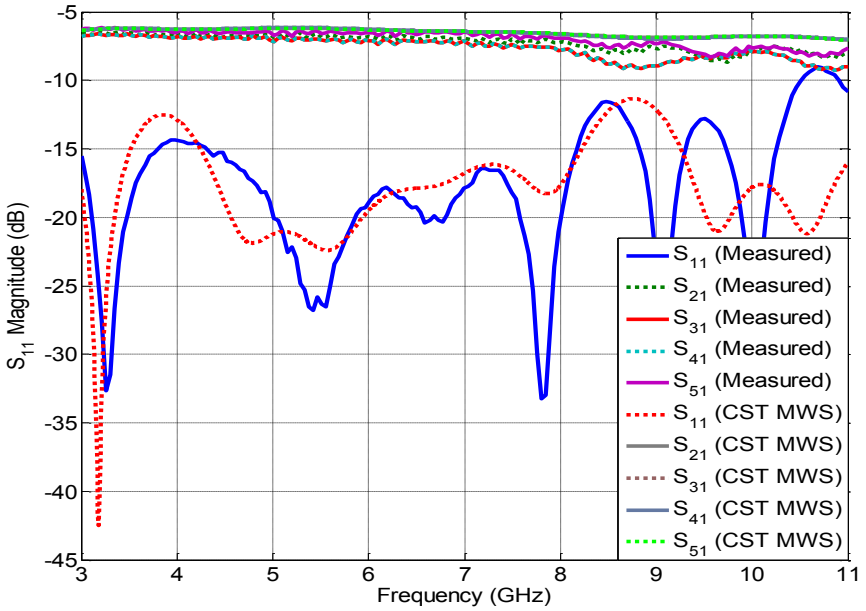

Figure 4.15 1-to-4 Modified UWB Wilkinson Power Divider S_{11}, S_{21}, S_{31}, S_{41}, S_{51}.

4.4.3 4-element UWB Antenna Array Results

In order to improve the scanning antenna gain, array principle is adopted. 4-BAVA antenna elements have been fabricated and connected to the proposed UWB power divider forming a 4-element linear antenna array. The separation distance between the antenna elements are chosen to be 0.6 λ at the center of the UWB range to avoid grating lobes. A photograph of the proposed antenna array system shown in Fig. 4.16.

The experimental reflection coefficient S_{11} of the proposed antenna system covers the majority of the UWB range, as presented in Fig. 4.17, except for a narrow band from

8.3 GHz to 8.6 GHz where S_{11} is around -8 dB. The measured E and H-plane radiation patterns comparison between a single BAVA and 4-element BAVA array are shown in Figs. 4.18. The measured radiation patterns show good agreement with the simulated patterns. However, it can be noticed some high levels of E-plane SLL (between 6 and 7 dB) at 7 GHz and 9 GHz, which may be accounted for the improper orientation of the antenna elements. Although the use of the 4-element antenna array should add theoretically about 6 dB over the single element gain, but the actual antenna system gain is greater than the single element by slightly less than 5.7 dB. This loss can be accounted for by the undesired mutual coupling between the antenna elements. Fig. 4.19 shows a comparison between the single element and the 4-element array in terms of the total realized gain.

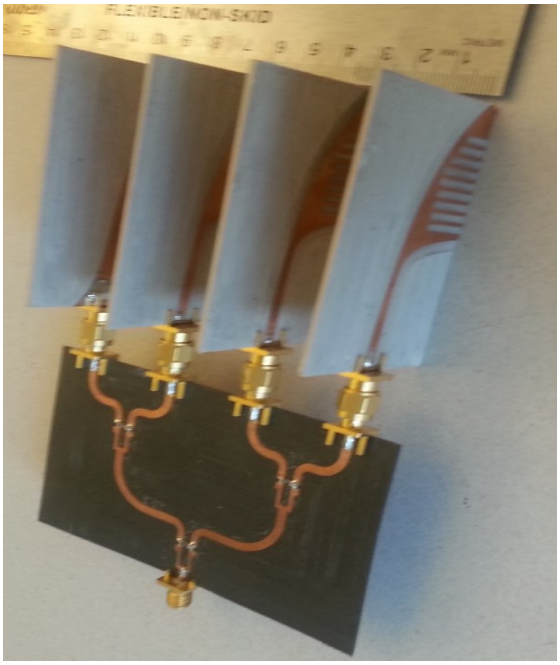

Figure 4.16 The fabricated 4-element array system.

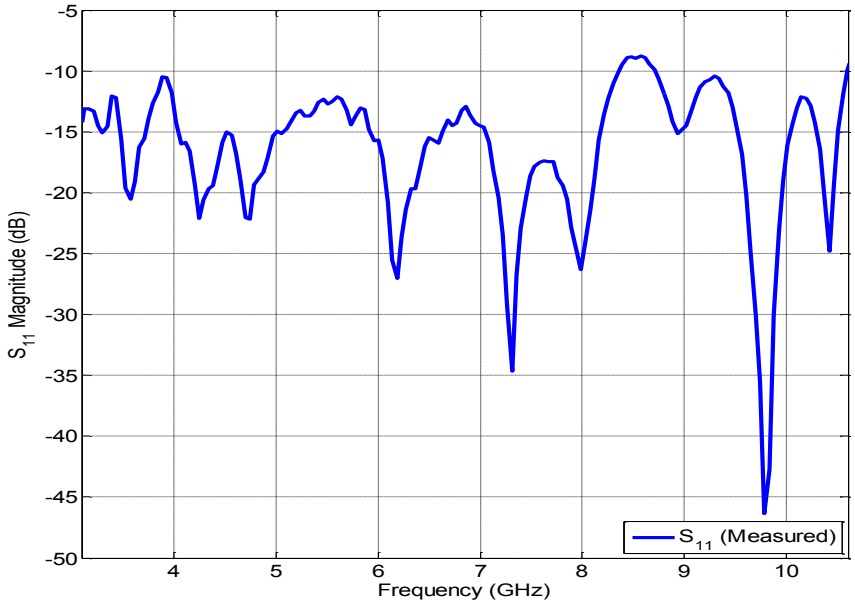

Figure 4.17 Measured reflection coefficient S_{11} of the antenna system.

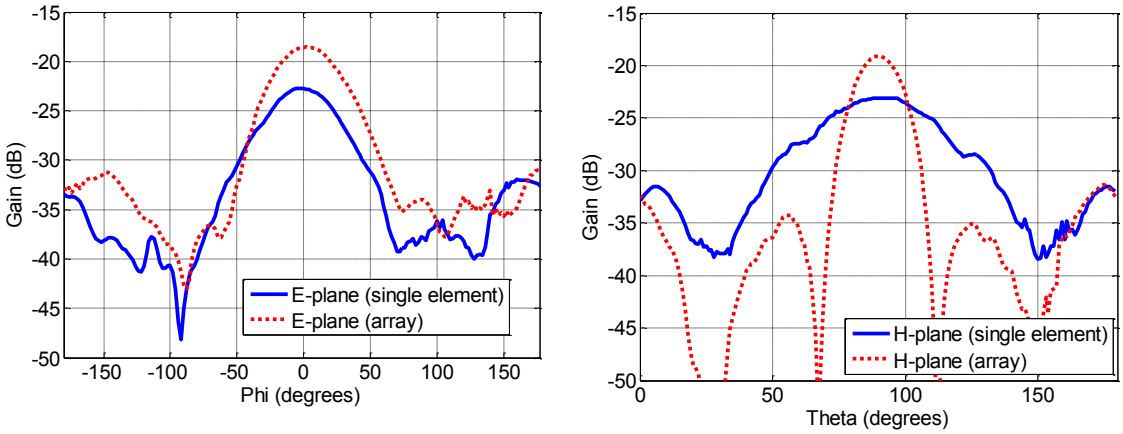

(a)

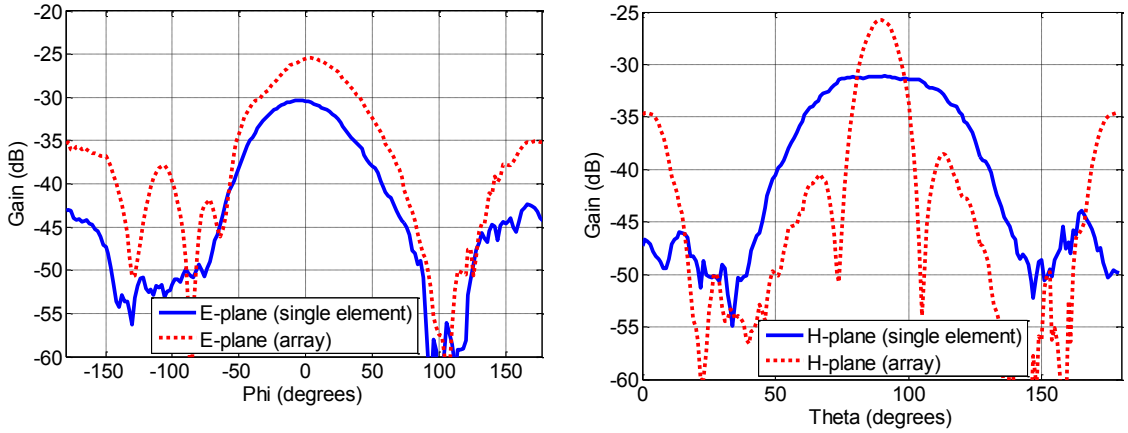

(b)

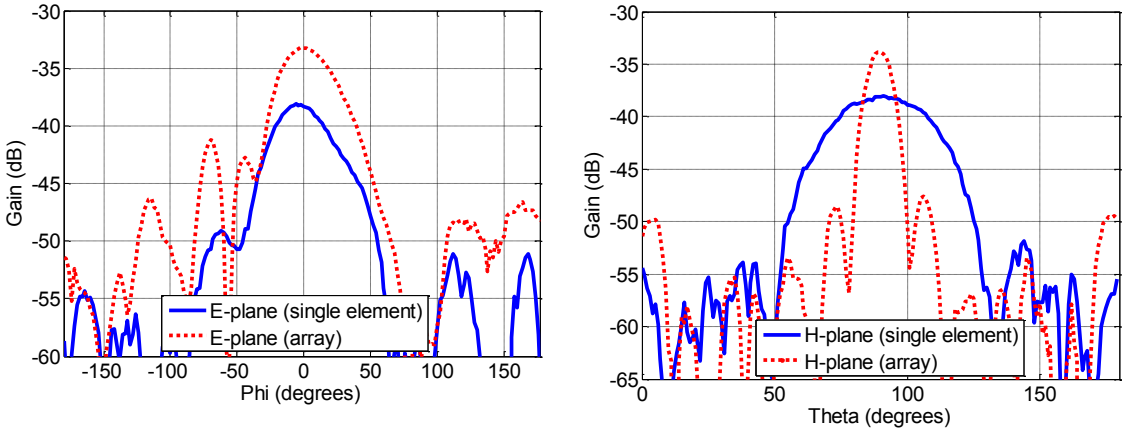

(c)

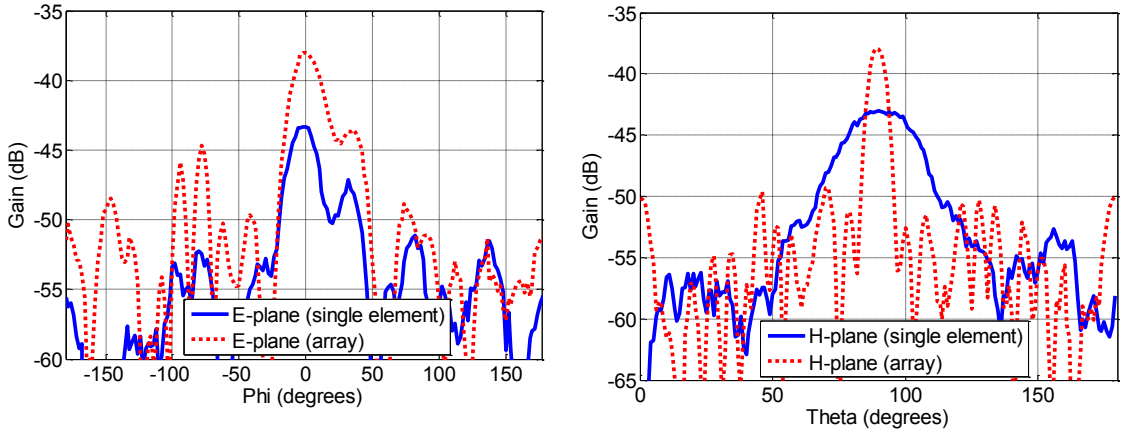

(d)

Figure 4.18 Measured E-Plane and H-plane radiation patterns at (a) 3 GHz, (b) 5 GHz, (c) 7 GHz, (d) 9 GHz.

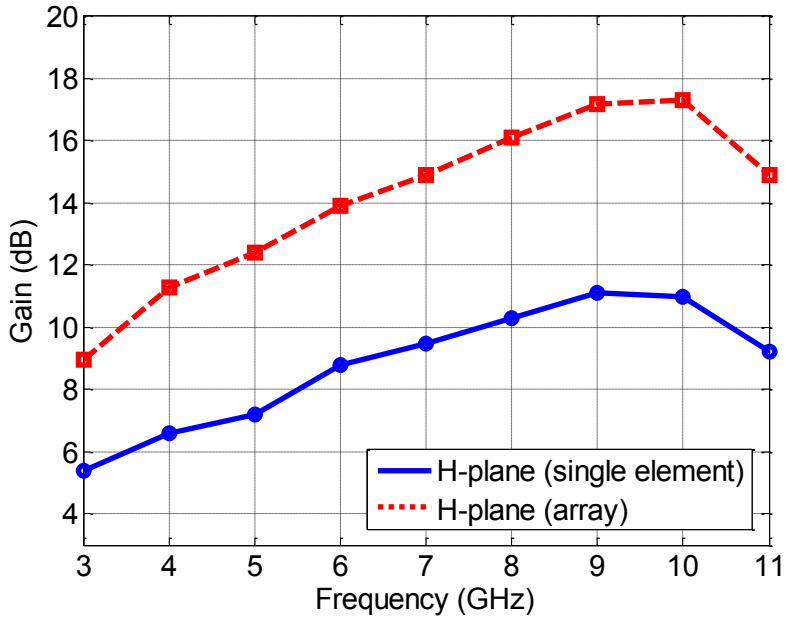

Figure 4.19 Total realized gain comparison between the single BAVA antenna and the 4-element array.

4.5 Summary

In this chapter, four different UWB antennas have been designed, optimized and fabricated using PCB technology. The first three slot-coupled antenna prototypes show very good performance in terms of gain stability, impedance bandwidth, and group delay. It can be noticed that prototype with a circular radiator exhibits a slightly better gain stability compared with the other prototypes. However, all these prototypes are considered good candidates for UWB applications. For more precise detection / imaging applications, a high-gain UWB BAVA antenna have been realized. Based on the BAVA antenna design, a 4-element array is developed. The array achieved a realized gain of 15 dB. For all designs, the experimental results show a very good agreement with the simulations.

Chapter 5

MMW Antenna Probes

5.1 Introduction

The design and realization of an efficient MMW antenna sensor is urgent for high performance detection / imaging systems. Such antenna probes should be characterized by a directive main beam, high radiation efficiency and stable gain and radiation patterns over the operating band, and good impedance matching.

In this chapter, multiple MMW antenna probes are introduced. The proposed antennas satisfy the above-mentioned requirements. Many gain enhancing techniques including: hybridization and the array principle have been adopted in order to realize such antenna sensors for imaging applications.

5.2 Hybrid Antennas

This section represents in detail multiple antenna configurations based on hybridization as a gain enhancing technique. These hybrid designs include open-ended waveguide / microstrip patch, microstrip patch / conical horn, horn / DRA, and x-slot /conical horn.

5.2.1 Open Ended Circular Waveguide / Patch Hybrid Antenna

Fig. 5.1 shows the geometry of the proposed design presentenced in [C4]. A printed microstrip circular patch is used to excite a mounted metallic open-ended circular waveguide. The waveguide is fabricated using a very thin copper sheet with a thickness 0.254 mm folded to form a 4.725 mm high cylinder with 4.5 mm radius.

The copper sheet waveguide is used to replace the heavy metallic waveguides. The waveguide thin wall acts here similar to the thick one because of the small skin depth at MMW frequencies. The skin depth within the operating frequency band is much less than the metallic wall thickness, which keeps the overall weight of the antenna much lighter than using bulky metallic waveguides without any performance deterioration.

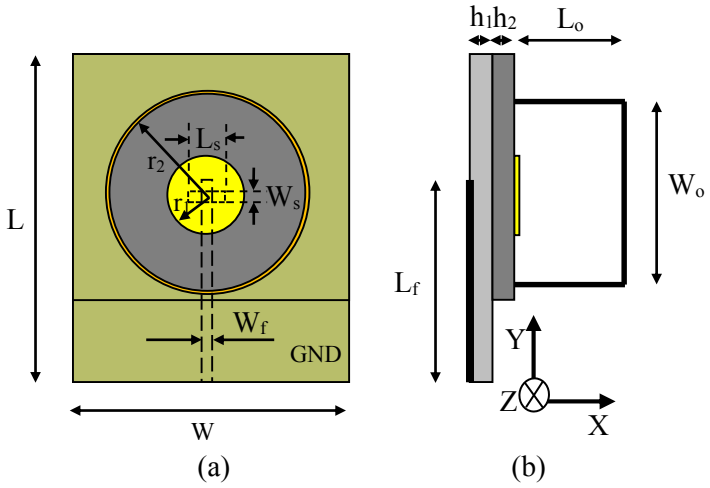

Figure 5.1 Geometry of the proposed antenna (a) front view (b) side view.

Some parametric studies have been carried out using CSTMWS to address the effect of both circular waveguide radius r_2 and its height L_o. It is found that increasing r_2 enhances the total realized gain in the range from 29 GHz to 32 GHz linearly due to increasing the physical radiation aperture, while it can be noticed that increasing r_2 more than 4.5mm causes the gain to drop in the lower operating band of the antenna (from 28 GHz to 29 GHz). The effect of r_2 on the antenna resonance is remarkably small, where any radius increment leads to a small shift in the main resonance of the reflection coefficient S_{11} to lower frequency maintaining the antenna matching at a proper level. Figs. 5.2 and

5.3 show the simulated reflection coefficient and the gain for different r_2 values with fixed all other parameters fixed.

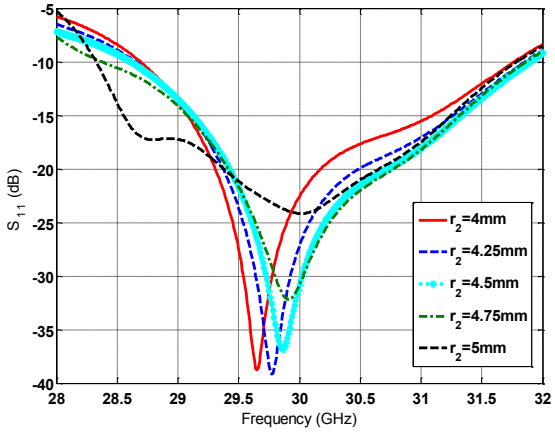

Figure 5.2 Waveguide radius effect on the reflection coefficient.

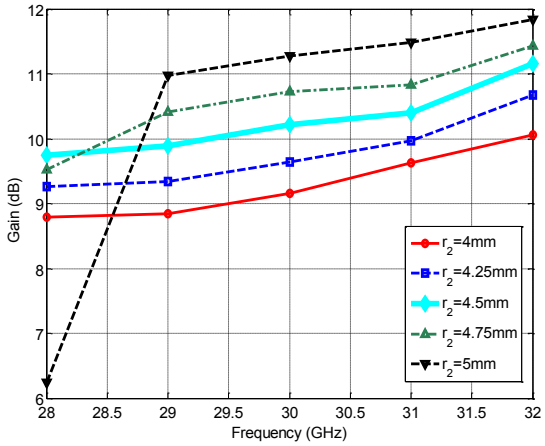

Figure 5.3 Waveguide radius effect on the antenna gain.

Figs. 5.4 and 5.5 illustrate the effect of L_o on both the reflection coefficient and the antenna gain, respectively. It can be concluded that the waveguide height L_o controls both the antenna impedance matching and the radiation matching from the antenna aperture to free space. The best value of L_o ,in terms of the gain, is found to be 7.875 mm which is almost (3/4λ) at 30 GHz, However, for keeping low profile antenna and for some fabrication considerations the L_o is chosen to be 4.725 mm. All the optimized parameters using HFSS and CSTMWS of the antenna prototype are shown in Table 5.1. A photograph of the fabricated antenna prototype is shown in Fig. 5.6.

Fig. 5.7 shows a comparison between the measured and the calculated reflection coefficients S_{11} for the proposed design. The designed antenna exhibits an impedance bandwidth of 3.1 GHz from 28.9 GHz to 32 GHz with a center frequency of 30.5 GHz (HFSS) and an impedance bandwidth of 3.2 GHz from 28.6 GHz to 31.9 GHz with a center

frequency of 29.9 GHz (CSTMWS), However, for the experimental results the antenna bandwidth extends from 28.4 GHz to 31.3 GHz with a center frequency of 28.7 GHz. The difference between the simulated results and the measured one can be accounted to the approximations in the geometrical and feeding models used in numerical simulators in addition to some fabrication imperfections including soldering, connector dimensions tolerance, etc.

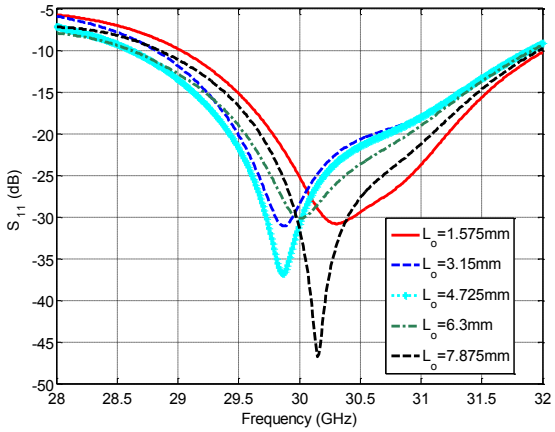

Figure 5.4 Waveguide height L_o effect on the reflection coefficient.

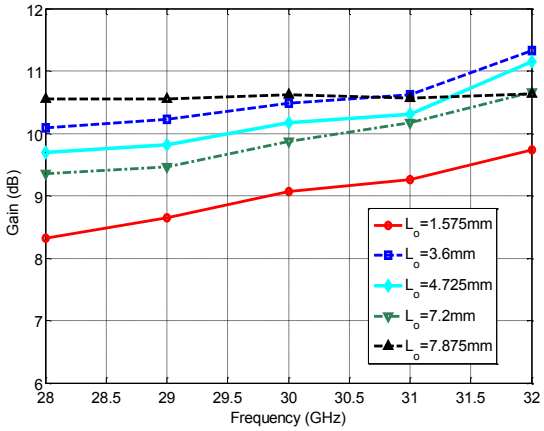

Figure 5.5 Waveguide height L_o effect on the antenna gain.

Fig. 5.8 shows the reflection coefficient S_{11} comparison between the circular patch antenna alone and the hybrid antenna configuration (patch and open ended waveguide). It can be noticed that there is a 0.5 GHz frequency shift which may be due to the loading effect, while the bandwidth is still almost the same. Fig. 5.9 illustrates the gain enhancement after using the hybrid configuration. The overall antenna gain for the hybrid configuration increased by more than 3 dB compared with the circular patch antenna only.

Table 5.1 The optimized dimensions of the antenna in (mm).

Parameter	*W*	*L*	W_s	L_s	h_1	h_2	W_f	L_f	W_o	L_o	r_1	r_2
Value	*15*	*20*	*0.25*	*2.3*	*0.635*	*0.7874*	*0.65*	*10.64*	*15*	*4.725*	*1.53*	*4.5*

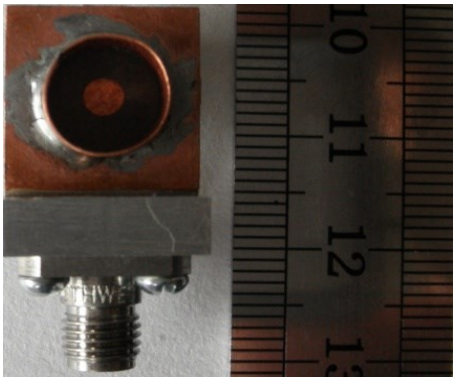

Figure 5.6 Photograph of the fabricated antenna prototype.

For practical measurement of the constructed antenna gain, a standard horn antenna is used as a receiving probe measuring the transmitted power from the antenna under test (AUT) at a distance *R*. The distance between the two antennas *R* should be chosen to be greater than ($2D^2/\lambda$) for any frequency in the operating range for ensuring farfield operation, where *D* is the largest antenna dimension which is equals to r_1 in this design. Then Friis' transmission equation, given by (5.1), can be applied for evaluating the gain of the AUT. There is a good agreement between the theoretical and measured gain of the proposed antenna as shown in Fig. 5.10.

$$|S_{21}| = \frac{P_t}{P_r} = G_t G_r \left(\frac{\lambda}{4\pi R}\right)^2 \cdot \tag{5.1}$$

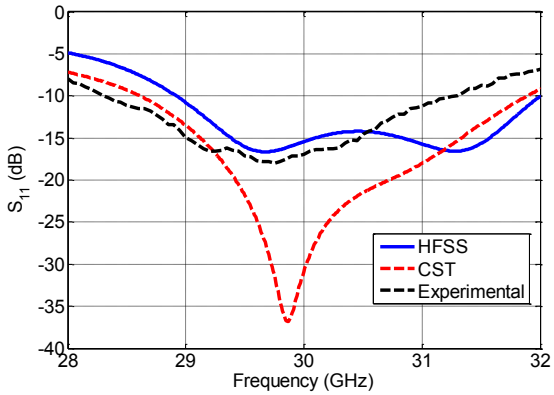

Figure 5.7 Reflection coefficient S_{11} of the proposed antenna.

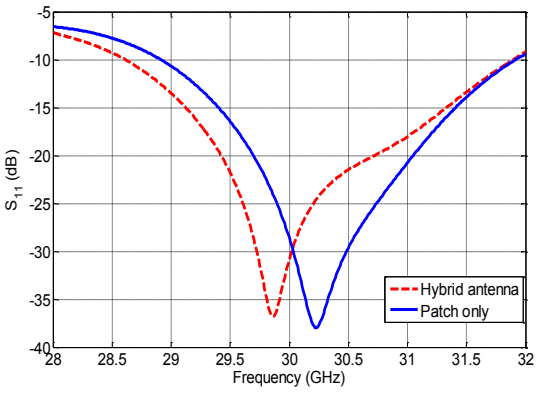

Figure 5.8 Reflection coefficient S_{11} comparison between the patch alone and the hybrid antenna (patch and open ended waveguide).

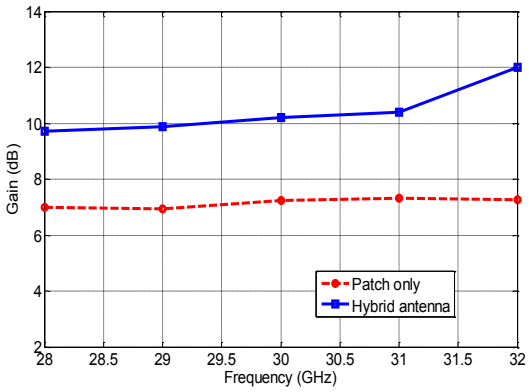

Figure 5.9 CST simulated gain comparison between the patch alone and the hybrid antenna.

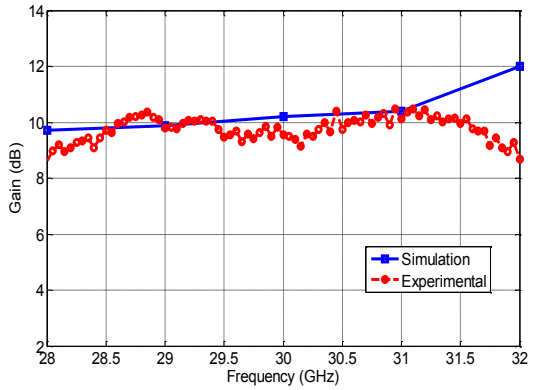

Figure 5.10 Measured vs. Simulated gain of the proposed hybrid antenna.

The measured and the calculated E-plane and H-plane radiation patterns for the proposed antenna at frequencies 30 GHz, 31 GHz are shown in Fig. 5.11 and Fig. 5.12, respectively. The antenna exhibits a low side lobe levels (less than -13dB) in both the E-plane (x-z) and H-plane (x-y) and it has broadside directive patterns with a HPBW of 50°, 30° in both E and H planes respectively. Finally, the antenna shows good radiation pattern stability over the impedance bandwidth.

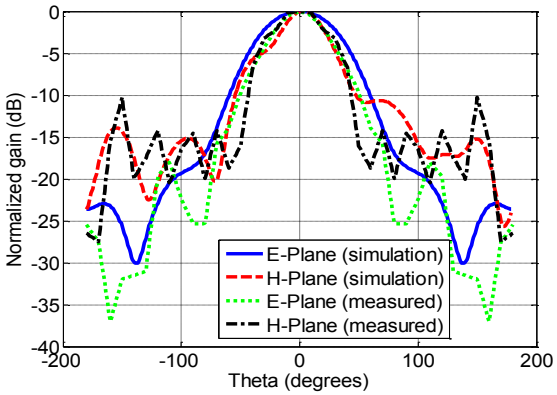

Figure 5.11 E-plane (x-z) and H-plane (y-z) radiation patterns for the proposed antenna at 30 GHz.

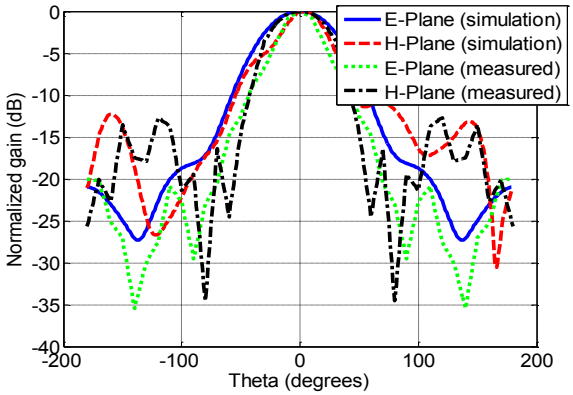

Figure 5.12 E-plane (x-z) and H-plane (y-z) radiation patterns for the proposed antenna at 31 GHz.

5.2.2 Hybrid Microstrip / Conical Horn Antenna

In the design shown in Fig. 5.13 [J2], a circular patch radiator is used to feed a thin wall metallic surface mounted conical horn. The horn has a great effect on enhancing the overall gain of the antenna without a great impact on the center frequency or the operating bandwidth. The prototype weight is still light compared with the standard horn antennas operating in the same range. The horn is fabricated using a very thin copper sheet, with a thickness of 0.254 mm, folded to form a circular conical shape with a top radius of 6.5 mm and bottom one of 2.5 mm. The thin wall horn acts similar to the thick one because of its small skin depth at MMW frequencies, which can be accounted for the small skin depth of the copper at MMW frequencies. This approach keeps the overall weight of the antenna much lighter than using bulky metallic horns without any significant impact on the overall performance. The choice of the circular patch radius r_p and the coupling slot length L_s is considered as the first step of this antenna design due to their dominant effect on the antenna resonant frequency. The primary value for r_p and L_s are chosen to be quarter wave

length at the antenna resonance of 31 GHz, and then by using the CSTMWS optimizer the proper dimensions are obtained. In addition, parametric studies are carried out using CSTMWS and HFSS to address the effect of the horn height (h_c) and its top-radius (r_c) on the antenna performance. Figs. 5.14 and 5.15 show the simulated reflection coefficient and the gain for different r_c values while other parameters are fixed. It can be concluded that increasing r_c enhances the total realized gain in the range from 28 GHz to 32 GHz mainly by increasing the physical radiation aperture. However, the effect of r_c on the antenna resonance is remarkably small.

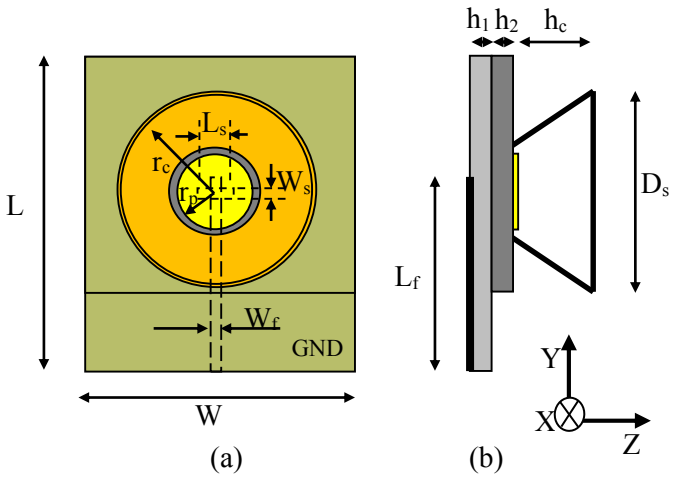

Figure 5.13 Geometry of the proposed antenna (a) front view (b) side view.

Figs. 5.16 and 5.17 illustrate the effect of h_c on both the reflection coefficient and the antenna gain, respectively. It can be noticed that the waveguide height h_c controls both the antenna impedance matching and the antenna gain. An optimum value of h_c, in terms of the gain, is found to be 6.3mm. However, for some fabrication considerations and higher gain values at the lower end of the considered frequency band, it is chosen to be 7.875mm.

The optimized antenna prototype parameters using the two different simulators are shown in Table 5.2. A photograph of the fabricated antenna prototype is shown in Fig. 5.18.

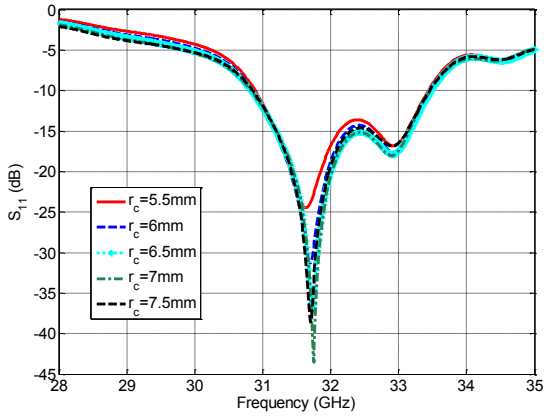

Figure 5.14 Horn top-radius "r_c" effect on the reflection coefficient.

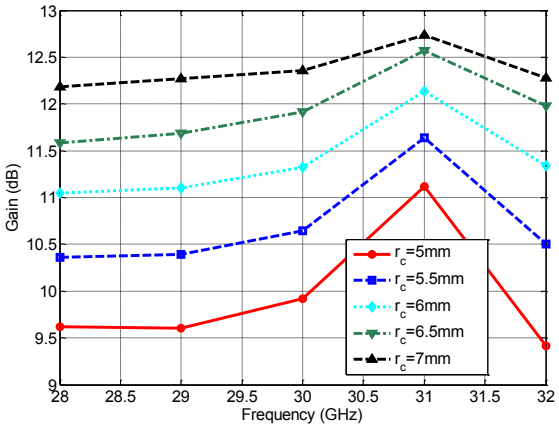

Figure 5.15 Horn top-radius "r_c" effect on the antenna gain.

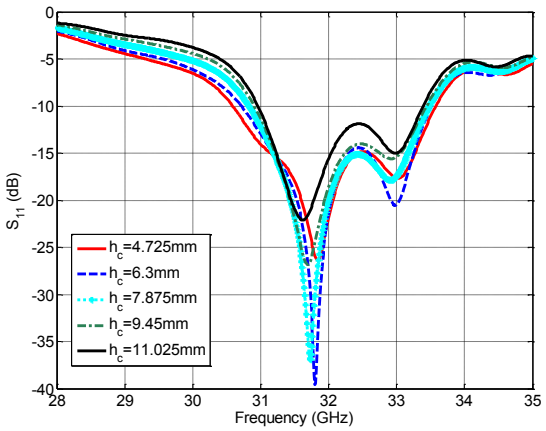

Figure 5.16 Horn height "h_c" effect on the reflection coefficient.

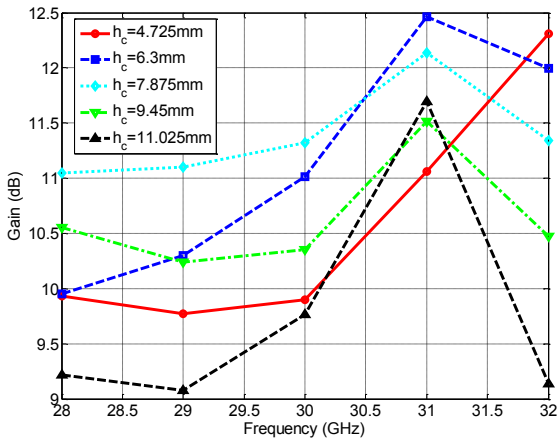

Figure 5.17 Horn height "h_c" effect on the antenna gain.

Table 5.2 Optimized dimensions of the proposed antenna (in mm).

Parameter	W	L	W_s	D_s	h_1	h_2	W_f	L_f	h_c	r_c	r_p	L_s
Value	*15*	*20*	*0.25*	*13*	*0.635*	*0.7874*	*0.65*	*10.64*	*7.875*	*6.5*	*1.48*	*2.3*

Fig. 5.19 shows a comparison between the measured and the calculated reflection coefficients S_{11} for the proposed design. HFSS results show that the antenna exhibits an impedance bandwidth of 1.7 GHz starts from 31.6 GHz to 33.3 GHz with a center frequency of 32.5 GHz while the simulated results using CSTMWS show an impedance bandwidth of 3 GHz starts from 30.4 GHz to 33.4 GHz with a center frequency of 31.2 GHz. However, the experimental results show that the antenna bandwidth extends from 30.3 GHz to 33.6 GHz with a center frequency of 31.25 GHz.

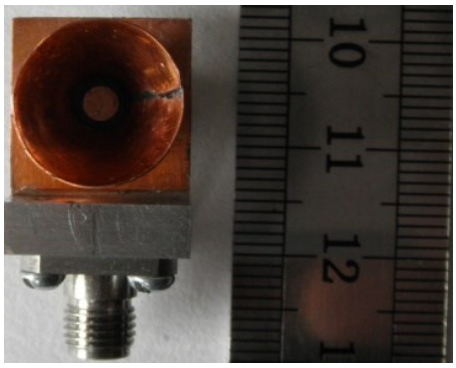

Figure 5.18 A Photograph of the fabricated antenna prototype.

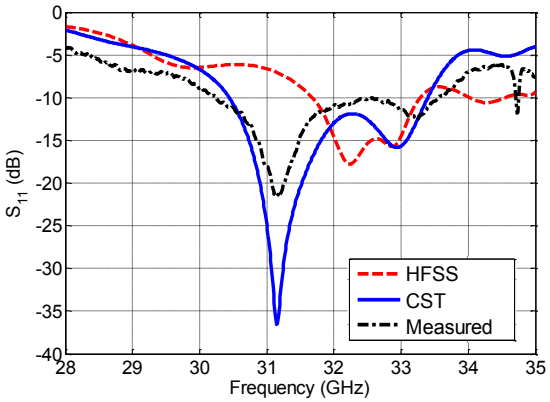

Figure 5.19 Reflection coefficient S_{11} comparison between the patch alone and the hybrid antenna.

Differences between simulated and measured results can be attributed to several potential parameters including the approximations and discretization used by the numerical methods implemented in CSTMWS and HFSS simulators. Methods used for simulators port modeling, where CSTMWS uses discrete ports while HFSS uses lumped ports, together with associated numbers of excited modes are also expected to have some effects on the simulated results. In addition, some fabrication imperfections including soldering, horn dimensions tolerance, etc., might cause differences between the measured and simulated prototypes.

Fig. 5.20 shows the CSTMWS simulated reflection coefficient S_{11} comparison between the circular patch antenna alone and the hybrid antenna configuration (patch and conical horn). It can be noticed that there is a 0.07 GHz frequency shift which may be due to the loading effect, while the bandwidth is still almost the same. Fig. 5.21 illustrates the gain enhancement after using the hybrid configuration and the measured gain of the fabricated prototype. The CSTMWS simulated total realized antenna gain for the hybrid configuration increased by more than 3 dB compared with the circular patch antenna only.

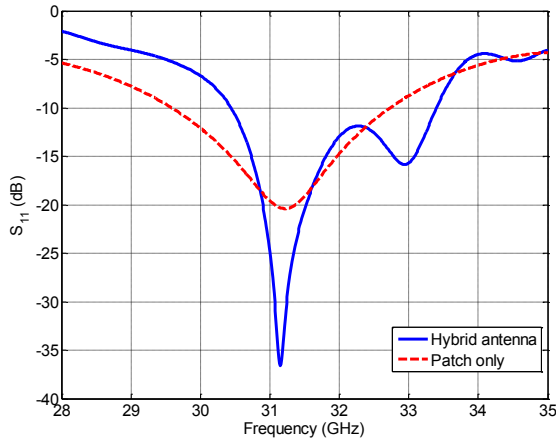

Figure 5.20 CSTMWS simulated S_{11} Reflection coefficient comparison between the DRA only and the hybrid configuration.

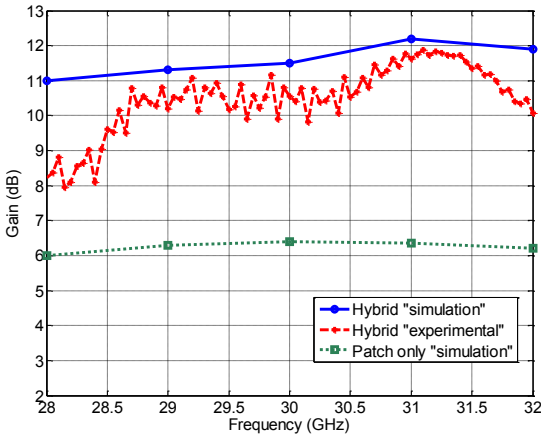

Figure 5.21 Gain comparison between the patch antenna alone vs. the hybrid antenna and the actual measured gain for the fabricated prototype.

As shown in Figs. 5.22 and 5.23, there is a good agreement between the CSTMWS and HFSS simulated, and measured E-plane (x-z) and H-plane (y-z) radiation patterns for the proposed antenna at 31 GHz. However, the presence of some discrepancies in the side lobes which can be accounted to some fabrication imperfections and some unexpected reflections from the pattern measuring system. The antenna exhibits a broadside directive

patterns in both E-plane and H-plane with good radiation pattern stability over the impedance bandwidth.

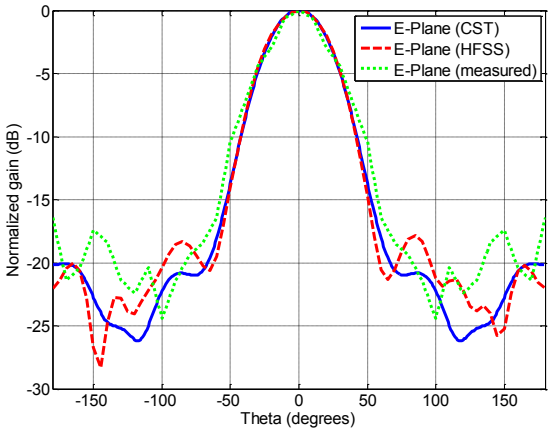

Figure 5.22 Measured E-plane (x-z) radiation pattern for the proposed antenna at 31 GHz.

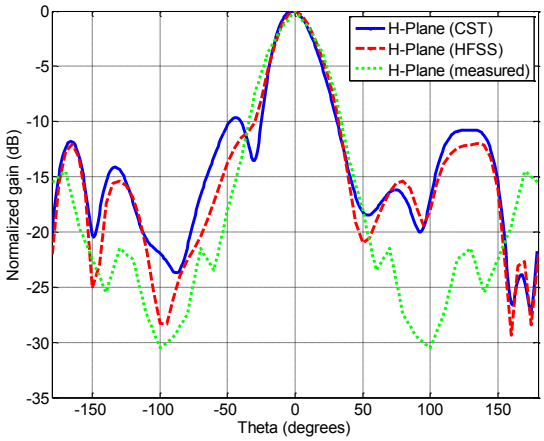

Figure 5.23 Measured H-plane (y-z) radiation pattern for the proposed antenna at 31 GHz.

5.2.3 Hybrid DRA / Conical Horn Antenna

In the design presented in [C9], a cylindrical DRA is placed on the ground plane of a high permittivity ε_{r1}=10.2 substrate with a 0.635 mm thickness. The DRA resonator is chosen to reduce the metallic losses associated with metallic radiators. It is fed by a 50Ω microstrip line on the backside of the substrate through a rectangular aperture etched in the ground plane. This feeding mechanism excites the mode HEM11δ in the circular DRA which feeds a thin-wall surface-mounted conical antenna with a smaller radius of 2.5 mm, 6.5 mm larger radius and is 4.725 mm high. The DRA is made of Rogers 3010 with ε_r=10.2. The schematic diagram of the proposed antenna is shown in Fig. 5.24. The surface-mounted circular cone has a great effect on enhancing the overall gain of the antenna without a great

impact on the center frequency or the operating bandwidth. The prototype weight is still very light compared with ordinary horn antennas. All the optimized parameters are shown in Table 5.3.

Fig. 5.25 shows the experimental and calculated reflection coefficient S_{11} against the frequency for the proposed hybrid configuration. The designed antenna exhibits an impedance bandwidth of 2.8 GHz starts from 28.4 GHz to 31.2 GHz (HFSS) and an impedance bandwidth of 1.6 GHz starts from 29.1 GHz to 30.7 GHz (CSTMWS). The measured reflection coefficient shows a measured bandwidth of 1.5 GHz starts from 29.2 GHz to 30.7 GHz. This discrepancy in the measured antenna performance can be accounted to some fabrication issues, including the improper alignment of the surface mounted horn and the DRA, besides the adhesive material effect under the DRA. Fig. 5.26 indicates the loading effect on the reflection coefficient S_{11} of the DRA radiator after and before integrating the surface mounted horn. It can be noticed that there is a 1.2 GHz frequency shift between them, which can be accounted to the loading effect, while the bandwidth is still the same. The calculated E-plane and H-plane radiation patterns for the proposed hybrid antenna at frequencies 29 GHz, 30 GHz are shown in Fig. 5.27 and Fig. 5.28, respectively.

The proposed antenna also exhibits a broad side directive patterns in both E-plane and H-plane with good radiation pattern stability over the impedance bandwidth. The total realized antenna gain for the hybrid configuration increased by nearly 5.5 dB compared with the circular DRA antenna only. Fig. 5.29 illustrates the gain enhancement after using the hybrid configuration. A photograph of the fabricated antenna prototypes is shown in Fig. 5.30.

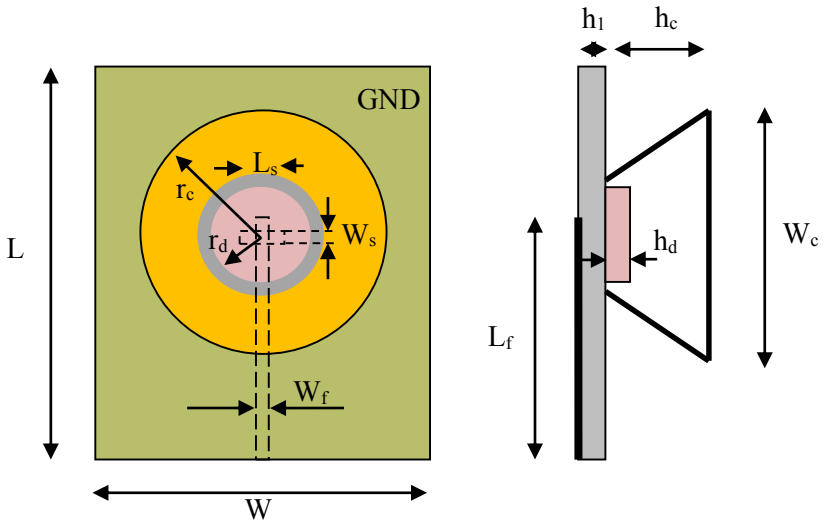

(a) (b)

Figure 5.24 Geometry of the hybrid DRA / conical antenna (a) front view (b) side view.

Table 5.3 Optimized dimensions for DRA / conical horn antenna (in mm).

Parameter	*W*	*L*	W_s	L_s	h_c	h_1	W_f	L_f	W_c	h_d	r_d	r_c
Value	*15*	*20*	*0.25*	*2.3*	*7.875*	*0.635*	*0.65*	*10.64*	*13*	*1.28*	*1.53*	*6.5*

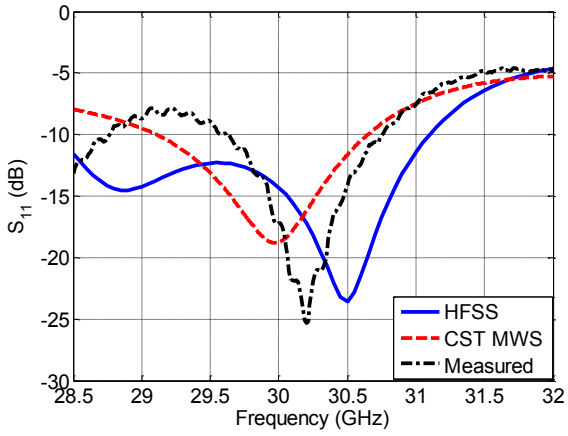

Figure 5.25 Reflection coefficient S_{11} of the proposed hybrid antenna.

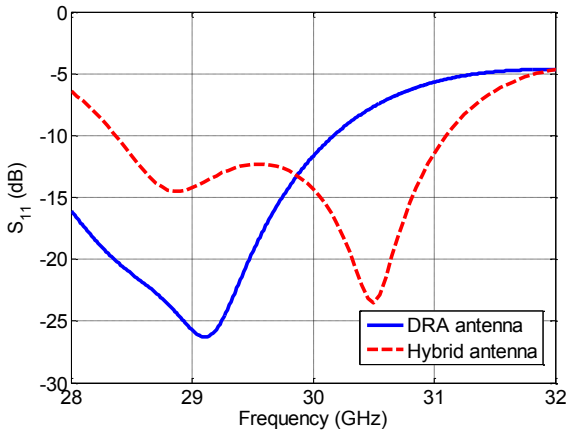

Figure 5.26 Reflection coefficient S_{11} comparison between the DRA only and the hybrid configuration.

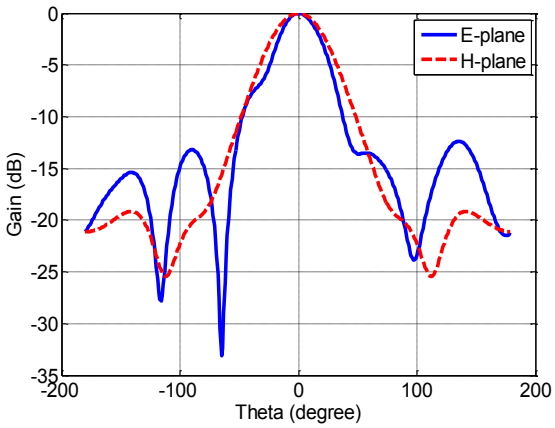

Figure 5.27 Calculated E-plane (blue solid) and H-plane (red dashed) radiation patterns for the hybrid antenna at 29 GHz.

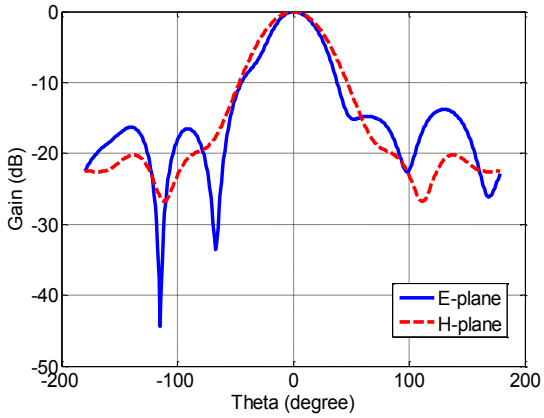

Figure 5.28 Calculated E-plane (blue solid) and H-plane (red dashed) radiation patterns for the hybrid antenna at 30 GHz.

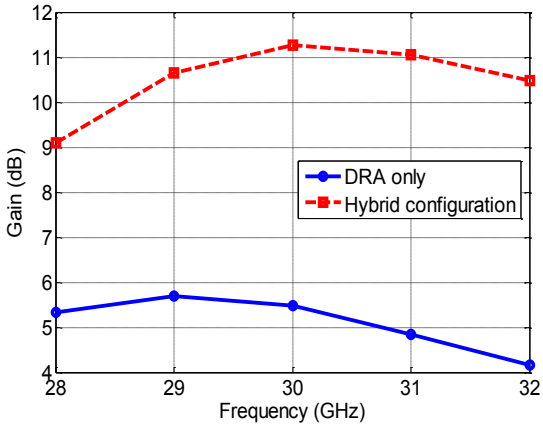

Figure 5.29 Total realized gain comparison between the DRA alone and the hybrid antenna.

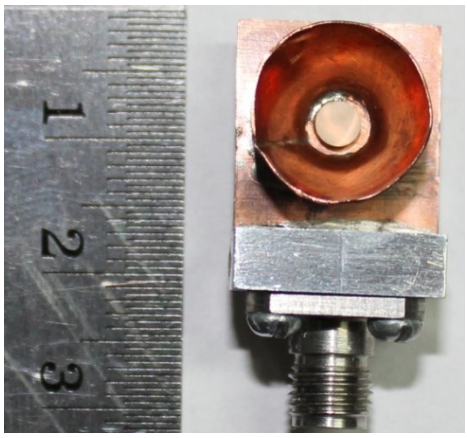

Figure 5.30 A photograph of the proposed hybrid antenna.

5.2.4 Hybrid X-Slot / Conical Horn Antenna

The schematic diagram of the design, presented in [C7], and [J5], is shown in Fig. 5.31. The proposed antenna consists of an x-shaped slot with unequal arms etched on top metal layer of a 0.5-mm-thick substrate (Rogers RT5880) with ε_r = 2.2 and backed by SIW circular cavity formed by vertical vias penetrating through the substrate. A surface mounted

conical horn is placed over the center of the x-shaped slot. The horn focuses the energy radiated from the x-slot into a narrow beam, which has a great effect on the overall antenna gain. Loading effect due to the surface mounted horn can be avoided by the proper choice of the cone height The conical horn is manufactured using a thin copper sheet with a thickness = 0.254 mm folded to form a circular conical shape with a top radius of 9 mm and bottom one of 4 mm. Using a thin wall thickness for the horn will not result in any power leakage, where the skin depth at MMW frequencies is much less than the physical horn wall thickness. The circular cavity surrounding the x-slot is opened from one side to enable strong slot excitation through rectangular SIW waveguide which is fed by a 50Ω microstrip line. In order to assure a smooth power transfer from the microstrip line to the SIW, a *λ/4* tapered line transformer is used. The rectangular SIW waveguide and the SIW cavity designs are very critical to obtain a stable performance close to metallic waveguides. The via design and the separation between any two adjacent vias are adjusted according two Eq. (3.24), and Eq. (3.25). The optimized dimensions of the proposed antenna prototype are tabulated in Table 5.4.

In order to verify and optimize the proposed design prior to fabrication stage, two different simulators have been used: the frequency domain solver HFSS and the time domain solver CSTMWS. Fig. 5.32 presents a comparison between measured and simulated reflection coefficient $|S_{11}|$ for the proposed design with the optimized dimensions for the x-slot antenna without the surface mounted horn. It can be noticed 1 GHz frequency shift between the simulated and measured data when considering the default value of the substrate permittivity in the simulators, i.e. $\varepsilon_r = 2.2$. This shift can be corrected if the substrate permittivity reduced by 8% in the simulations, i.e. $\varepsilon_r = 2.024$. The default value

of the substrate permittivity stated in the datasheets is measured at 10 GHz. However, its variation at MMW frequencies "greater than 30 GHz" can be considered as a physical phenomenon reported in [123], and [124] and documented by Rogers Corp. in [125]. The designed antenna, before mounting the horn, exhibits an impedance bandwidth of more than 1.4 GHz from 36 GHz to 37.4 GHz.

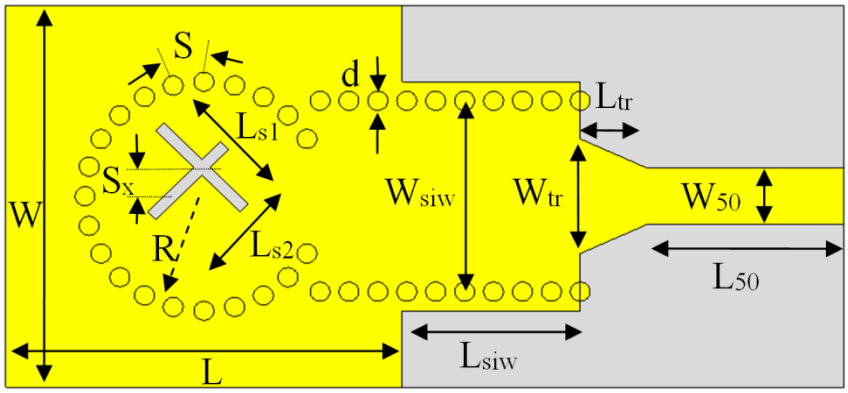

(a)

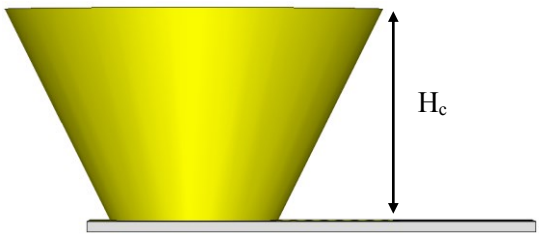

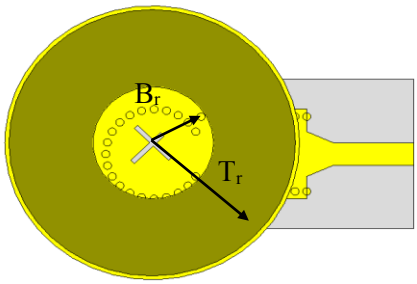

(b) (c)

Figure 5.31 Schematic diagram of the proposed antenna (a) Top view without horn (b) side view with the horn (c) top view with the horn.

Table 5.4 Optimized dimensions for hybrid x-slot / conical horn antenna (in mm).

parameter	*R*	*L*	L_{50}	L_{s1}	L_{s2}	L_{siw}	L_{tr}	*W*	W_{slot}	W_{tr}	S_x	*S*	*d*	B_r	T_r	H_c
Value	*3*	*10*	*3*	*3*	*2.6*	*4.5*	*1.66*	*10*	*0.3*	*3*	*0.7*	*0.76*	*0.5*	*4*	*9*	*10*

Position orientation of the surface mounted horn over the slot was a great challenge. There were two possible locations to mount the horn to be concentric either with the SIW cavity or with the x-slot center. Through simulations, we found that the second location was the optimal position, where placing the horn around the cavity center results in a main beam deflection of 10 degrees from the broadside direction. The reflection coefficient $|S_{11}|$ of the proposed antenna with the surface mounted circular horn, with and without substrate correction, is shown in Fig. 5.33. The fabricated prototype shows a very good impedance matching from 36.25 GHz to 37.25 GHz. The measured impedance bandwidth is 1.05 GHz at the resonant frequency of 36.7 GHz. A photograph of the fabricated antenna prototypes with and without the horn is illustrated in Fig. 5.34.

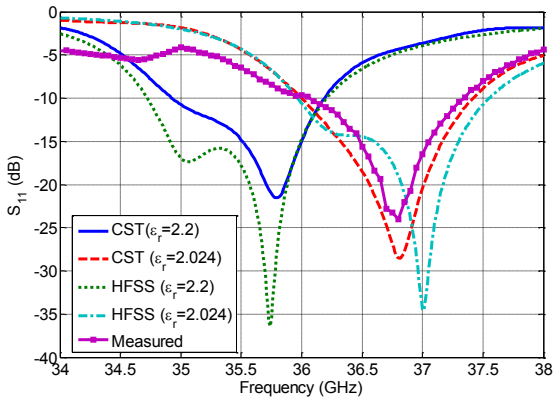

Figure 5.32 Measured and simulated reflection coefficient $|S_{11}|$ of the x-slot antenna without the surface mounted horn.

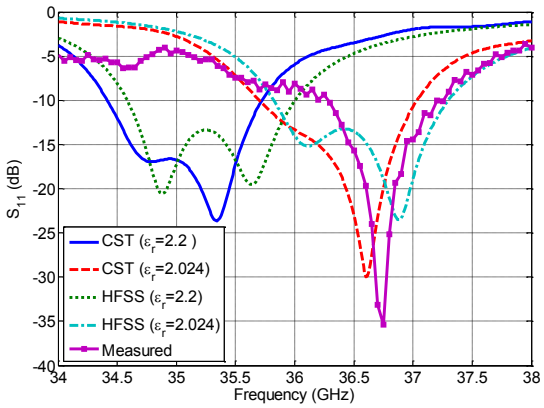

Figure 5.33 Measured and simulated reflection coefficient $|S_{11}|$ of the x-slot antenna with the surface mounted horn.

A noticeable gain enhancement of more than 15 dB is achieved after mounting the horn, for both simulation and experimental results. Fig. 5.35 illustrates the conical horn effect on the total realized gain of the proposed antenna. More than 7.5 dB of gain increment is obtained after placing the horn. The calculated axial ratio, after and before

mounting the horn, is shown in Fig. 5.36. It can be concluded that the lowest value of axial ratio value after mounting the horn is 1.25dB at 36.45 GHz (HFSS) and 1.3 dB at 36.25 GHz (CSTMWS) which is still located within the impedance bandwidth of the proposed antenna.

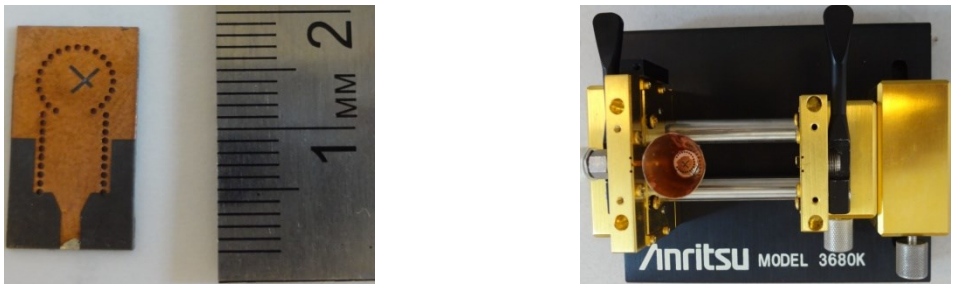

(a) (b)

Figure 5.34 Photograph of the fabricated prototypes (a) without horn (b) with horn.

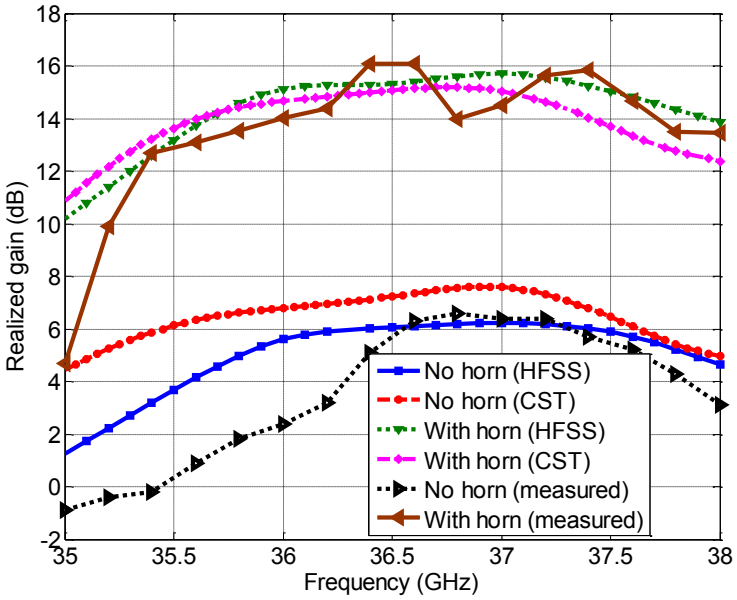

Figure 5.35 Total realized gain comparison between the proposed antenna with and without horn.

The proposed antenna prototype has very stable radiation patterns over the

operating band. Figs. 5.37-5.38 show the measured and simulated E and H-plane radiation patterns at 36.7 GHz before mounting the horn including both phi and theta components. As illustrated in Figs. 5.39-5.40, the proposed antenna becomes more directive after adding the horn in both E and H-plane with sidelobe level (SLL) around -15 dB. Very good agreement between the calculated patterns obtained from both simulators. However, there are some discrepancies, especially in the back lobes of the patterns, which can be accounted to the presence of the test fixture and the mounting support inside the anechoic chamber.

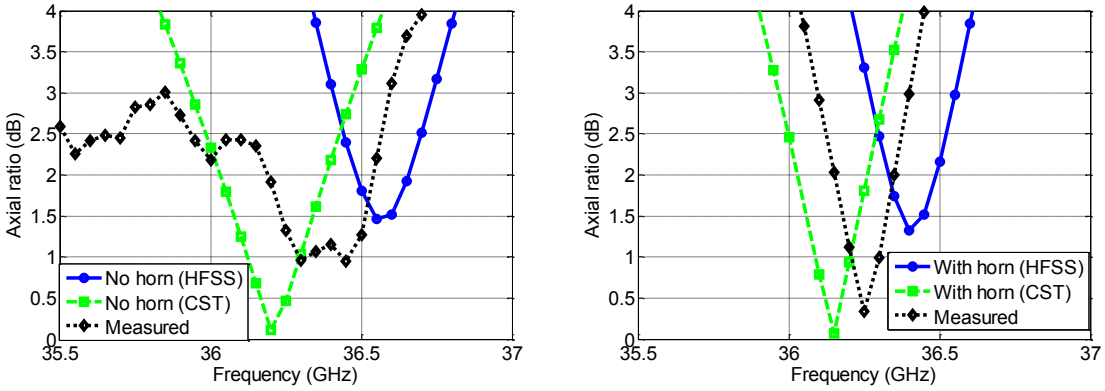

(a) (b)

Figure 5.36 Axial ratio of the proposed design (a) without horn (b) with horn.

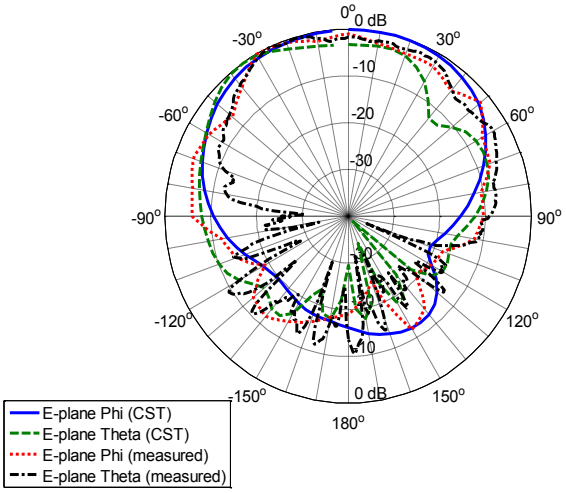

Figure 5.37 Measured and simulated E-plane (x-z) radiation patterns of the proposed antenna without surface mounted horn.

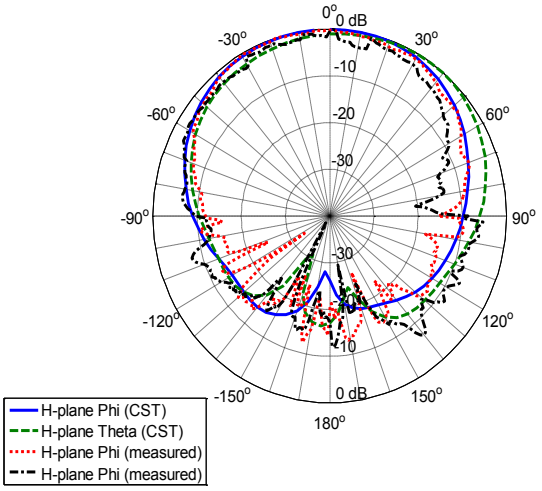

Figure 5.38 Measured and simulated H-plane (y-z) radiation patterns of the proposed antenna without horn.

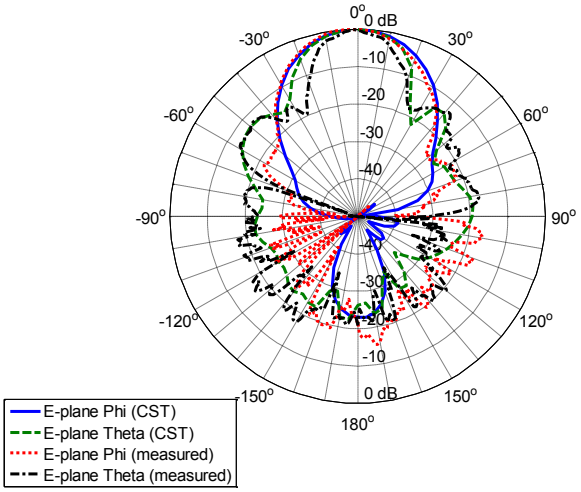

Figure 5.39 Measured and simulated E-plane (x-z) radiation patterns of the proposed antenna with surface mounted horn.

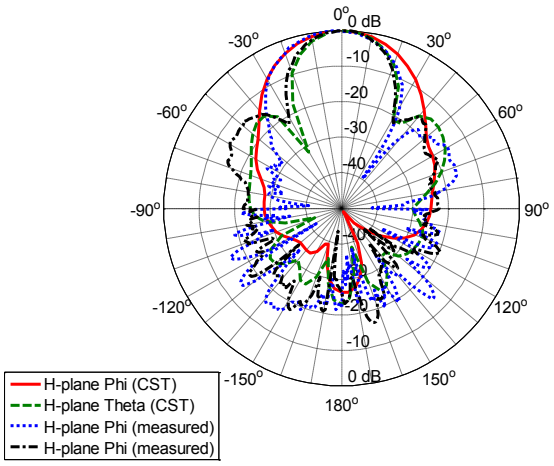

Figure 5.40 Measured and simulated H-plane (y-z) radiation patterns of the proposed antenna with surface mounted horn.

5.3 Summary

In this chapter, multiple hybrid MMW antenna sensors have been presented. These designs are simulated and optimized using both HFSS and CSTMWS simulators prior to the fabrication process. The proposed hybrid designs include circular waveguide / microstrip patch, DRA / microstrip patch, microstrip patch / conical horn, DRA / conical horn and x-slot / conical horn. All the illustrated designs show very stable radiation patterns, high realized gain (greater than 10 dB), and good impedance matching over the operating band. The antennas weight and size are small compared with classical horn antennas which allow integration and forming arrays for increasing the overall gain. Given these characteristics, these antenna prototypes could be employed as a MMW scanning sensors for detection / imaging applications.

Chapter 6

Applications to Detection / Imaging of Hidden Objects

6.1 Introduction

This chapter is divided into two main sections. The first one introduces the UWB gap detection and Imaging / detection of a hidden target behind a wall, while the second focuses mainly on MMW imaging / detection results for hidden weapons detection / imaging applications. Both sections explain the setup used in the experiments and discuss the performance, accuracy, and reliability of these systems.

6.2 UWB Imaging / Detection

UWB technology has been used for some time in Ground Penetrating Radar (GPR) applications [25]-[27] and early breast cancer detection [126]-[128], and TWMI applications [6], [7].

In the work illustrated in [J3], Time Domain Reflectometry (TDR) UWB through wall gap detection system based on the operation principle of the UWB imaging system proposed by Khor et al. [29] is introduced. It is based on sending a short duration pulse that is synthesized by transmitting continuous wave (CW) signals at equidistant frequencies covering the entire UWB range from 3.1 GHz to 10.6 GHz. The signal is produced by a vector network analyzer (VNA) after proper calibration over the pre-stated frequency range. The time domain representation of the pulse can be obtained by performing an Inverse Fast Fourier Transform (IFFT) on both transmitted and received signals. The principle is used in [29] for building a complete UWB imaging system for breast cancer

detection. Multiple numerical simulations have been carried out using CSTMWS, to address the possible multiple reflections due to the wall construction. These simulations are used to ensure the negligible effect of the higher order reflection on the gap detection accuracy.

The proposed UWB detection system has an advantage over some of the available systems since it adopts the monostatic radar principle, i.e. it uses just one antenna for both transmission and reception. The UWB sensor is also another critical design parameter regarding the cost, weight and size. In the proposed system the heavy metallic UWB horn sensor is replaced by a low profile UWB microstrip antenna maintain a high accuracy detection level.

6.2.1 Through Wall Gap Detection

The proposed UWB detection system for through wall gap detection is shown in Fig. 6.1 [J3]. The system includes a fixed support to mount a UWB probe antenna. The probe antenna is connected to channel (1) of the VNA. An absorber is mounted vertically behind the antenna to prevent any undesired back reflections. The antenna is centered to face the first wall in the y-z plane, whereas the separation distance between the antenna and the first wall should be chosen carefully to ensure working in the far-field region of the antenna. Undesired reflections in UWB imaging systems considered as a great obstacle. To overcome this problem we focus on a prototype which images the target using a synthesized pulse realized by sending continuous signals at equidistant frequencies over the required microwave band [29].

In order to check the imaging system capabilities for detecting hidden gaps behind walls, we made some practical tests using the setup shown in Fig. 6.1. The proper choice of the UWB antenna sensor is very critical issue for the system. The (UWB) antenna with circular radiator, presented in Section 4.3.1, can be used as antenna probe covering the frequency band from 3 to 10 GHz. This antenna prototype is chosen to work as a testing probe in this system because of satisfying impedance bandwidth of the UWB range, its relatively constant gain and stable radiation patterns over the UWB frequency range.

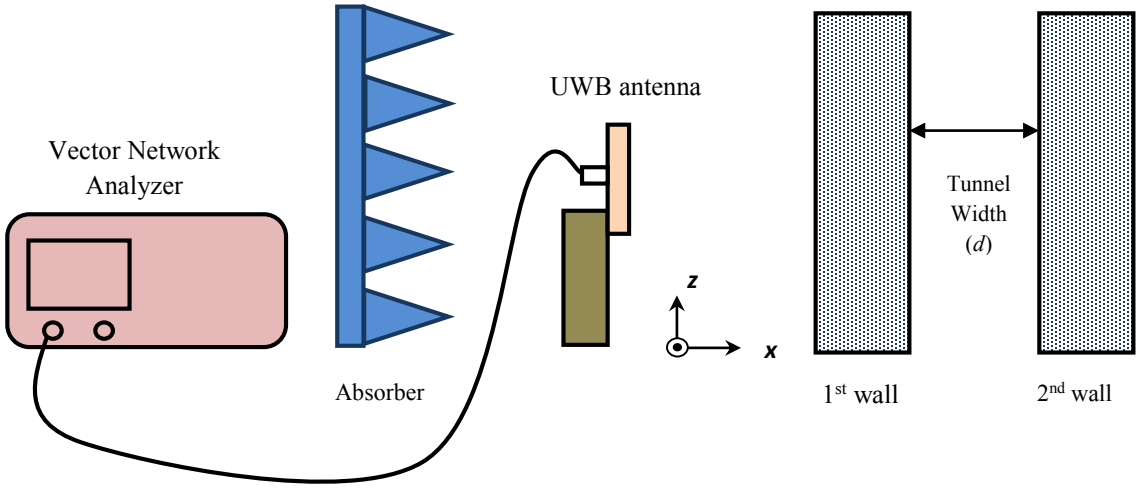

Figure 6.1 The proposed UWB imaging system for through wall gap detection.

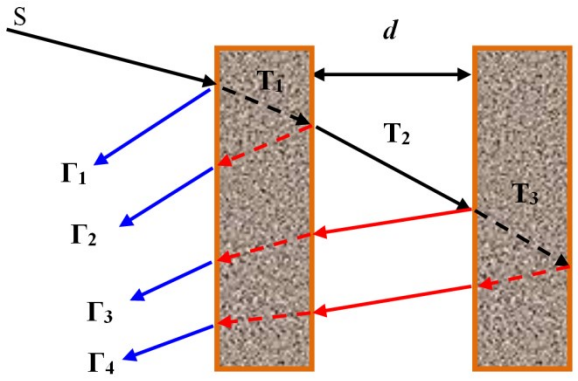

Figure 6.2 Reflections from the 1st and the 2nd wall with a gap in between.

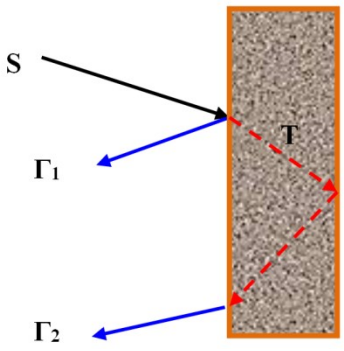

Figure 6.3 Reflections from a solid wall with no gaps.

Two different wall materials were studied. The first type with thickness = 3cm, length = 22cm, and width = 30cm is made of a reinforced paper with a lower attenuation coefficient (0.26 dB/cm) than the second one. The second material (5.5cm thickness, 23cm length, and 15cm width) is made of sandy brick and has a very high attenuation coefficient (3.6 dB / cm). Fig. 6.2 and 6.3 show different reflections from two walls separated by an air gap and from a solid wall, respectively. As shown in Fig. 6.2, we expect four reflection coefficients ($\boldsymbol{\Gamma_1, \ldots..., \Gamma_4}$) in case of having a gap between the two walls.

The gap detection algorithm begins by reading the reflection coefficient (S_{11}) from the VNA to obtain a frequency domain representation for the wall(s) reflections *G(f)*. Using Inverse Fast Fourier Transform (IFFT) embedded code in the VNA, a time domain representation of the reflection can be obtained *g(t)*. In order to cancel the antenna, cables and connectors effect, the received reflections *g(t)* subtracted from the antenna response in front of an absorber *a(t)*. The resulted signal *s(t)* contains only the reflection information from the wall(s) under study. By monitoring the peaks and their locations, the detection algorithm will provide enough information to make a decision in regard to the structure with either a solid wall or two walls separated by a gap (*d)*. The gap 'tunnel' width (*d*) separating the two walls can be evaluated using the separation time (Δt) between the second reflection $\boldsymbol{\Gamma_2}$ and the third reflection $\boldsymbol{\Gamma_3}$ from the following equation:

$$d = (\Delta t \cdot c)/2 \tag{6.1}$$

where *c* is the speed of light in free space. The flow chart of the gap detection algorithm is shown in Fig. 6.4.

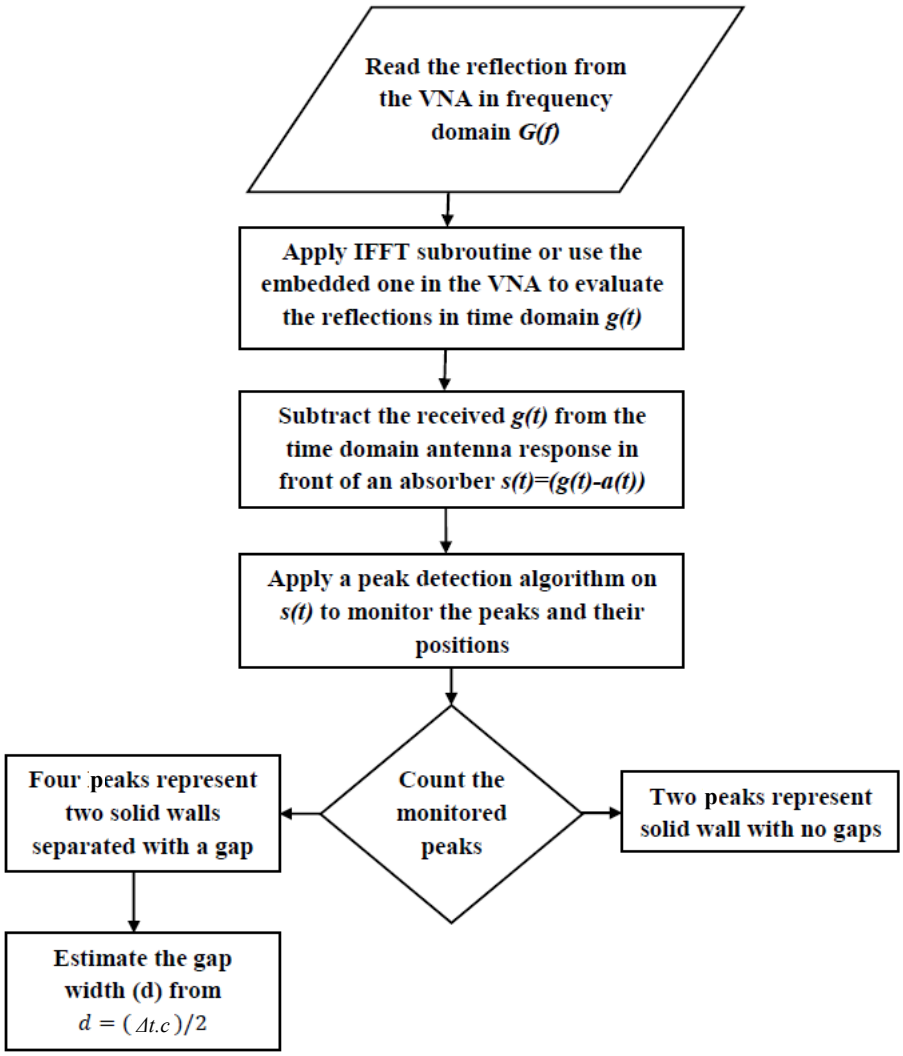

Figure 6.4 Gap detection algorithm.

6.2.1.1 Numerical Investigation of Through Wall Gap Detection Using CSTMWS

In order to verify the proposed system performance and study the possible sources of errors, especially from higher order reflections, some numerical simulations have been carried out using CSTMWS simulator.

Two different cases have been investigated to determine the expected time domain reflections. The first one is the single wall, while the second is two walls separated by an air gap (d). An UWB plane wave Gaussian pulse (3 to 10 GHz), shown in Fig. 6.5, is used as a source of an incident wave, while the reflected back signals are monitored on the surface of the first wall. Two different scenarios for the internal construction of the walls under study are assumed. The first is for a lossless case with zero conductivity as an extreme case with no attenuation. While the other one assumes an actual sandy brick walls with finite conductivity (ε_r=5.84 and the conductivity is σ=89 mS/m). Fig. 6.6 shows a comparison between the time domain reflection from single wall and the reflections of two walls separated by an air gap of 5 cm assuming the worst case of lossless walls with zero conductivity. It can be concluded that the first and second reflections for both cases are coincident with each other. However, the multiple reflections (i.e. higher order reflections inside the single wall) are responsible for the lower amplitude reflections around 2.3 ns (solid red curve). The amplitudes of these reflections are much smaller compared with $\boldsymbol{\Gamma_3}$. Fig.6.7 shows the reflections according to the second scenario of using sandy brick walls. The effect of the higher order reflections decreased dramatically that cannot interfere with $\boldsymbol{\Gamma_3}$. In the case of two walls reflections, the air gap separation (d) is responsible for the time difference between $\boldsymbol{\Gamma_2}$ and $\boldsymbol{\Gamma_3}$. Some parametrical studies for different values of (d), shown in Fig. 6.8, illustrate that effect.

6.2.1.2 Solid Wall with No Gaps Response

After constructing the system shown in Fig.6.1 and calibrating the VNA using standard calibration procedure in the frequency range of 3 GHz to 10 GHz, we measure the reflection

coefficient in frequency domain and then using the time domain conversion tool embedded in the VNA, we convert the response into the time domain. Fig. 6.9 shows the antenna response in front of an absorber and without any walls, where we can notice two large reflection peaks and some small reflections at a later time. The first peak accounts for the reflection from the interface between the microstrip feed line and the antenna, while the second peak results from reflection of the electromagnetic wave radiated by the antenna into free space. The minor reflections at later time can be attributed to multipath effects and scattering waves from the surrounding objects. Fig. 6.10 shows a comparison between the time domain antenna response in front of an absorber and the response in front of a single low attenuation wall, 19 cm apart, where two huge peaks appeared as a result of the air / wall reflection (Γ_1) and wall / air reflection (Γ_2). Fig. 6.11 (a, b) shows a photo of the measurement setup.

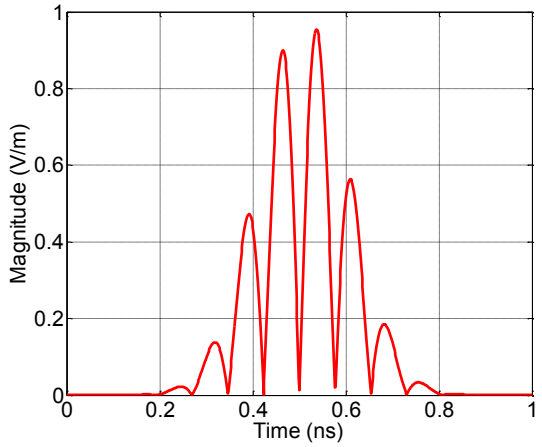

Figure 6.5 UWB plane wave pulse used by CSTMWS.

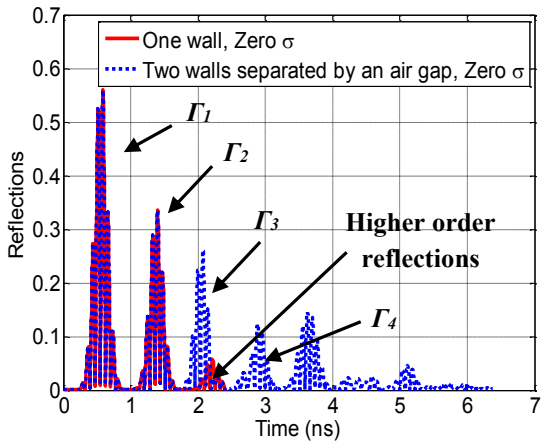

Figure 6.6 Time domain reflection comparison using no attenuation walls.

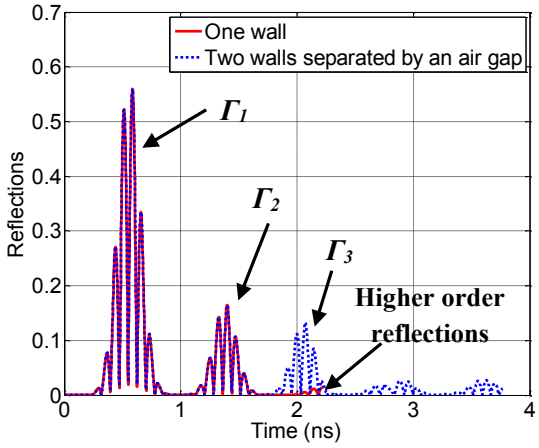

Figure 6.7 Time domain reflection comparison using sandy brick walls.

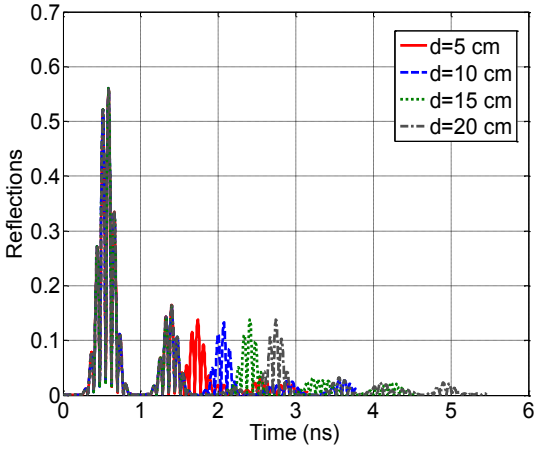

Figure 6.8 Time domain reflections of two walls for different values of the air gap (*d*).

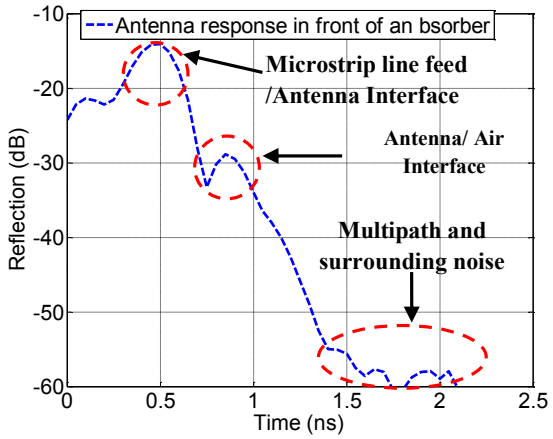

Figure 6.9 Antenna response in front of an absorber.

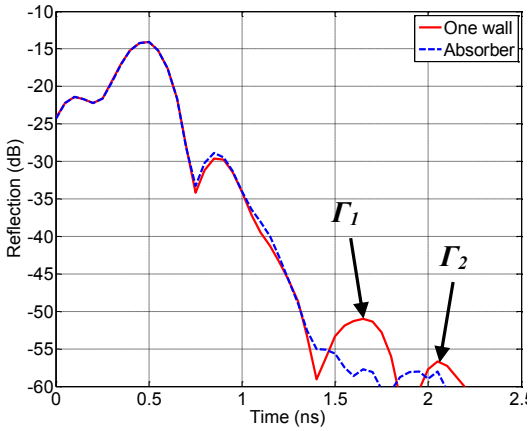

Figure 6.10 Reflections from a solid low attenuation wall without gaps.

(a) (b)

Figure 6.11 Practical measurement arrangements (a) solid sandy brick wall (b) two walls separated by a distance (*d*).

6.2.1.3 Two Low Attenuation Walls Separated by an Air Gap (d) Response

Fig. 6.12 (a-e) shows the multiple reflections due to two walls separated by a distance (d). Table 6.1 shows a comparison between the actual gap dimensions and the calculated ones using (6.1). There is a good agreement between the actual and the calculated separation d, where the percentage error does not exceed 6.25% for the considered cases. The error pattern here does not follow a certain pattern because of errors in antenna location adjustment, minor errors in actual distance measurements and some errors due to multipath effect from the surrounding objects.

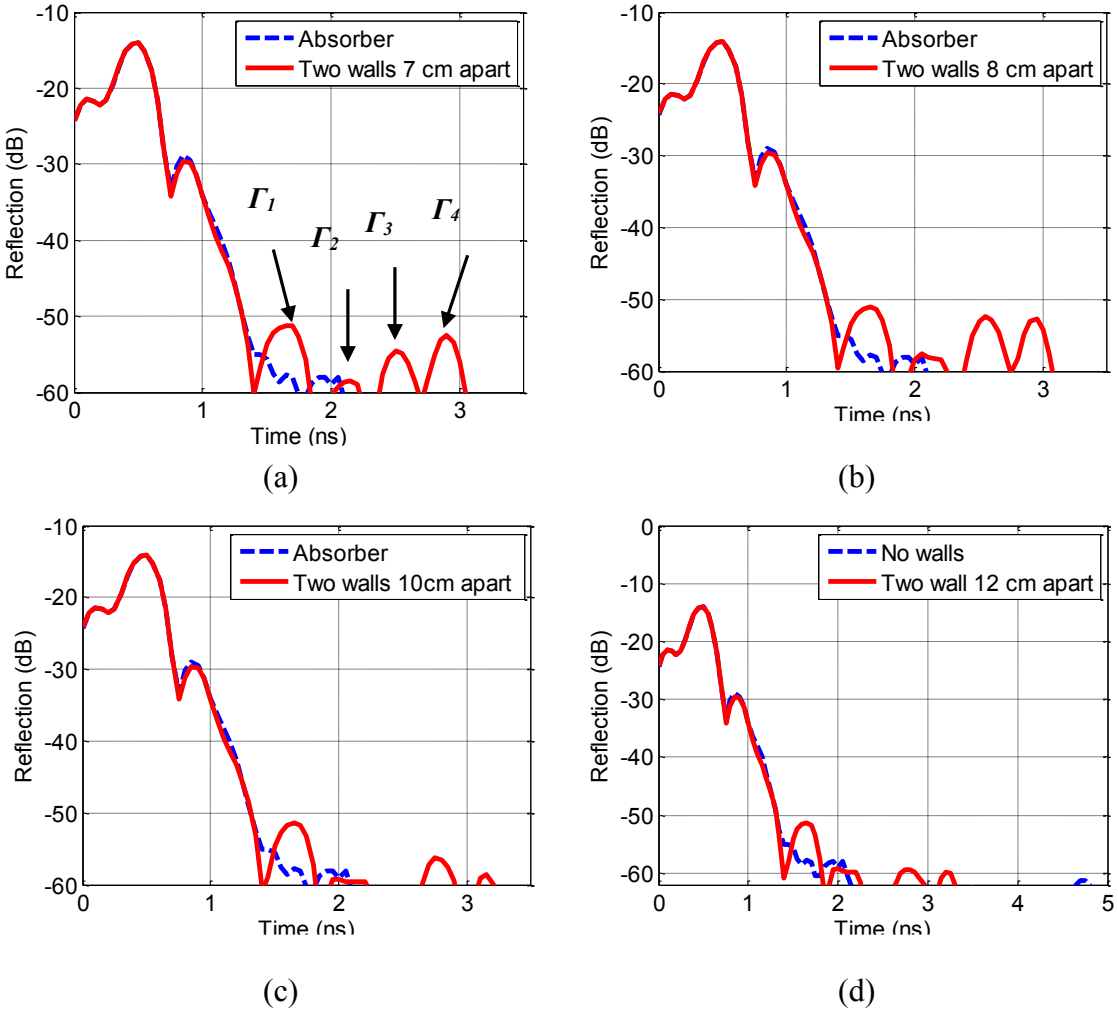

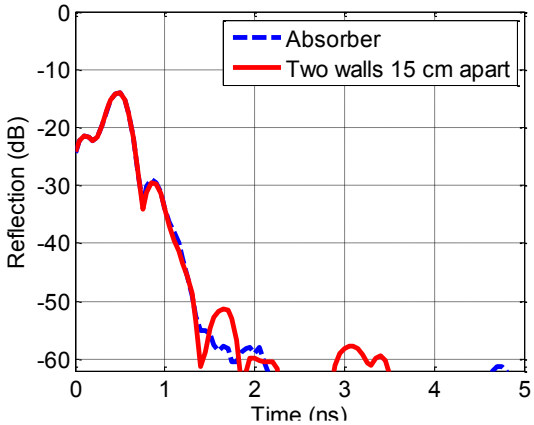

(e)

Figure 6.12 Reflections from two low attenuation walls separated by an air gap (*d*), (a) *d*=7 cm, (b) *d*=8 cm, (c) *d*=10 cm, (d) *d*=12 cm, (e) *d*=15 cm.

Table 6.1 Comparison between Actual and calculated gap length between walls.

Actual Distance between two walls	Calculated Distance between two walls	Error%
7 cm	6.75 cm	3.5%
8 cm	7.5 cm	6.25%
10 cm	9.75 cm	2.5%
12 cm	11.25 cm	6.25%
15 cm	15 cm	0%

6.2.1.4 Two High Attenuation Walls Separated by an Air Gap (d) Response

The nature of the wall material has a great effect on the reflected back signals from the walls, for example, using high attenuation walls (sandy bricks) will result in much lower reflection levels (Γ_2, Γ_3, Γ_4) after the first reflection. Time domain representation is shown in Fig. 6.13 for the reflections occur from a solid wall in front of the transreceiving antenna. The distance from the antenna probe to the first wall is reduced to 10 cm for reducing the round trip path loss. Two major peaks can be noticed; the first one is due to the air / wall reflection and the second is due to the wall / air reflection whose magnitude is very low (less than -60 dB) mainly due to the wave high attenuation inside the wall. Fig. 6.14

illustrates the effect of 5.5 cm gap between the two walls, where just three reflections (Γ_1, Γ_2, Γ_3) can be detected while the fourth one (Γ_4) cannot be detected because of the interference with the noise floor due to its small value. The calculated distance between the two walls is 5.25 cm which compared to the actual distance (5.5 cm) with a percentage error of 4.54%.

6.2.2 UWB TWMI Hidden Targets Detection System

Recently, as a new trend, EM based systems can be used in through wall microwave imaging (TWMI) applications to help in detecting the existence of any hidden rooms or hidden people behind walls [6], [7]. The proposed BAVA antenna array system, presented in Section 4.3.4.3-Chapter 4, is integrated into Time Domain Reflectometry (TDR) UWB TWMI detection system.

The proposed UWB TWMI system for hidden target detection is shown in Fig. 6.15. The system includes a 3D movable Lynxmotion robotic arm (AL5D) [129] to provide the required scanning motion for the proposed antenna array system. The input port of the array system is connected to channel (1) of the VNA. An absorber is mounted vertically behind the antenna system to prevent any undesired back reflections. The antenna system is centered to face the first wall in the y-z plane, whereas the separation distance between the antenna and the first wall should be chosen carefully to ensure working in the far-field region of the antenna (*35 cm*). Undesired reflections in UWB imaging systems considered as a great obstacle. To overcome this problem we focus on a prototype which images the target using a synthesized pulse realized by sending continuous signals at equidistant frequencies over the required microwave band.

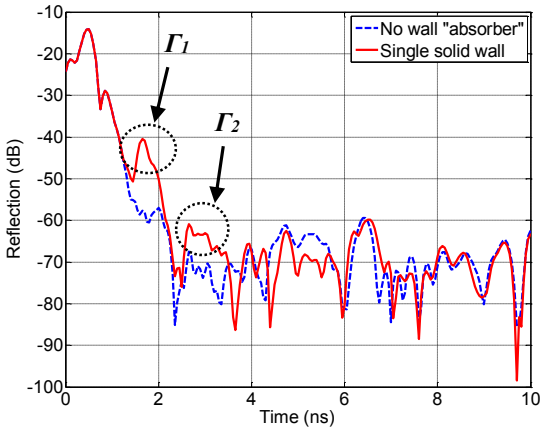

Figure 6.13 Reflections from a solid single high attenuation wall without gaps.

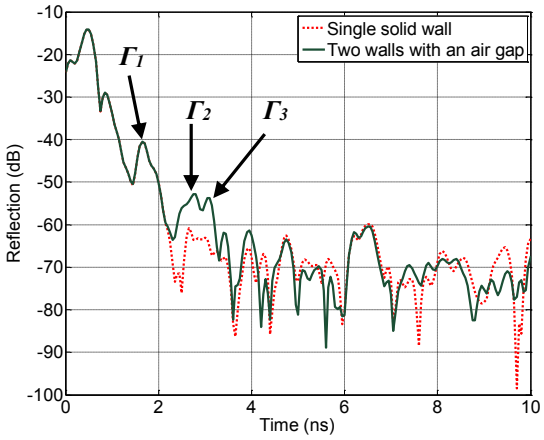

Figure 6.14 Reflections from two high attenuation walls separated by an air gap of 5.5 cm.

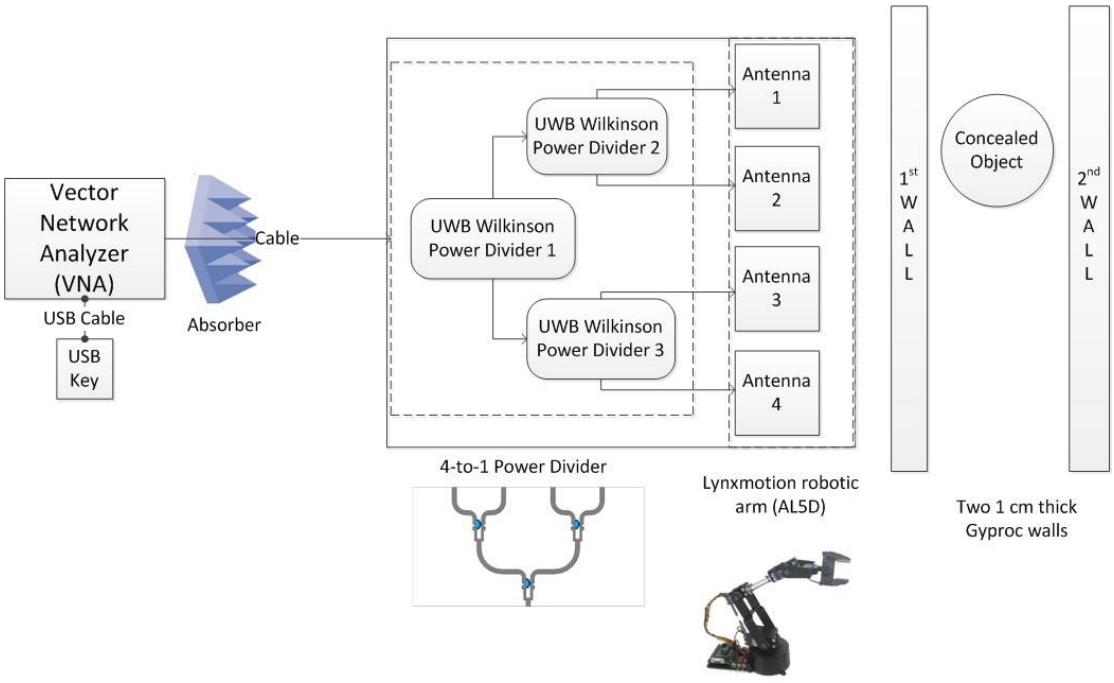

Figure 6.15 The UWB through wall detection system.

The target to be scanned consists of two 20 x 20 cm Gyprock plasterboard walls with thickness of 1 cm and separated by an air gap of 15cm. As shown in Fig. 6.16, the scanning area is divided into 100 squares with equal length and width of 2 cm. The hidden

target to be detected is chosen to be a metallic ball of diameter 4 cm mounted behind the square # 57. A photo of the proposed antenna system mounted on the robotic arm is shown in Fig. 6.17.

6.2.2.1 Hidden Target Detection Algorithm

The concealed target detection algorithm begins by reading the reflection coefficient (S_{11}) from the calibrated VNA. The reading process is carried out each point in the area under investigation. The obtained data is considered as a frequency domain representation for the walls and the target reflections *G(f)*. Using Inverse Fast Fourier Transform (IFFT) embedded code in the VNA, a time domain representation of the reflection coefficient can be obtained at each point *g(t)*. In order to cancel the antenna system (feeding network and the antenna array), cables and connectors effects and to reduce the clutter signals from unwanted objects, the received reflection *g(t)* are subtracted from the antenna system response in front of an absorber *a(t)*. The resulted signal *s(t)* contains only the reflection information from the walls and the hidden target under study. By multiplying *s(t)* by low shape factor Kaiser window *k(t)* focused in the region between the two walls, only the target information can be extracted *m(t)*. Image reconstruction can be done by correlating the 2D data of the points locations to the area under the *m(t)* curve (integration of *m(t)*). The flow chart of the hidden target detection algorithm is shown in Fig. 6.18.

6.2.2.2 Experimental Results of the Concealed Target Detection

After constructing the system shown in Fig.6.15 and calibrating the VNA using standard calibration procedure over the frequency range of 3 GHz to 10 GHz, the reflection coefficient in frequency domain is measured.

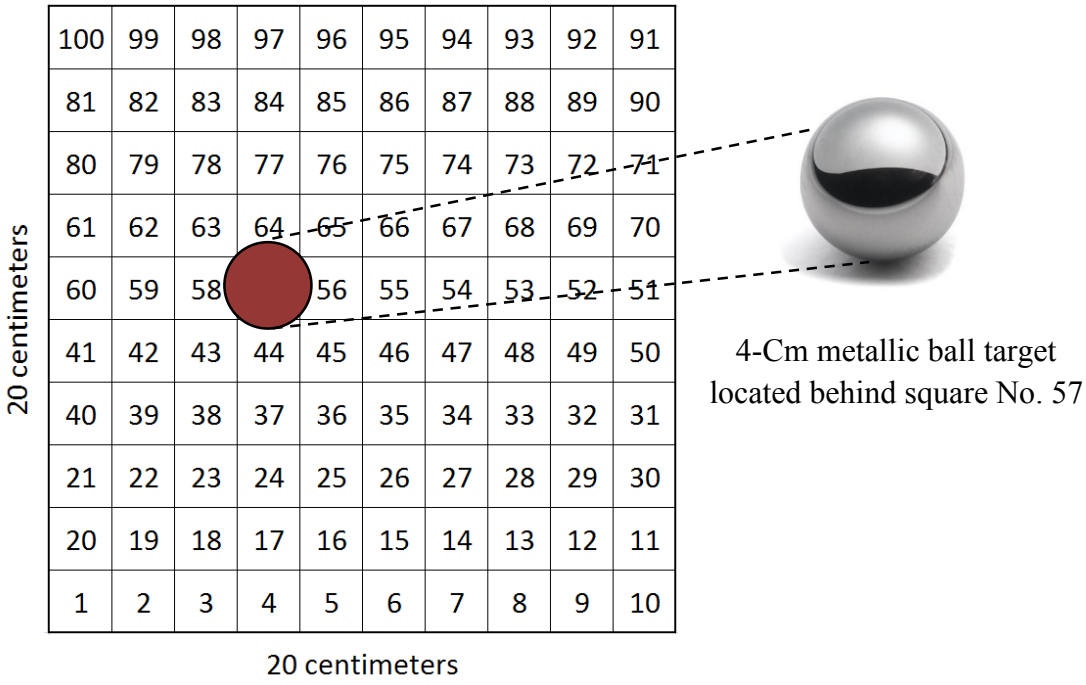

Figure 6.16 The wall area to be scanned and the target location.

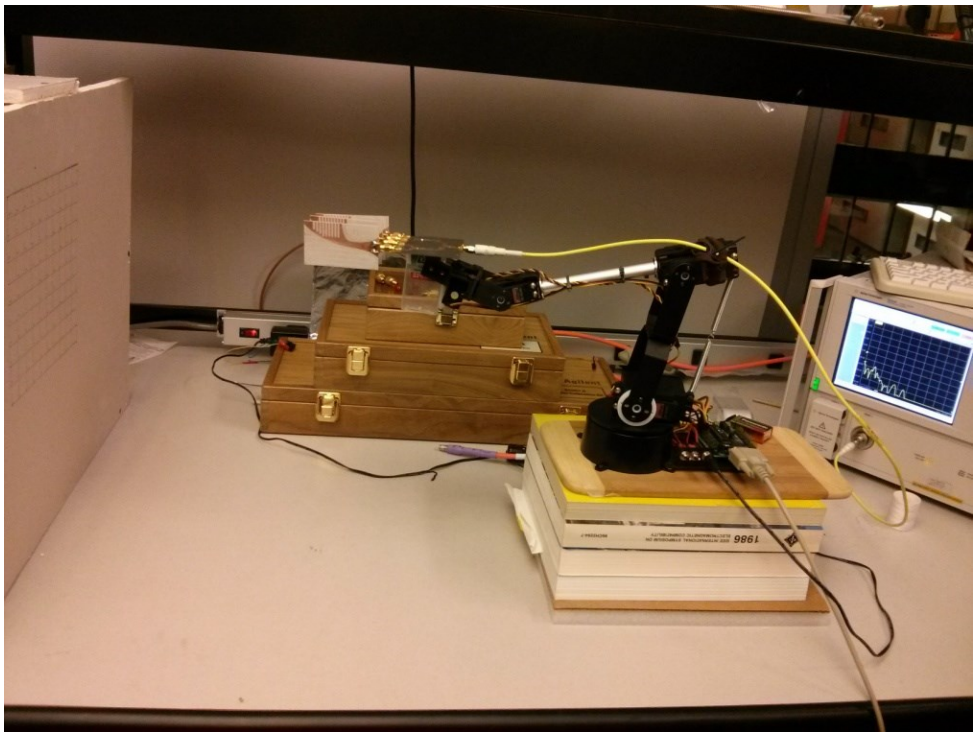

Figure 6.17 The proposed antenna system mounted on the robotic arm (AL5D).

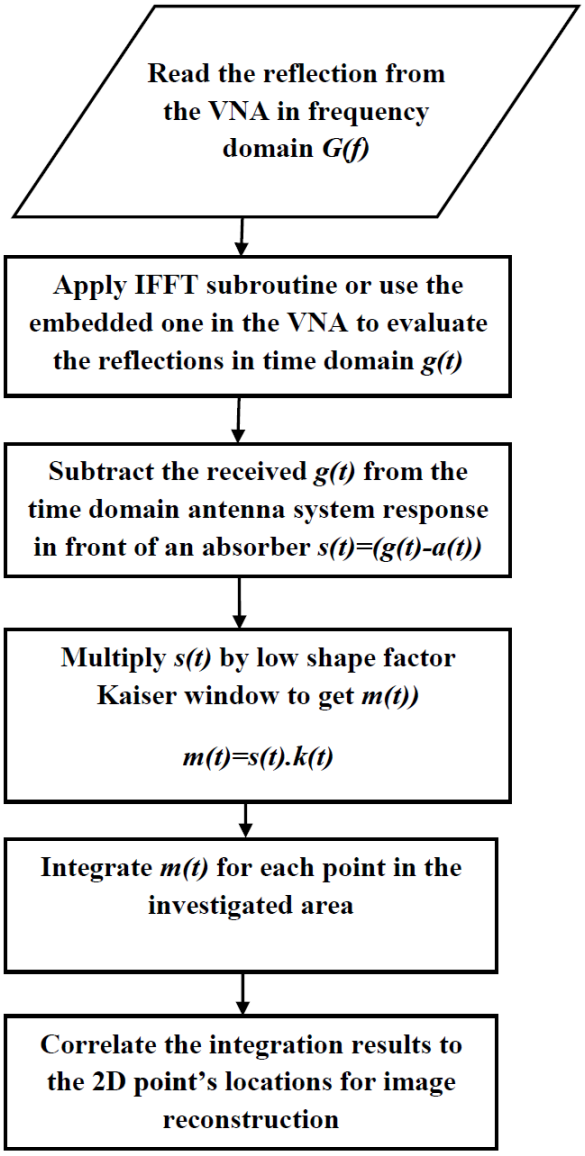

Figure 6.18 Hidden target detection algorithm.

The measured results are then converted into time domain using the time domain conversion tool embedded in the VNA. Fig. 6.19 shows a comparison between the antenna system response in front of an absorber and the response in front of the two walls with a 4 cm diameter metallic ball in between. It can be noticed multiple peaks between 0 ns till 3 ns which are related to the internal reflections in the antenna system components (i.e. between

the antenna elements and the feeding network besides the cable and the input port). Three major peaks can be detected at 3.7 ns, 4.2 ns and 4.9 ns. The first and the third peaks account for the reflection from the first and the second wall, while the middle peak results from reflection from the hidden ball in the gap between the walls. The minor reflections at later time can be accounted to multipath effects and scattering waves from the surrounding objects. Fig. 6.20 shows a comparison between the time domain antenna response in front of the two walls with and without the hidden metallic object. The measurement process should be repeated for each point in the investigated area. An interpolating program is used to plot a 2D image for the target with and without the presence of the metallic target. These images are shown in Figs. 6.21 and 6.22, respectively. In order to enhance the reconstructed image resolution, the received data are processed using Gaussian filter [130] to remove the signal echoes resulted from the wide beam of the antenna system. Fig. 6.23 illustrates an improved reconstructed image after the filtration process.

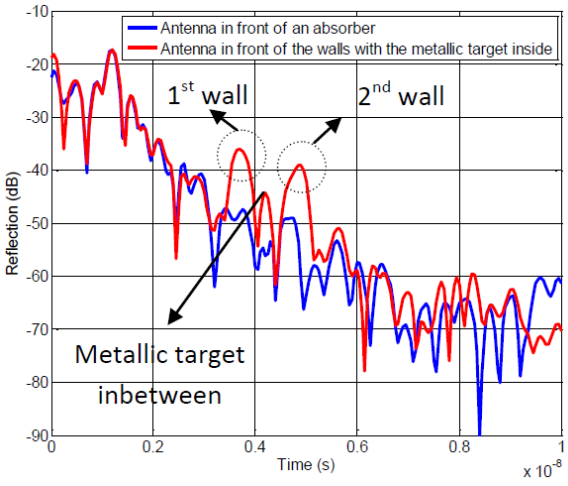

Figure 6.19 Comparison between the antenna system response in front of an absorber and the response in front of the two walls.

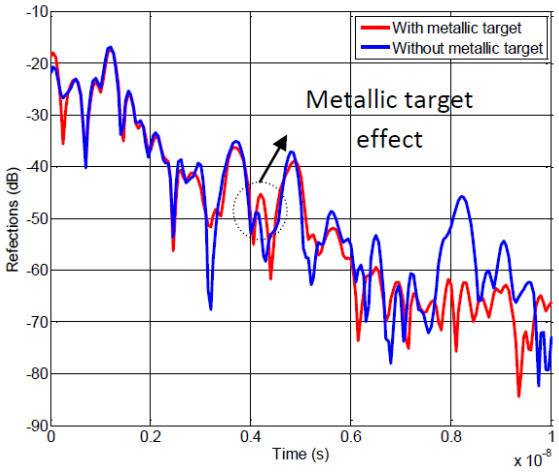

Figure 6.20 Comparison between the time domain antenna response in front of the two walls with and without the hidden metallic object.

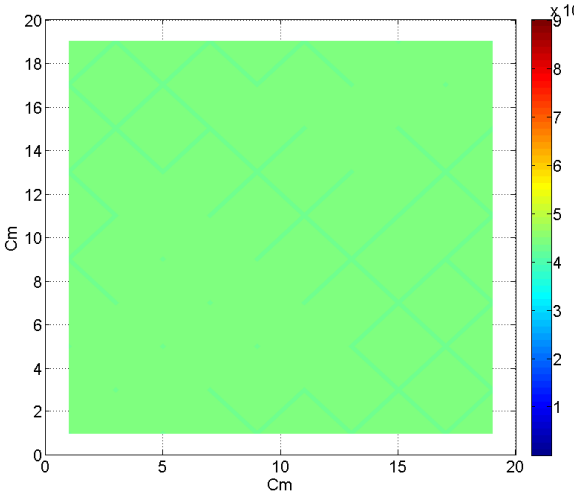

Figure 6.21 2D image for the target without the metallic ball.

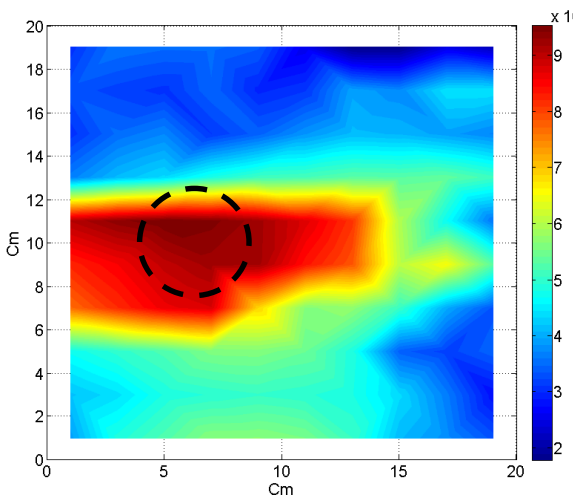

Figure 6.22 2D image for the target with the metallic ball.

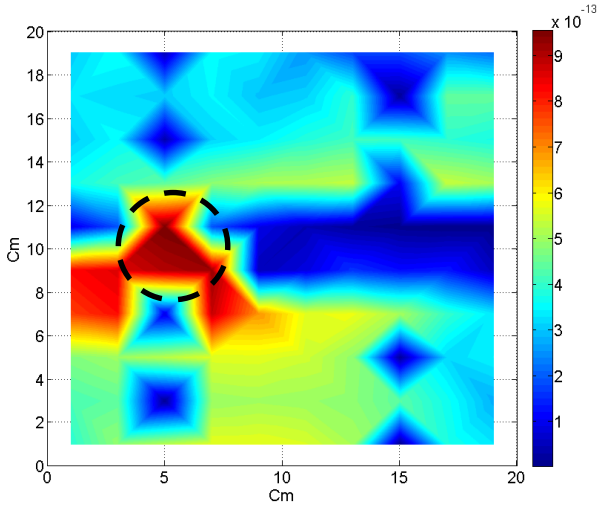

Figure 6.23 2D image for the target with the metallic ball after filtration.

6.3 MMW Imaging / Detection

In this section, an active monostatic MMW imaging system for hidden weapons detection will be presented. The system uses a short pulse in the MMW range of frequency around 30 GHz produced by a vector network analyzer (VNA) after proper calibration over the operating frequency range for target scanning. The time domain representation of the pulse can be obtained by performing Inverse Fast Fourier Transform (IFFT) on both transmitted and received signals (the reflected back signal from the target).

6.3.1 Monostatic Imaging / Detection System Configuration

The proposed MMW imaging system for hidden weapons detection is shown in Fig. 6.24. The system, presented in [C5], consists of a fixed support to mount the MMW antenna on it (instead of the PC controlled robotic arm, as shown in Fig. 6.24). This probe antenna is connected to channel (1) of the VNA. An absorber is mounted vertically behind the antenna to prevent any undesired back reflections. The antenna is centred to face the centre of the phantom in y-z plane. The separation distance between the antenna and the phantom should be chosen carefully to ensure working in the farfield region.

In order to simulate the human body, a small target is built using three different layers the first one is made of jeans with a thickness of 0.6 mm followed by a 1mm layer of natural animal leather and finally a supporting layer of reinforced paper with 2 mm thick. The target has a triangular shape with equal edges of 10 cm. Fig. 6.25 shows the construction of the target to be imaged.

6.3.1.2 System Operation and Primary Results Using a Standard Horn Antenna

To check the imaging system capabilities for detecting hidden weapons under clothes, we made initial tests using the setup shown in Fig. 6.24. A standard MMW pyramidal horn antenna (ARRA 23-862) with an operating bandwidth ranged from 26-32 GHz is used as a scanning element in the system. Fig. 6.26 shows the measured reflection coefficient of the horn antenna.

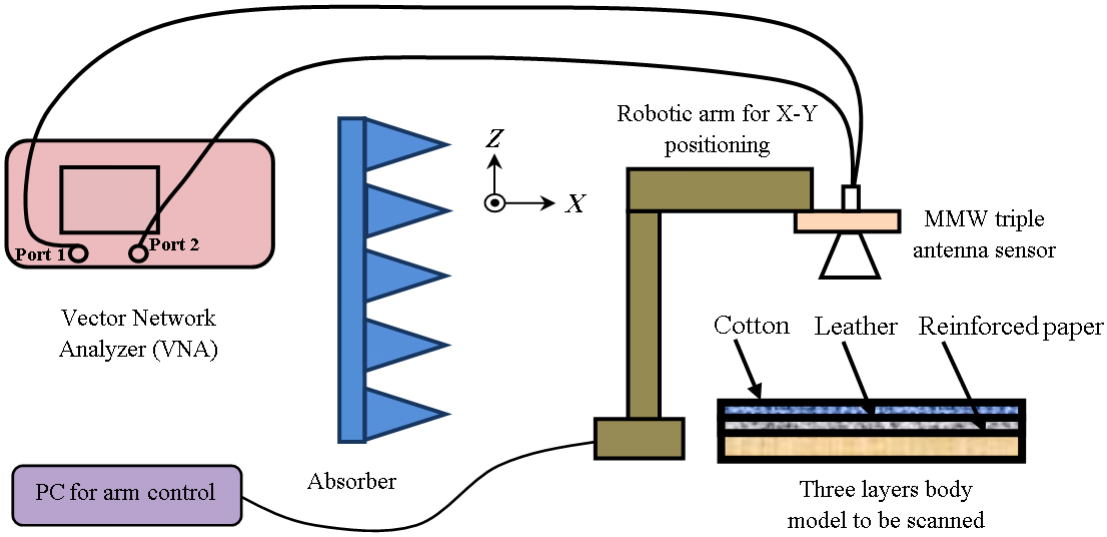

Figure 6.24 The proposed monostatic MMW imaging / detection system.

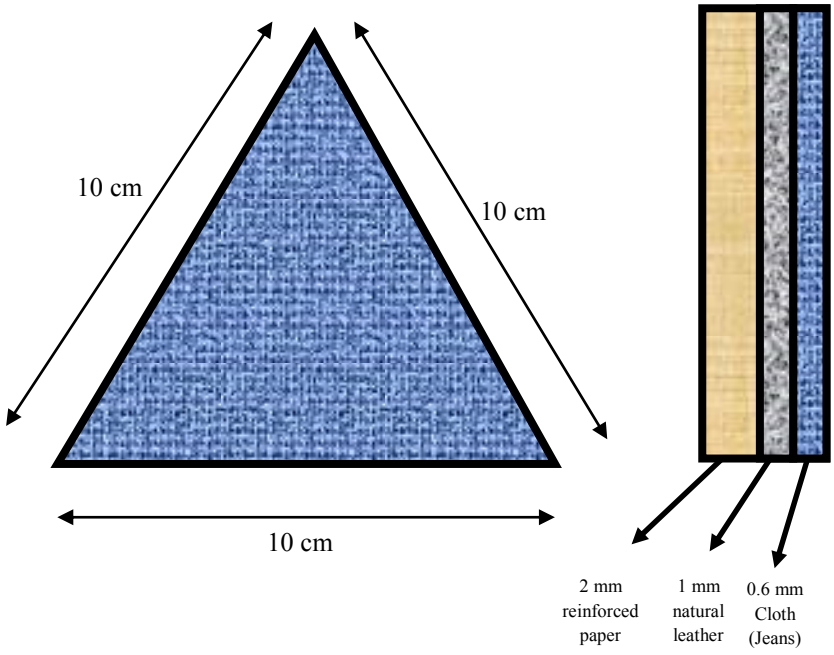

Figure 6.25 Target to be scanned.

To start the imaging process, the VNA is calibrated first using the standard calibrating kit (short, open and broadband load) over the range from 30 to32 GHz before

attaching the standard horn. Fig. 6.27 shows the time domain response of the horn antenna in front of an absorber. Two main peaks can be monitored at 0.2 and 0.7 ns. The first peak is due to the reflection of the transition from coaxial feeding to the rectangular waveguide, while the second one is due to the transition from the rectangular waveguide to the pyramidal horn.

The target to be imaged is illuminated in seven different points as shown in Fig. 6.28, where the scanning antenna is placed in front of each point recording the reflection coefficient in time domain for each point. The separation between the antenna and the target is kept constant at 10 cm to ensure working in farfield region.

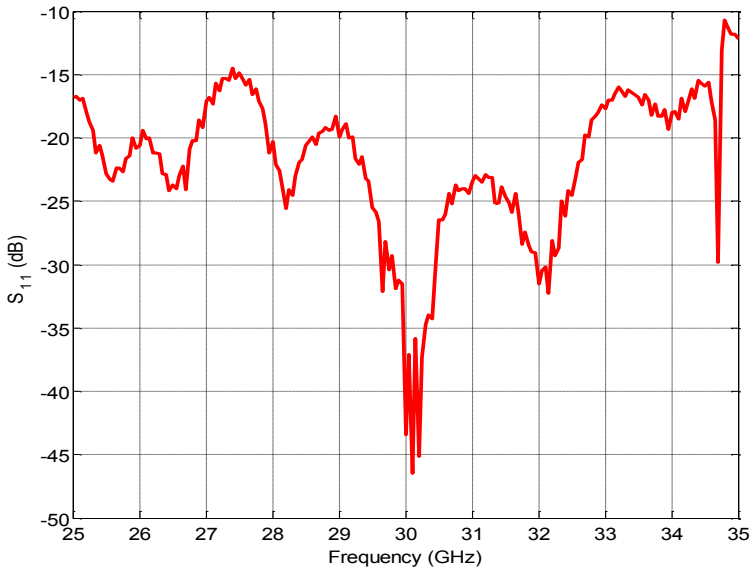

Figure 6.26 Reflection coefficient S_{11} of the standard horn antenna.

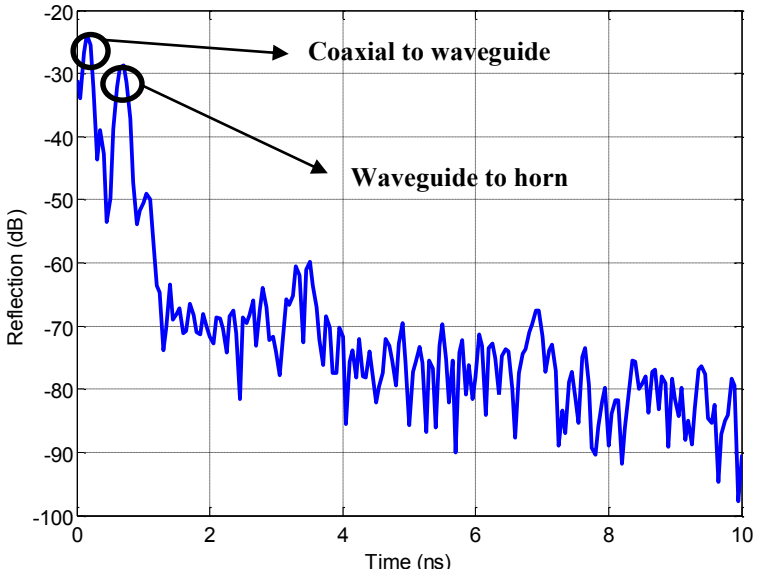

Figure 6.27 Reflection coefficient S_{11} of the standard horn antenna in front of an absorber in time domain.

Fig. 6.29 shows the effect of target presence in front of the scanning antenna, where it can be noticed a third peak due to target reflection. A metallic weapon is represented in this model by a 1 cent coin (8 mm diameter and 1 mm thick). This coin is hided under the jeans layer over the point number five. Fig. 6.30 shows the effect of the metallic coin presence. After recording all the reflection data for each point, an interpolating program is used to plot a 2D image for the target with and without the presence of the metallic coin. These images are shown in Fig. 6.31(a) and Fig. 6.31(b), respectively.

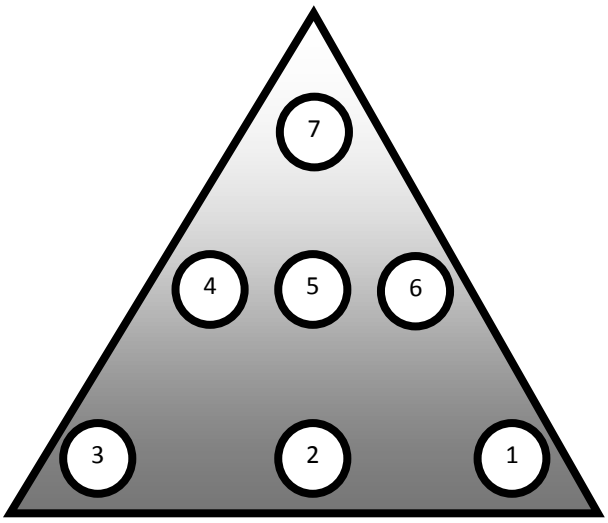

Figure 6.28 Target points.

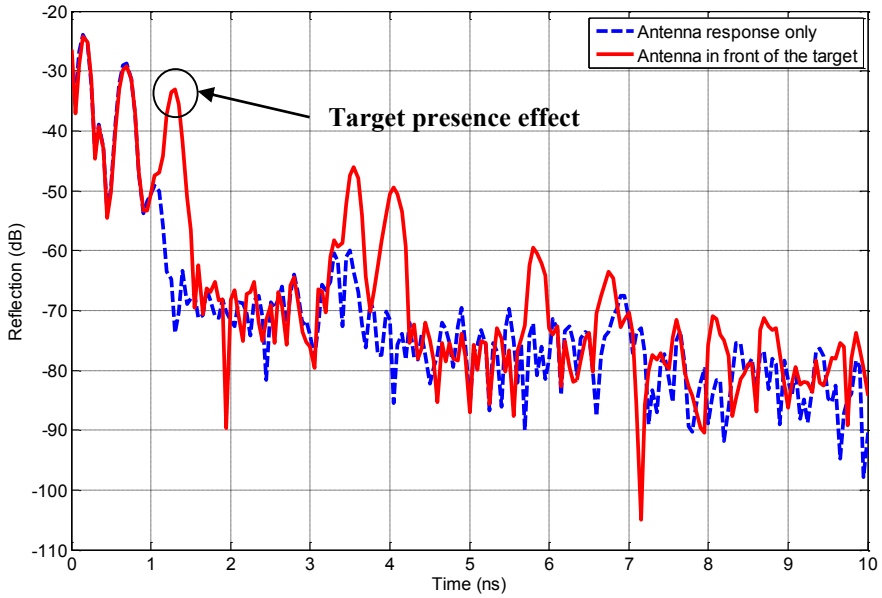

Figure 6.29 Antenna responses in front of an absorber vs. antenna in front of the target.

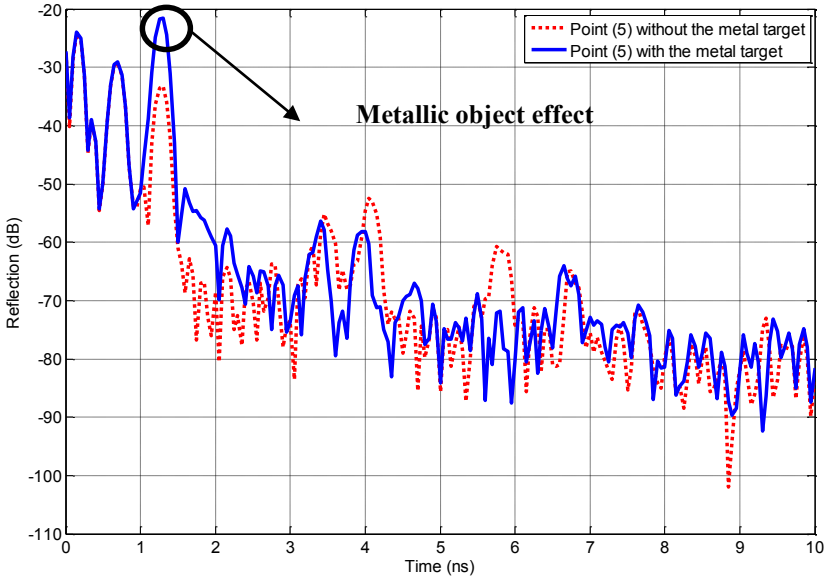

Figure 6.30 Metallic target effect on the antenna response.

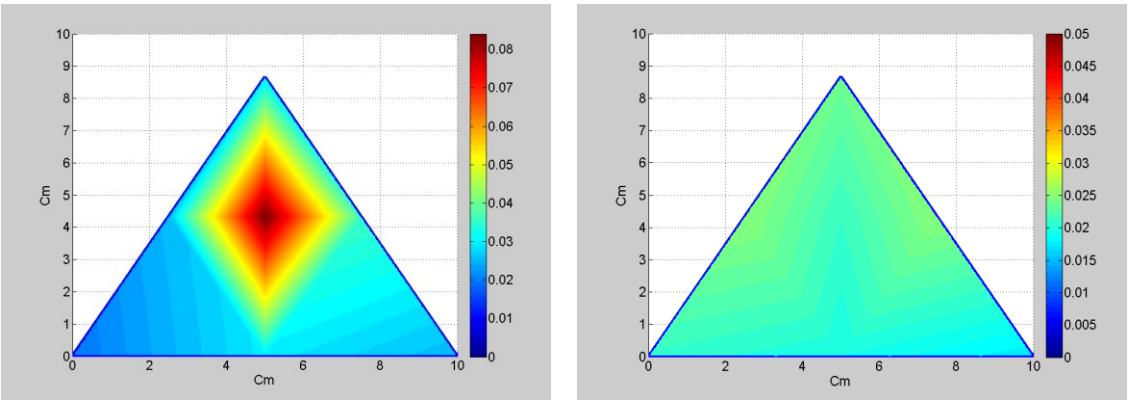

(a) (b)

Figure 6.31 2D image for the target using the standard horn probe (a) with the metallic object (b) without the metallic object.

6.3.1.3 Imaging Results Using a Hybrid Microstrip / Horn Antenna

To determine the effect of this sensor on the imaging system, the metallic horn antenna in the original setup, shown in Fig. 6.24, is replaced by the hybrid microstrip / horn antenna, discussed in chapter 5 section 5.4.4, then repeating the calibration procedure for the VNA

over the range (28 GHz to 32 GHz). The same coin target is placed at 30 cm from this antenna. Fig. 6.32 shows the time domain response of the horn antenna in front of an absorber.

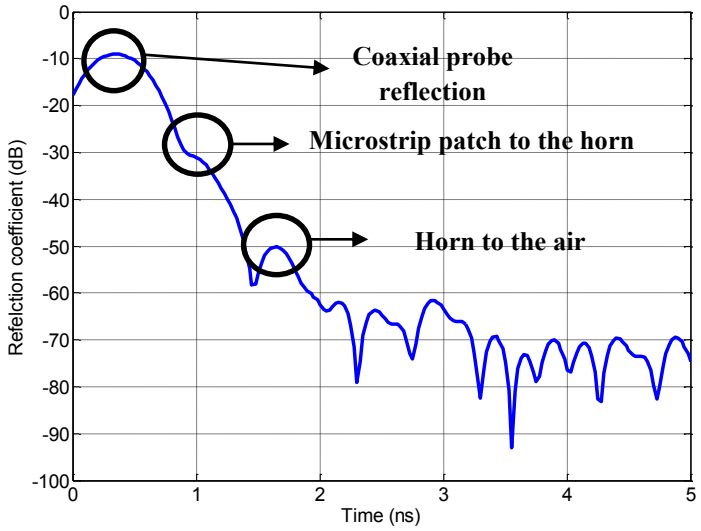

Figure 6.32 Reflection coefficient S_{11} of the standard horn antenna in front of an absorber in time domain.

Three main peaks can be monitored at 0.4 ns, 1 ns and 1.7 ns. The first peak is due to the reflection of the coaxial feeding of the connector, the second one is due to the transition from the patch antenna to the surface mounted horn and the third one is due to the horn to air interface. Fig. 6.33 shows the effect of metallic coin presence on the reflection coefficient of the scanning probe, where it can be noticed a fourth peak due to target reflection around 2.5 ns. The metallic object causes an increment in the reflection peak of 3.8 dB, which is smaller than the reflection obtained by using the standard horn. The difference in the reflection levels can be accounted to the higher directivity of the

standard horn. A 2D image is then generated by interpolating the successive measurements at different locations as shown in Fig. 6.34.

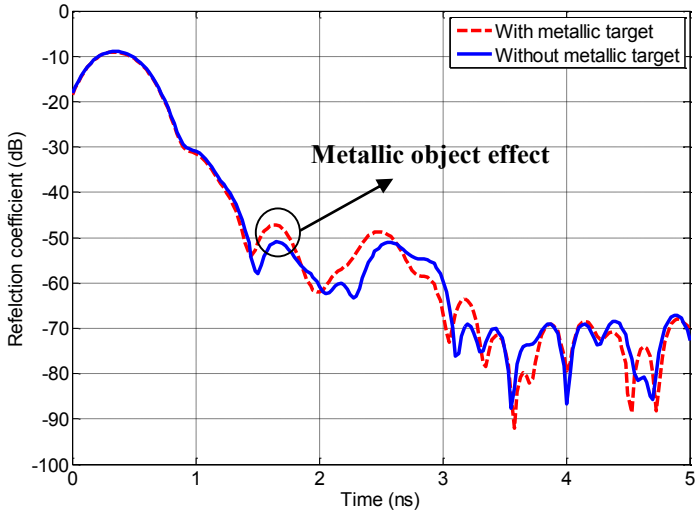

Figure 6.33 The effect of target presence in front of the scanning antenna, where it can be noticed a third peak due to target reflection.

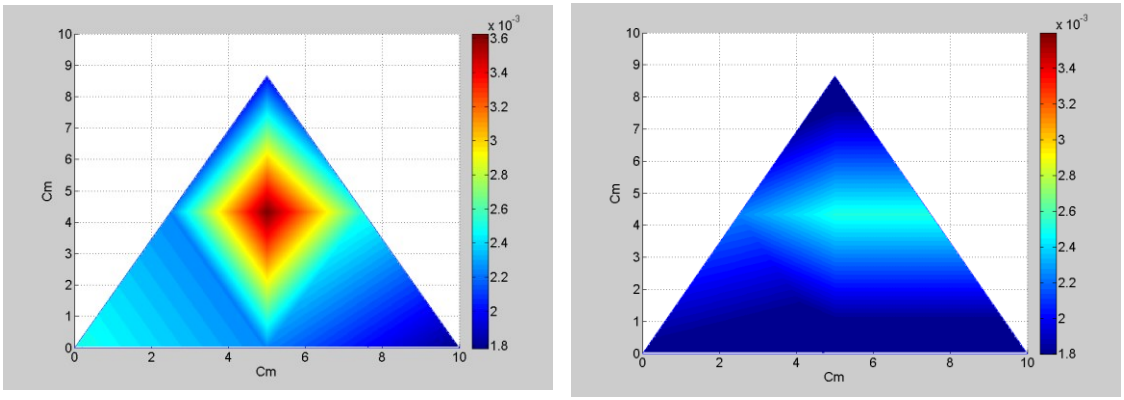

Figure 6.34 2D image for the target using the hybrid microstrip / horn probe (a) with the metallic object (b) without the metallic object.

6.3.2 MMW Sensor for Hidden Targets Detection Based on Reflection / Scattering Approach

The MMW sensor, presented in [J4], consists of three adjacent high gain microstrip / horn hybrid antenna elements. The central antenna acts as bi-static radar, while the two side antennas are used to receive the scattered back signals from a hidden object. The proposed design exhibits a remarkable small size (45 mm x 20 mm x 9.29 mm) compared with other commercially available antenna sensors including dish antennas, metallic horn and lens antennas. In addition, it is based on printed circuit board (PCB) technology, which leads to a lighter overall sensor weight and lower cost compared with other antenna sensors. Also, it provides remarkable enhancement for the detection ability and the reconstructed image resolution of a hidden target.

The presented antenna sensor consists of three adjacent antenna elements separated by 1.5 λ at 30 GHz. The distance between the antenna elements are chosen to minimize the undesired mutual coupling between them. The antenna elements integrated in this sensor are based on the hybrid antenna design presented in [J2].

6.3.2.1 Triple Element Antenna Sensor

As shown in Fig. 6.35, the proposed triple antenna sensor consists of three adjacent hybrid antenna elements with three separated input ports. The design parameters of these antenna elements are identical to the dimensions presented in [J2]. The separation distance between the antenna elements is chosen to be 1.5 λ at 30 GHz in order to minimize the mutual coupling between them without increasing the overall size of the triple sensor. The reflection coefficient and the mutual coupling between the antenna elements are illustrated in Fig. 6.36. There is a frequency shift of about 0.5 GHz between the experimental and the

CSTMWS simulated reflection coefficient (S_{11}) which can be accounted for some fabrication errors especially in the soldering process and alignment of mounted horns. It can be noticed that the measured mutual coupling does not exceed -27 dB over the range from 30 GHz to 32 GHz, while the measured impedance bandwidth of the antenna element ranged from 30.2 GHz to 33.6 GHz. The proposed triple antenna sensor exhibits remarkable radiation characteristics where it has broad side directive patterns in both E-plane and H-plane with good radiation pattern stability and high average realized gain of 10.5 dB over the operating band. There is a good agreement between the CST and HFSS simulated results, and the corresponding measured E-plane (XZ) and H-plane (YZ) radiation patterns at 31 GHz. The radiation characteristics of the middle antenna in the triple sensor, taken when the other side antenna ports are terminated with matched loads, are shown in Fig. 6.37.

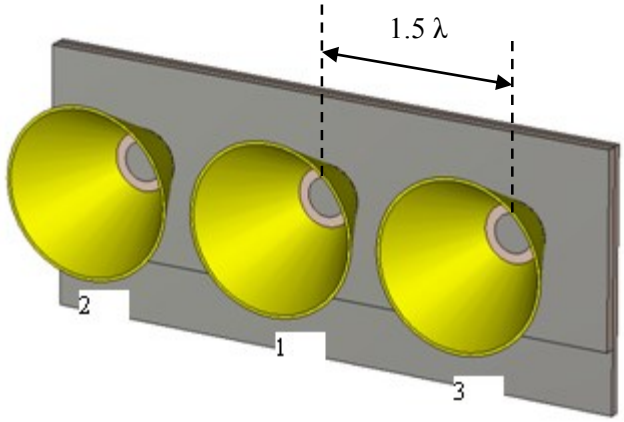

Figure 6.35 Geometry of the proposed triple antenna sensor.

6.3.2.2 MMW Imaging / Detection System Setup

The proposed automated MMW imaging / detection system setup for hidden weapons detection is shown in Fig. 6.24. The system includes a 3D movable Lynxmotion robotic

arm (AL5D) [127] to provide the required scanning motion for the proposed triple-antenna sensor. The middle antenna element input port of the sensor is connected to channel (1) of Agilent PNA-E8364B VNA, while channel (2) is connected to the side antenna elements alternatively to record both the scattered signals S_{21} and S_{31}. The VNA is used to generate a synthesized pulse after full two port calibration procedure over the band from 30 GHz to 32 GHz. An absorber is mounted vertically behind the mounted antenna sensor to prevent any undesired back reflections. The proposed sensor is centered to face the three layer body model in the x-y plane, whereas the separation distance between the antenna sensor and the first wall 10 cm is chosen carefully to ensure working in the far-field region of the antenna.

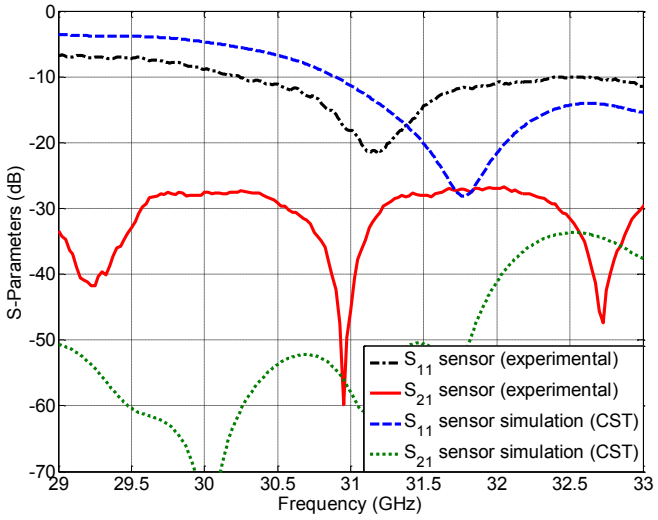

Figure 6.36 Reflection coefficient (S_{11}) and the mutual coupling (S_{21}) of the triple element sensor.

A photograph of the MMW imaging / detection setup and the triple antenna sensor is shown in Fig. 6.38. The body model to be scanned is built using three different layers; the first one is made of cotton with a thickness of 0.3 mm followed by a 1 mm layer of natural animal leather and finally a 2 mm thick supporting layer of reinforced paper. A

small area of 11×11 cm^2 of the body model is chosen as the scanning area, shown in Fig. 6.39, where it is divided into 111 square-shaped regions, each with area of 1×1 cm^2.

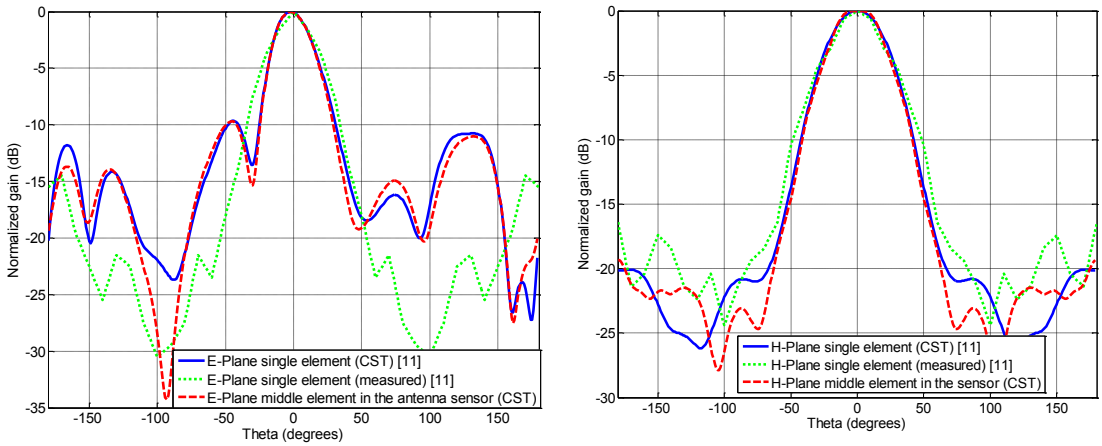

(a) (b)

Figure 6.37 The radiation pattern comparison between the stand alone antenna element and the antenna element within the proposed triple antenna sensor (a) E-plane (b) H-plane.

The robotic arm scanning motion, controlled by RIOS software [127], is adjusted to make the middle antenna of the sensor facing the center of each square, i.e. the X and Y resolution are chosen to be 1 cm. For demonstration purposes, a rectangular metallic strip made of copper with dimensions of 4 cm length, 1 cm width and 0.25 mm thickness is selected to be the hidden target. The metallic target is placed under the cotton layer with three different orientations. As shown in Fig. 6.39, the first orientation is vertical (red shaded rectangle), the second is inclined by 45 degrees (green shaded rectangle); while the third is horizontal (blue shaded rectangle).

6.3.2.3 Imaging / Detection Algorithm

The hidden target detection algorithm, illustrated in Fig. 6.40, starts by recording the frequency domain representation data for the reflected signal $G(f)$ from the hidden target and the body model as well as the scattering signals $S_{c1}(f)$and $S_{c2}(f)$received from the side antennas. Using Inverse Fast Fourier Transform (IFFT) embedded code in the VNA, a time domain representation of the reflection and scattering information can be obtained ($g(t)$, $s_{c1}(t)$ and $s_{c2}(t)$).

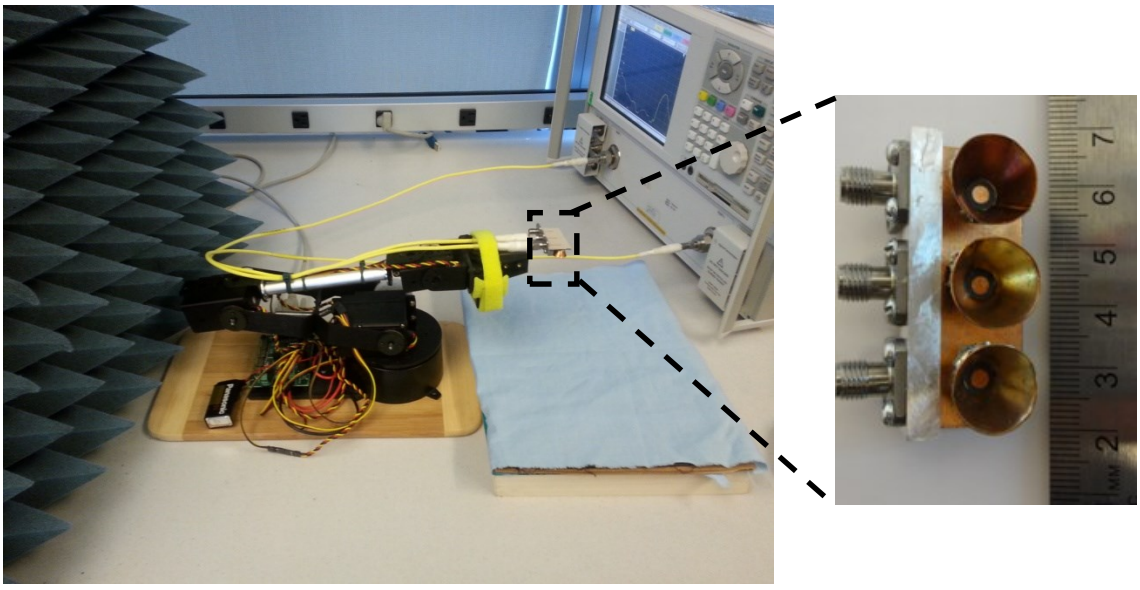

Figure 6.38 A photo of the MMW imaging / detection setup and the triple antenna sensor.

In order to cancel the effect of antenna elements, cables and connectors, the received signals are normalized by subtracting the sensor response in front of an absorber $a_r(t)$, $a_{sc1}(t)$ and $a_{sc2}(t)$, as follows:

$$g_n(t) = g(t) - a_r(t),$$

$$s_{c1n}(t) = s_{c1}(t) - a_{sc1}(t),$$

$$s_{c2n}(t) = s_{c2}(t) - a_{sc2}(t) \tag{6.1}$$

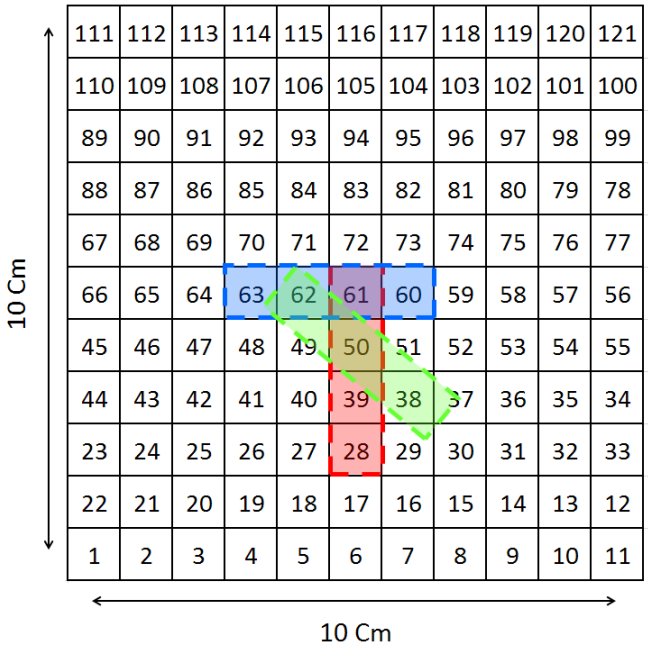

Figure 6.39 Scanning points over the body model and metallic target locations.

The resulted signals $g_n(t)$, $s_{c1n}(t)$ and $s_{c2n}(t)$ contain only the reflection and the scattering information from the body model and the target under study. Due to the path difference between the reflection and the scattering signals, time equalization process is needed for the scattering signals. To eliminate all the remaining unwanted reflections during the digital signal processing, the normalized signals are multiplied by a low shape factor Kaiser Window,

$$m_n(t) = g_n(t) * K(t - \tau)$$

$$m_{c1n}(t) = s_{c1n}(t - \Delta) * K(t - \tau)$$

$$m_{c2n}(t) = s_{c2n}(t - \Delta) * K(t - \tau) \tag{6.2}$$

where, Δ is a small delay time for path difference equalization of the scattered signals $m_{c1n}(t)$ and $m_{c2n}(t)$, and τ is the time shift required to center the Kaiser window at the required position, i.e. the first peak of the reflected / scattered signals, taken here to be 0.8 ns.

$$K(t-\tau) = \begin{cases} \dfrac{I_o\left(\pi\alpha\sqrt{1-\left(\dfrac{2(t-\tau)}{m}-1\right)^2}\right)}{I_o(\pi\alpha)} & ,0 \le t \le m \\ 0 & ,otherwise \end{cases} \tag{6.3}$$

where, I_o is the zeroth order of the modified Bessel function of the first kind, α is an arbitrary real number that controls the shape of the window (taken here to be 0.5) and m is an integer, and the length of the sequence is $T = m + 1$. Fig. 6.41 illustrates the Kaiser Window function for different values of α. Using a simple integration subroutine the area under each curve, which represents the reflection / scattering magnitude, can be estimated. Furthermore, the resulted signals are added together after multiplying them by some weights.

$$M_i = W_{1i} * m_n(t) + W_{2i} * m_{c1n}(t) + W_{3i} * m_{c2n}(t) \tag{6.4}$$

where i is the square no. in the scanning domain and $0<W_{ix}<1$ are the required adjustment weights.

The above algorithm steps are repeated for each scanned point within the scanned area. Finally, image reconstruction can be carried out after correlating the obtained results

to the 2D points' locations and interpolating them over the scanned area. The imaging / detection algorithm steps are implemented using Matlab code.

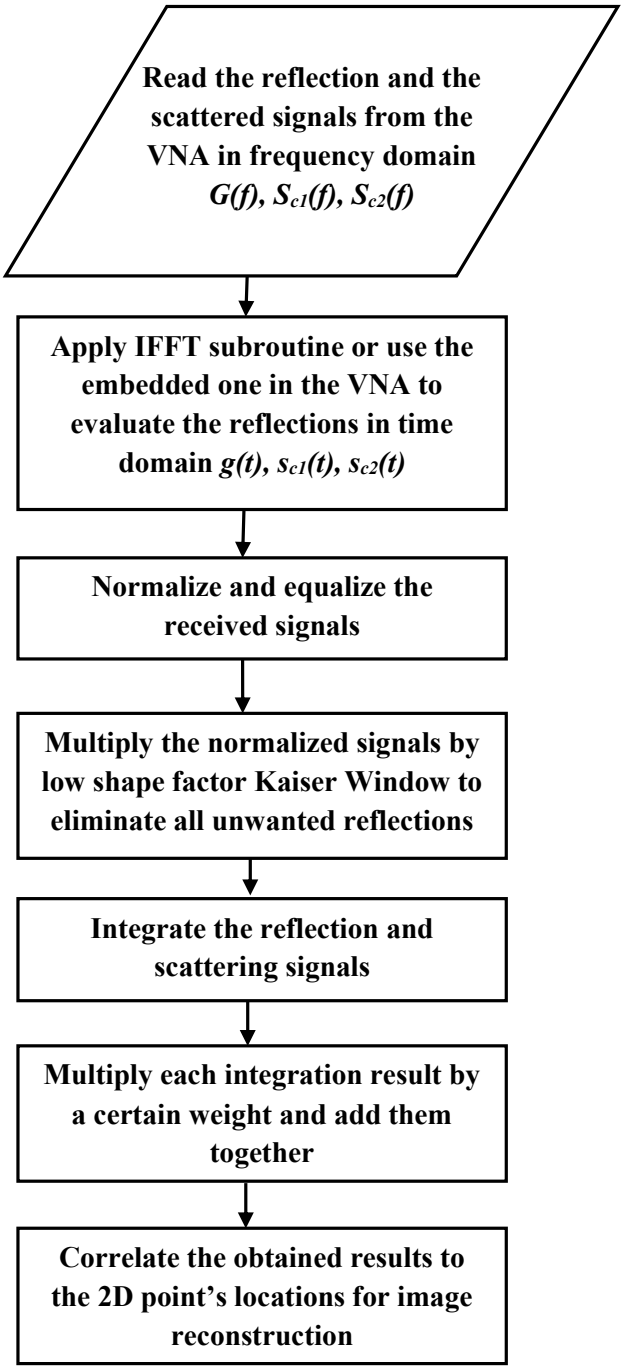

Figure 6.40 MMW imagining / detection algorithm.

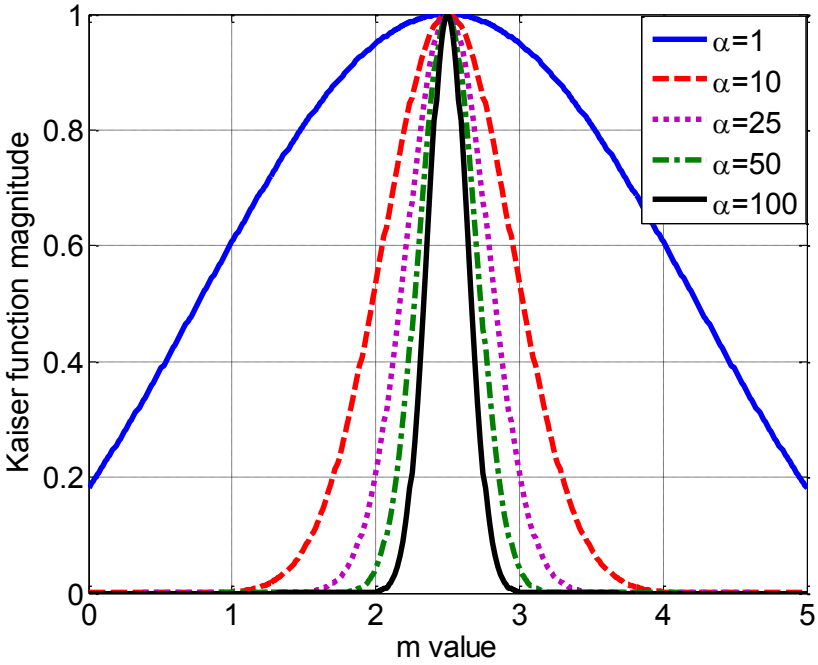

Figure 6.41 Kaiser function for different values of α.

6.3.2.4 Results and Discussion

After constructing and connecting the system shown in Fig. 6.24 and calibrating the VNA using standard calibration procedure over the frequency range of 30 GHz to 32 GHz, the reflection and the scattering data in frequency domain is measured. The measured results are then converted into time domain using the time domain conversion tool embedded in the VNA. Data collection and recording processes are done sequentially to cover all the testing points in the scanning area.

Fig. 6.42 shows the sensor response in front of an absorber. There are some differences between the peaks of the scattered signals $a_{sc1}(t)$ and $a_{sc2}(t)$ because of some fabrication, alignment and soldering variations in the three mounted horns. However, these

differences can be considered as static errors that can be added to every sampling point and easily eliminated through the normalization process.

Figs. 6.43-6.45 show a comparison between the normalized reflected back signal $g_n(t)$, the normalized scattered signals $s_{c1n}(t)$ and $s_{c2n}(t)$ signal levels for the vertical target orientation in two different sensor positions. The first one when the sensor is centered over square No. 50, i.e. over the metallic target, while the second when the sensor position is shifted 2 cm in the negative y direction away from the target, i.e. centered over square No. 48. It can be noticed a level difference of 10 mV, 15 mV and 2 mV in the first peak of $g_n(t)$, $s_{c1n}(t)$ and $s_{c2n}(t)$, respectively. These levels are fair enough to differentiate between the existence and no existence of the target. Almost same level differences with some minor variations can be detected for the other target orientations.

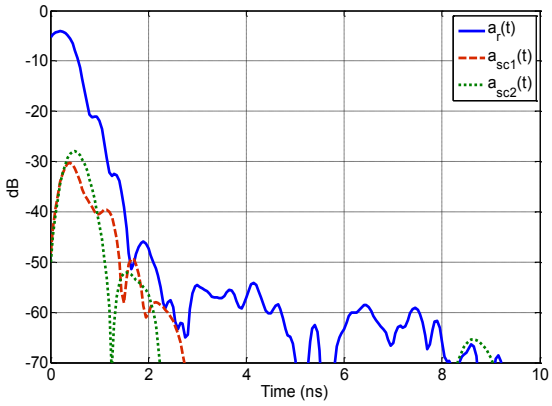

Figure 6.42 Triple antenna sensor response in front of an absorber ($a_r(t)$, $a_{sc1}(t)$ and $a_{sc2}(t)$).

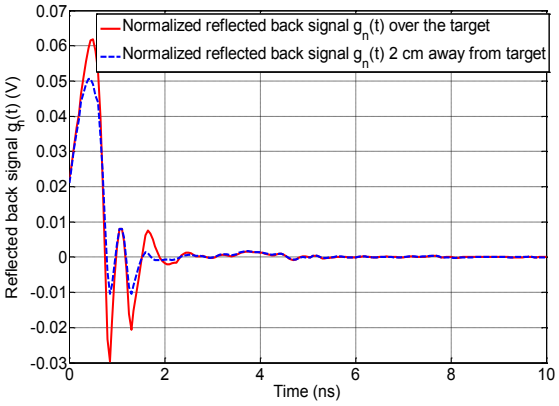

Figure 6.43 Normalized reflection signal $g_n(t)$, over the metallic target and 2 cm away.

Reflection and scattered data can be processed using Matlab in order to plot a complete image of the scanning domain with the hidden target. The first investigated case is the vertical orientation of the target. As shown in Fig. 6.46 (a), the reflection based image

of the target is about 1 cm shorter than its actual size. The image based on combined reflection and scattering data, shown in Fig. 6.46 (b), shows a better realistic size. Figs. 6.47 (a) and (b) show the reconstructed images for the hidden target with 45 degree orientation. The reconstructed image in Fig. 6.47 (a) based on reflection data only shows strong reflections that may be due to the edge diffraction by testing points located on the edges of the target. However, considering both reflection and scattering data plays an important role in decreasing the edge diffraction effect as shown in Fig. 6.47 (b). The horizontal orientation target case is presented in Fig. 6.48. Considering both reflection and scattering data in this case enhances the reconstructed target image dimensions, especially the target width and its resolution.

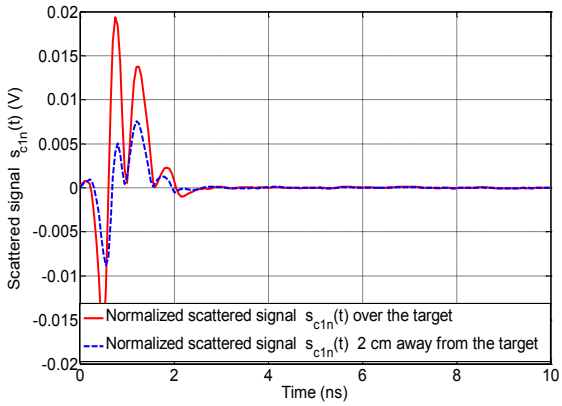

Figure 6.44 Normalized scattering signal $s_{c1n}(t)$ over the metallic target and 2 cm away.

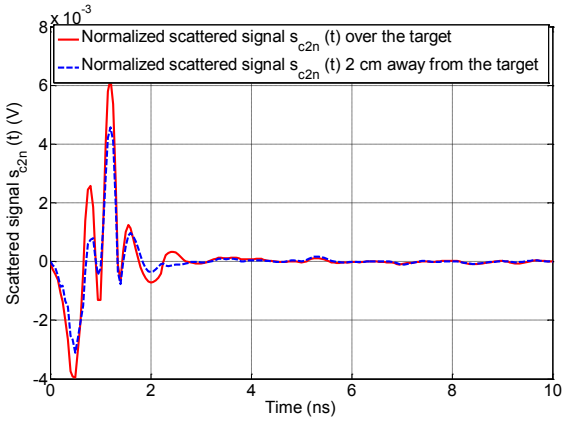

Figure 6.45 Normalized scattering signal $s_{c2n}(t)$over the metallic target and 2 cm away.

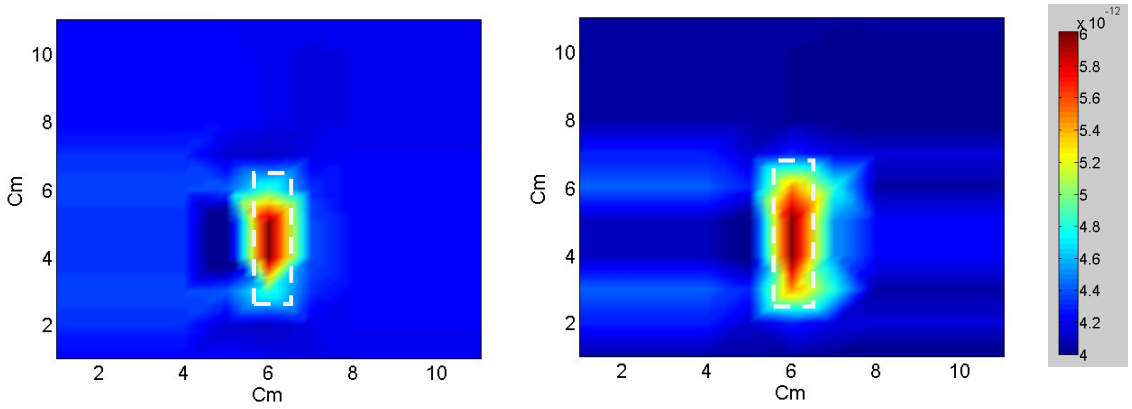

(a) (b)

Figure 6.46 Reconstructed image for the vertical target using (a) reflection data only (b) reflection plus scattering data.

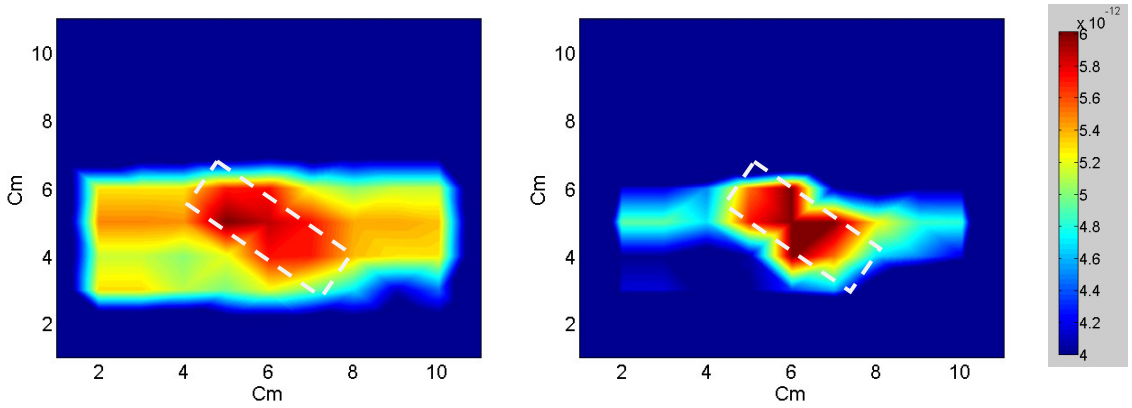

(a) (b)

Figure 6.47 Reconstructed image for the 45^{o} inclined target using (a) reflection data only (b) reflection plus scattering data.

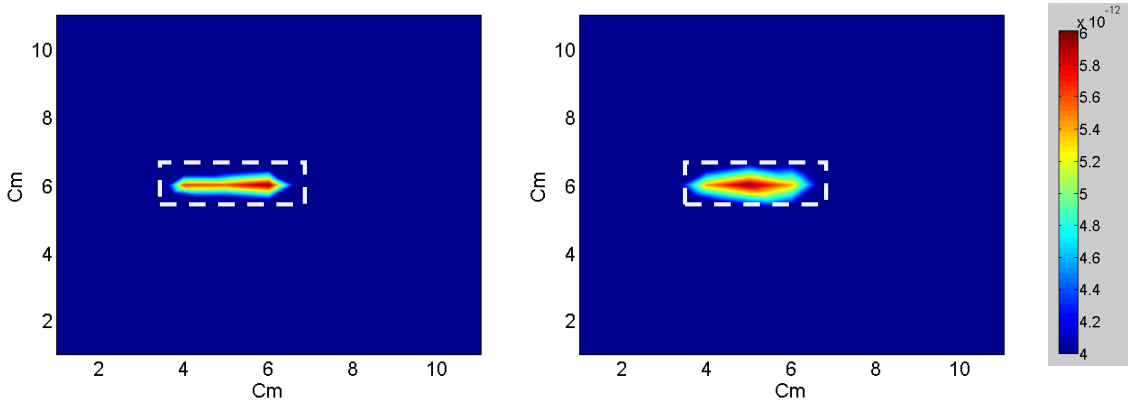

(a) (b)

Figure 6.48 Reconstructed image for the horizontal target using (a) reflection data only (b) reflection plus scattering data.

6.4 Summary

In this chapter, two distinct categories of microwave detection / imaging experiments are introduced. The first category involves UWB TWMI applications, while the second one focuses on MMW detection / imaging applications.

Some experimental work has been carried out using an accurate and easy to build UWB through wall gap detection system. The coupled-slot UWB antenna with a circular radiator shape, presented in Chapter 4, is used as a testing sensor in the proposed system. The system proves its reliability not only in gap detection, but also in gap width estimation with an error percentage of 6.25% in the worst scenario. Another UWB mechanically scanning system for TWMI applications is presented. The system utilizes the 4-element BAVA array system as a scanning sensor. The proposed system exhibits a great ability in the detection of 4-cm metallic ball embedded between two walls.

A MMW hidden weapons detection / imaging system operating around 30 GHz is also presented. Two practical MMW imaging experiments have been carried out for imaging and detecting a small metallic coin under a three layer target emulating a human body. Two different antenna sensors have been used. The first sensor is a standard metallic horn while the second is a small weight and size hybrid antenna. Both antenna sensors show a remarkable imaging and detection performance in the experimental work. To improve the system accuracy, and to enhance the resolution of the reconstructed images, a new triple sensor is employed in the system. The sensor adopts reflection / scattering approach for hidden target detection. The modified sensor shows a great ability for detecting and imaging a rectangular strip hidden under the cotton layer in the body model with three different orientations (vertical, horizontal, and 45^{o} inclined).

Chapter 7

Conclusion and Future Work

7.1 Conclusion

In this thesis, multiple antenna probes for different security applications have been introduced. The proposed antenna elements have been simulated optimized, tested, and fabricated, seeking the best performance without any impact on their size and weight. The realized antenna probes can be categorized according to their operating frequency, to two different categories. The first is the UWB range (3.1 GHz to 10.6 GHz), which is selected as an operating band for the probes indented to be used for TWMI applications, including hidden tunnel detection and hidden target detection / imaging behind walls. The MMW range is selected as an operating band for antenna probes / sensors intended to be employed in human body scanners for hidden target detection / imaging with the passengers at the airports and gate terminals. Different design techniques have been adopted to design such probes, including hybridization and array principles. All the proposed probe designs show good performance in terms of good impedance matching over the targeted band (i.e. $S_{11} \leq$ 10 dB), realized gain, radiation patterns, and minimal time domain distortion, especially in the case of UWB antenna sensors. The methodology and prototyping of these antenna probes have been presented and discussed extensively. Some of the realized antennas have been employed in a practical detection / imaging systems to verify their ability to serve as a scanning probe. The antenna probes show an encouraging performance, making them suitable to be employed in future detection / imaging systems, replacing the heavy, bulky, and expensive traditional metallic antennas used in commercial systems.

In Chapter 4, multiple antenna prototypes for UWB detection / imaging applications have been introduced. Three of these antenna probes are based on elliptical coupled-slot approach with different radiator shapes including circular, elliptical and crescent ring radiator. The calculated impedance bandwidth of proposed antenna designs ranges from 3 GHz to beyond 14 GHz for a reflection coefficient (S_{11}) that is less than -10dB. It can be noticed that the UWB with a circular radiator has more stable gain compared with the two other designs over the whole frequency band of interest. However, the proposed antenna designs are considered to be good candidates for UWB applications, especially detection applications. Another high gain UWB antenna based on BAVA approach has been introduced. This antenna exhibits an end-fire radiation pattern with higher gain (around 10 dB over the operating band) than the coupled-slot prototypes. These characteristics make it a good candidate for UWB imaging applications providing better resolution.

Adopting hybrid technology as a gain enhancing technique, multiple high efficient antenna probes have been realized to be employed as an efficient scanning sensor in an active MMW detection / imaging system. The proposed designs, presented in Chapter 5, incorporate hybrid circular waveguide / microstrip patch, microstrip patch/ conical horn, DRA / conical horn and x-slot / conical horn. Moreover, array technology has been considered as an alternative technique for gain enhancement.

The microstrip / circular waveguide hybrid antenna exhibits a good performance in terms of operating band and radiation characteristics. It has a realized gain around 10 dB, besides it is characterized by an easy fabrication process.

The microstrip patch / conical horn hybrid antenna is considered as an upgrade for the two former hybrids. Replacing the open-ended circular waveguide with a surface mounted horn enhances the overall realized gain to 12 dB without any sacrificing of the operating bandwidth. In addition, the antenna weight and size are small compared with classical horn antennas which allow integration and forming arrays for increasing the overall gain, making this antenna element our best choice as a scanning probe.

In order to reduce the copper losses occurs in the metallic patch radiator, the circular microstrip patch is replaced by a cylindrical DRA forming DRA / conical horn hybrid. DRA excitation is achieved through a rectangular slot in the ground plane. The antenna exhibits good impedance bandwidth of about 1.5 GHz (5% around its center frequency). The overall realized gain is almost 11.2 dB. Despite the deterioration of the antenna bandwidth, the antenna is still considered to be a good candidate for imaging applications.

Finally, a high gain circularly polarized x-slot antenna with a surface mounted horn is presented. The antenna prototype exhibits a good impedance bandwidth of about 1.05 GHz (3% around its center frequency). The overall antenna gain is almost 15 dB, which makes this design useful for various types of MMW imaging applications.

For enhanced detection / imaging capabilities, a triple antenna sensor for MMW imaging / detection applications is presented. The proposed sensor consists of three adjacent antenna elements based on the microstrip patch / conical horn hybrid introduced later. The sensor is implemented and employed in a practical MMW imaging system. The proposed sensor shows very good ability to detect and plot an approximated image for a hidden target with different orientations.

Detection / imaging results carried out over both UWB and MMW ranges were included in Chapter 6. Using the UWB antenna prototype with circular ring as a detection probe, an accurate and easy to build UWB through wall gap detection system based on TDR approach was built. Some numerical and practical UWB imaging experiments were carried out for gap detection between walls made of different materials using time domain measurements. The realized system shows a remarkable performance in both gap detection and gap width determination with a very high precision with an error percentage not more than 6.25% in the worst case.

Based on the high-gain BAVA antenna element design, a 4-element antenna array has been built as an improved sensor for TWMI applications. The proposed array system shows a great ability in the detection of a small metallic target behind embedded between two walls. The overall array system characteristics make it the optimum choice as a scanning probe in microwave imaging and detection systems.

Some practical MMW detection / imaging experiments were carried out for detecting a hidden target under a cotton layer in the three layers body model. The primary experiments were intended to detect a small circular metallic coin using the hybrid microstrip patch / conical horn antenna. To enhance the detection / imaging accuracy, the scanning sensor is replaced by the triple antenna sensor. Imaging / detection algorithm was developed and implemented using Matlab to process, interpolate and plot the measured data over the scanning domain. Three different target orientations were considered (inclined, horizontal and vertical). The triple antenna sensor shows a remarkable imaging / detection performance and target size estimation in the experimental work.

7.2 Contributions

The main contribution of this work can be divided into two main areas. The first one includes design of several antenna elements, while the second one is concerned with the development of two detection systems. The related publications are listed at the end of the references.

7.2.1 Antenna Probe Research

The contributions on this activity can be summarized as:

- Design and implementation of slot coupled UWB antenna probes with different radiator shapes (circular, elliptical, and crescent) [J1], [C1].
- Design and implementation of high gain BAVA UWB antenna for TWMI application [C6].
- Design and implementation of multiple MMW antenna probes for detection / imaging applications, including incorporate hybrid DRA / microstrip patch [C2], SIW / microstrip patch [C3], circular waveguide / microstrip patch [C4], microstrip patch / conical horn [J2], DRA / conical horn [C9] and x-slot / conical horn [C7], [J5].
- Design and implementation of a triple antenna sensor based on a reflection / scattering approach [J4].

7.2.2 System Level Research

- Introducing an accurate UWB hidden tunnel detection algorithm and system [J3].
- Design and verification of a practical UWB hidden target detection / imaging system [C6] including associated algorithm.
- Developing a MMW detection / imaging algorithm based on reflection only [C5].

- Developing a novel algorithm for MMW detection / imaging based on reflection / scattering approach [J4] and associated hardware system implementation.

7.3 Future Work

The following list summarizes some possible ideas for future work:

(a) Verifying the proposed TWMI system on different walls made from different materials (concrete, rocks, wood, etc.).

(b) Investigating new techniques for gain enhancement and size reduction for MMW antenna probes.

(c) Developing a real-time MMW scanning system for hidden target detection / imaging, including both hardware and associated software.

(d) Considering dielectric-based hidden targets with different geometrical shapes instead of using metallic targets.

(e) Looking for a better and efficient electronically scanning system that can provide ultra-fast beam steering ability using digital-controlled phase shifters.

References

[1] Fear, E.C.; Meaney, P.M.; Stuchly, M.A, "Microwaves for breast cancer detection?" *Potentials, IEEE*, vol. 22, no. 1, pp. 12-18, Feb/Mar 2003.

[2] Huang, C.L.; Zhu, S.P.; Lu, M., "Miniature multimode deep ground penetrating radar," *Ground Penetrating Radar (GPR), 2010 13th International Conference on*, pp. 1-5, 21-25 June 2010.

[3] Sun, Y.; Li, J., "Time-frequency analysis for plastic landmine detection via forward-looking ground penetrating radar," *Radar, Sonar and Navigation, IEE Proceedings,* vol. 150, no. 4, pp. 253-61, 1 Aug. 2003.

[4] Zhou, Y., "Microwave imaging based on wideband range profiles," *Progress In Electromagnetics Research Letters*, vol. 19, pp. 57-65, 2010.

[5] Conceição, R. C.; O'Halloran, M.; Glavin, M.; Jones, E., "Comparison of planar and circular antenna configurations for breast cancer detection using microwave imaging," *Progress In Electromagnetics Research*, vol. 99, pp. 1-20, 2009.

[6] Aryanfar, F.; Sarabandi, K., "Through wall imaging at microwave frequencies using space-time focusing", *Antennas and Propagation Society International Symposium*, 2004. *IEEE*, vol. 3, pp. 3063- 3066, 20-25 June 2004.

[7] Yemelyanov, K.M.; Engheta, N.; Hoorfar, A.; McVay, J.A., "Adaptive polarization contrast techniques for through-wall microwave imaging applications", *Geoscience and Remote Sensing, IEEE Transactions on*, vol. 47, no. 5, pp. 1362-1374, May 2009.

[8] FCC, "First report and order, revision of part 15 of the commission's rules regarding ultra-wideband transmission systems", FCC02- 48, April 2002.

[9] James, D.T., *Ultra-wideband radar technology*, CRC Press LLC, 1st edition, 2001.

[10] http://en.wikipedia.org/wiki/Metal_detector, "web page", 5/8/2014.

[11] Huang, H., "Flexible Wireless Antenna Sensor: A Review," *Sensors Journal*, *IEEE*, vol. 13, no. 10, pp. 3865-3872, Oct. 2013.

[12] Dallinger, A.; Schelkshorn, S.; Detlefsen, J., "Short distance related security millimeter-wave imaging systems," *German Microwave Conference - GeMIC 2005*, pp. 244-246, April 2005.

[13] Dallinger, A.; Schelkshorn, S.; Detlefsen, J., "Millimeter-wave imaging of humans - basic experiments," *Infrared and Millimeter Waves, and 12th International Conference on Terahertz Electronics*, *Conference Digest of the 2004 Joint 29th International Conference on*, pp.521-522, 27 Sept.-1 Oct. 2004.

[14] Peichl, M.; Dill, S.; Jirousek, M.; Suess, H., "Passive microwave remote sensing for security applications," *Radar Conference, EuRAD 2007*, pp.32-35, 10-12 Oct. 2007.

[15] Dill, S; Peichl, M.; Schreiber, E.; Süß, H., "Passive MMW imaging systems for security applications," *International Radar Symposium - IRS 2009*, pp. 225-228, 9-11Sept. 2009.

[16] Doghri, Ali; Ghiotto, A.; Djerafi, T.; Ke Wu, "Early demonstration of a passive millimeter-wave imaging system using substrate integrated waveguide technology," *Mediterranean Microwave Symposium (MMS)*, *2011 11th*, pp.215-218, 8-10 Sept. 2011.

[17] Ahmed, S.S.; Schiessl, A.; Schmidt, L., "A novel fully electronic active real-time imager based on a planar multistatic sparse array," *Microwave Theory and Techniques, IEEE Transactions on*, vol. 59, no. 12, pp. 3567-3576, Dec. 2011.

[18] Nilsson, E.; Baath, L., "Radar interferometric measurements with a planar patch antenna array," *Sensors Journal, IEEE*, vol. 7, no. 7, pp. 1025-1031, July 2007.

[19] Rizzoli, V.; Costanzo, A.; Montanari, E.; Benedetti, A., "A new wireless displacement sensor based on reverse design of microwave and millimeter-wave antenna array," *Sensors Journal, IEEE*, vol. 9, no. 11, pp. 1557-1566, Nov. 2009.

[20] Chan, Y.K.; Koo, V.C., "An introduction to synthetic aperture radar (SAR)," *Progress In Electromagnetics Research B*, vol. 2, pp. 27–60, 2008.

[21] Chinnam, D.M. et al., "Implementation of a low cost synthetic aperture radar using Software Defined Radio", *Computing Communication and Networking Technologies (ICCCNT)*, *2010 International Conference on*, pp. 1-7, 29-31 July 2010.

[22] Patel, V.M., Easley, G.R., Healy, D.M., Chellappa, R. , "Compressed synthetic aperture radar" *Selected Topics in Signal Processing, IEEE Journal of* , vol. 4, no. 2, pp. 244-254, April 2010.

[23] Binbin, C.; et al., "Real-time imaging with a 140 GHz inverse synthetic aperture radar," *Terahertz Science and Technology, IEEE Transactions on*, vol. 3, no. 5, pp. 594-605, Sept. 2013.

[24] Cataldo, A.; Tarricone, L.; Attivissimo, F.; Trotta, A., "A TDR method for real-time monitoring of liquids," *Instrumentation and Measurement, IEEE Transactions on*, vol. 56, no. 5, pp. 1616-1625, Oct. 2007.

[25] Suksmono, A.B.; Bharata, E.; Lestari, A.A.; Yarovoy, A.G.; Ligthart, L.P., "compressive stepped-frequency continuous-wave ground-penetrating radar," *Geoscience and Remote Sensing Letters, IEEE* , vol. 7, no. 4, pp. 665-669, Oct. 2010.

[26] Huang, C.L.; Zhu, S.P.; Ming, L., "Miniature multimode deep ground penetrating radar," *Ground Penetrating Radar (GPR), 2010 13th International Conference on* , pp. 1-5, 21-25 June 2010.

[27] Sun, Y.; Li, J., "Time-frequency analysis for plastic landmine detection via forward-looking ground penetrating radar", *Radar, Sonar and Navigation, IEE Proceedings*, vol. 150, no. 4, pp. 253-61, 1 Aug. 2003.

[28] Ghasr, M.T.; Kharkovsky, S.; Bohnert, R.; Hirst, B.; Zoughi, R., "30 GHz linear high-resolution and rapid millimeter wave imaging system for NDE," *IEEE Trans. Instrum. Meas.*, vol. 61, no. 9, pp. 4733-4740, June 2013.

[29] Khor, W. C.; Bialkowski, M.E.; Crozier, S., "Microwave imaging using a planar scanning system with step-frequency synthesized pulse," *Microwave Conference Proceedings*, 2005, *APMC 2005*, *Asia-Pacific Conference Proceedings*, vol. 1, pp., 4-7, Dec. 2005.

[30] Thajudeen, C.; Zhang, W.; Hoorfar, A., "Efficient forward modeling of large scale buildings and through-the-wall radar imaging scenarios," *28th Annual Review of Progress in Applied Computational Electromagnetics (ACES)*, Columbus, Ohio, pp. 122-126, April 2012.

[31] Buonanno, A.; D'Urso, M.; Prisco, G.; Farina, A., "A model-based signal processor to see inside buildings," *26th Annual Review of Progress in Applied Computational Electromagnetics (ACES)*, Tampere, Finland, pp. 846-851, April 2010.

[32] Nikolic, M.; Nehorai, A.; Djordjevic, A., "Estimating distributed objects inside buildings by moving sensors," *23rd Annual Review of Progress in Applied Computational Electromagnetics (ACES)*, Verona, Italy, pp. 409-414, March 2007.

[33] Lubecke, V.M.; Boric, O.; Host, A.; and Fathy, A.E., "Through-the-wall radar life detection and monitoring". *IEEE Microwave symposium*, pp. 769-772, June 2007.

[34] Mahfouz, M.; Fathy, A.; Yang, Y.; Elhak Ali, E.; Badawi, A., "See through- wall imaging using ultra wideband pulse systems," *IEEE Applied Imagery and Pattern Recognition Workshop*, pp. 19-21, Oct. 2005.

[35] Lin, M.; Zhongzhao, Z.; Xuezhi, T., "A novel through-wall imaging method using ultra wideband pulse system," *IEEE Conf. on Intelligent Hiding and Multimedia Signal Processing*, pp. 147-150, Dec. 2006.

[36] Cara, D.D.; Trajkovikj, J.; Torres-Sanchez, R.; Zurcher, J.; Skrivervik, A.K., "A low profile UWB antenna for wearable applications: The tripod kettle antenna (TKA)," *Antennas and Propagation (EuCAP), 2013 7th European Conference on*, pp.3257-3260, 8-12 April 2013.

[37] Koohestani, M.; Zurcher, J.-F.; Moreira, A.; Skrivervik, A., "A Novel, Low-Profile, Vertically-Polarized UWB Antenna for WBAN," *Antennas and Propagation, IEEE Transactions on*, no. 99, pp. 1-7, Jan. 2014.

[38] Sibille, A., "Compared performance of UWB antennas for time and frequency domain modulation", *28th URSI General Assembly*, New Delhi, India, 2005.

[39] Alipour, A.; Hassani, H.R., "A Novel omni-directional UWB monopole antenna," *Antennas and Propagation, IEEE Transactions on*, vol. 56, no. 12, pp. 3854-3857, Dec. 2008.

[40] Guha, D.; Gupta, B.; Antar, Y.M.M., "New pawn-shaped dielectric ring resonator loaded hybrid monopole antenna for improved ultrawide bandwidth," *Antennas and Wireless Propagation Letters, IEEE*, vol. 8, no. 1, pp.1178-1181, 2009.

[41] Lao, J.; Jin, R.; Geng, J.; Wu, Q., "An ultra-wideband microstrip elliptical slot antenna excited by a circular patch", *Microwave Optical Technol. Lett.,* vol. 50, no. 4, pp. 845–846, Feb. 2008.

[42] Yoon, J.H.; Han, G.H.; Kim, D. H.; Lee, J.C.; Woo, S.M.; Kim, H.H., "Design of triangular slot antenna for triple-band (2.4/5.2/5.8 GHz) antenna with fork-like tuning stub", *Microwave Optical Technol. Lett.*, vol. 49, no. 7, pp. 1561–1565, April 2007.

[43] Sorbello, G.; Pavone, M.; Russello, L., "Numerical and experimental study of a rectangular slot antenna for UWB communications", *Microwave Optical Technol. Lett.*, vol. 46, no. 4, pp. 315–319, Aug. 2005.

[44] Ma, T.G.; Jeng, S.K.; "Planar miniature tapered-slot-fed annular slot antennas for ultra-wideband radios," *IEEE Trans. Antennas Propagation*, vol. 53, pp. 1194–1202, Mar. 2005.

[45] Sorbello, G.; Consoli, F.; Barbarino, S., "Numerical and experimental analysis of a circular slot antenna for UWB communications," *Microwave Optical Technol. Lett.*, vol. 44, no. 5, pp. 465–470, Jan. 2005.

[46] Gao, G.P.; Hu, B.; Zhang, J.S., "Design of a miniaturization printed circular-slot UWB antenna by the half-cutting method," *Antennas and Wireless Propagation Letters, IEEE*, vol. 12, no. 12, pp. 567-570, 2013.

[47] Gautam, A.K.; Yadav, S.; Kanaujia, B.K., "A CPW-fed compact uwb microstrip antenna," *Antennas and Wireless Propagation Letters, IEEE*, vol. 12, no. 12, pp.151-154, 2013.

[48] Kuiwen, X.; Zhongbo, Z.; Huan, L.; Jiangtao, H.; Changzhi, L.; Lixin R., "A printed single-layer UWB monopole antenna with extended ground plane stubs," *Antennas and Wireless Propagation Letters, IEEE* , vol. 12, no. 12, pp.237-240, 2013.

[49] Srifi, M.N.; Podilchak, S.K.; Essaaidi, M.; Antar, Y.M.M., "Compact disc monopole antennas for current and future ultrawideband (UWB) applications," *Antennas and Propagation, IEEE Transactions on*, vol. 59, no. 12, pp. 4470-4480, Dec. 2011.

[50] Fereidoony, F.; Chamaani, S.; Mirtaheri, S.A., "UWB monopole antenna with stable radiation pattern and low transient distortion," *Antennas and Wireless Propagation Letters, IEEE*, vol.10, no. 10, pp.302-305, 2011.

[51] Levy, M.; Kumar, D.S.; Dinh, A., "A novel fractal UWB antenna for earthquake and tsunami prediction application (LETPA)," *Electrical and Computer Engineering (CCECE), 2013 26th Annual IEEE Canadian Conference on*, pp.1-4, 5-8 May 2013.

[52] Oraizi, H.; Hedayati, S., "Miniaturized UWB monopole microstrip antenna design by the combination of Giusepe Peano and Sierpinski carpet fractals," *Antennas and Wireless Propagation Letters, IEEE*, vol. 10, no. 10, pp. 67-70, 2011.

[53] Fallahi, H.; Atlasbaf, Z., "Study of a class of UWB CPW-fed monopole antenna with fractal elements," *Antennas and Wireless Propagation Letters, IEEE*, vol.12, no. 12, pp.1484-1487, 2013.

[54] Bitchikh, M.; Ghanem, F., "An UWB to three sub-bands frequency reconfigurable antipodal Vivaldi antenna," *Antennas and Propagation Society International Symposium (APSURSI), 2013 IEEE*, pp. 670-671, 7-13 July 2013.

[55] Teni, G.; Ning Zhang; Jinghui Qiu; Pengyu Zhang, "Research on a novel miniaturized antipodal Vivaldi antenna with improved radiation," *Antennas and Wireless Propagation Letters, IEEE*, vol. 12, no. 12, pp. 417-420, 2013.

[56] Chao, Y.; Wei, H.; Leung, C.; Guohua, Z.; Chen, Y.; Wei, Q.; Kuai, Z., "Ultrawideband Printed log-periodic dipole antenna with multiple notched bands," *Antennas and Propagation, IEEE Transactions on* , vol. 59, no. 3, pp. 725-732, March 2011.

[57] Orlob, C.; Dao, Q. H.; Geck, B., "Conformal log.-periodic antenna with integrated feeding network for UWB-MIMO applications," *Microwave Conference (GeMiC), 2012 The 7th German*, pp. 1-4, 12-14 March 2012.

[58] Omar, A.A.; Qaroot, A.; Scardelletti, M.C., "UWB coplanar-waveguide-fed spiral slot antenna," *Antennas and Propagation (EuCAP), 2013 7th European Conference on*, pp. 2901-2902, 8-12 April 2013.

[59] Licul, S.; Noronha, J.A.N.; Davis, W.A.; Sweeney; D.G.; Anderson, C.R.; Bielawa, T.M., "A parametric study of time-domain characteristics of possible UWB antenna architectures," *IEEE 58th Vehicular Technology Conference, VTC 2003-Fall*, vol. 5, pp. 3110-3114, 6-9 October, 2003.

[60] Harvey, B.A.; Howard, D.H.; et al., "An analysis of MMW wireless LANs for LPVAJ command post communications," *Military Communications Conference, MILCOM '93*. Conference record, pp. 580- 584, 1993.

[61] Emerson, D.T., "The work of Jagadis Chandra Bose: 100 years of millimeter-wave research," *Microwave Theory and Techniques, IEEE Transactions on*, vol. 45, no. 12, pp. 2267-2273, Dec 1997.

[62] Costanzo, S.; Venneri, I.; Massa, G.D.; Amendola, G., "Hybrid array antenna for broadband millimeter-wave applications," *Progress In Electromagnetics Research*, vol. 83, pp. 173-183, 2008.

[63] Akkermans, J.A.G., Herben, M.H.A. "Millimeter-Wave Antenna With Adjustable Polarization", *Antennas and Wireless Propagation Letters, IEEE,* vol. 7, pp.539 – 542, 2008.

[64] Pilard, R.; Montusclat, S.; Elwertowska, A.; Gloria, D.; Le Pennec, F.; Person, C.; , "Size reduction and input impedance increase in advanced MMW silicon integrated double-slotted antenna using fractal and director slot layout," *Antenna Technology: Small Antennas and Novel Metamaterials, 2008, iWAT 2008 International Workshop on*, pp.294-297, 4-6 March 2008.

[65] Hwann-Kaeo, C.; I-Shan, C.; Nan-Wei, C., “Corrections to “V-band on-chip dipole-based antenna” [Oct. 09 2853-2861]," *Antennas and Propagation, IEEE Transactions on* , vol. 60, no. 4, pp. 2144-2145, April 2012.

[66] Rashidian, A.; Klymyshyn, D.M.; Aligodarz, M.T.; Boerner, M.; Mohr, J., “Development of polymer-based dielectric resonator antennas for millimeter-wave applications,” *Progress In Electromagnetics Research C*, vol. 13, pp. 203-216, 2010.

[67] Perron, A.; Denidni, T.A.; Sebak, A.R, “High-gain hybrid dielectric resonator antenna for millimeter-wave applications: Design and Implementation,” *Antennas and Propagation, IEEE Transactions on*, vol. 57, no. 10, Part 1, pp. 2882 - 2892, Oct. 2009.

[68] Kramer, O.; Djerafi, T.; Ke Wu, “Very small footprint 60 GHz stacked Yagi antenna array,” *Antennas and Propagation, IEEE Transactions on*, vol. 59, no. 9, pp. 3204-3210, Sept. 2011.

[69] Tan, K.J.; Luan, X.Z., “Millimeter wave circularly polarized substrate integrated waveguide antenna,” *ICMMT 2008*. vol. 3, pp. 1058 - 1061, April 2008.

[70] Tian, Y.Y.; Wei, H.; Yan, Z., “Wideband millimeter-wave substrate integrated waveguide cavity-backed rectangular patch antenna,” *Antennas and Wireless Propagation Letters, IEEE*, vol. 13, no. 13, pp. 205-208, 2014.

[71] Alhalabi, R.A.; Yi, C.; Rebeiz, G.M., “Self-shielded high-efficiency Yagi-Uda antennas for 60 GHz communications,” *Antennas and Propagation, IEEE Transactions on*, vol. 59, no. 3, pp. 742-750, March 2011.

[72] Li, M.; Luk, K.-M., "A low-profile unidirectional printed antenna for millimeter-wave applications," *Antennas and Propagation, IEEE Transactions on*, vol. 62, no. 99, pp.1232-1237, Dec. 2013.

[73] Ghassemi, N.; Ke Wu, "Planar high-gain dielectric-loaded antipodal linearly tapered slot antenna for E- and W-band gigabyte point-to-point wireless services," *Antennas and Propagation, IEEE Transactions on*, vol. 61, no. 4, pp. 1747-1755, April 2013.

[74] Al-Tarifi, M.A.; Anagnostou, D.E.; Amert, A.K.; Whites, K.W., "Bandwidth enhancement of the resonant cavity antenna by using two dielectric superstrates," *Antennas and Propagation, IEEE Transactions on*, vol. 61, no. 4, pp. 1898-1908, April 2013.

[75] Ying, S.Z.; Wei, H., "A Millimeter-wave gain enhanced multi-beam antenna based on a coplanar cylindrical dielectric lens," *Antennas and Propagation, IEEE Transactions on*, vol. 60, no. 7, pp. 3485-3488, July 2012.

[76] Gentile, C.; Kik, A., "A comprehensive evaluation of indoor ranging using ultra-wideband technology", *EURASIP Journal on Wireless Communications and Networking*, vol. 2007, id. 86031, 2007.

[77] Craddock; I.J.; Klemm, M.; Leendertz, J.; Preece, A.W.; Benjamin, R., "An improved hemispeherical antenna array design for breast imaging", *Antennas and Propagation, 2007, EuCAP 2007*, *The Second European Conference on*, , pp.1-5, 11-16 Nov. 2007.

[78] http://www.camero-tech.com/product.php?ID=40, "web page", 4th April 2014.

[79] http://www.cambridgeconsultants.com/projects/prism-200-through-wall-radar, "web page", 4th April 2014.

[80] http://www.military.com/ContentFiles/techtv_update_soldiervision.htm,"web page", 4th April 2014.

[81] Harmer, S.; Andrews, D.; et al., "Ultra wide band detection of on body concealed weapons using the out of plane polarized late time response," *Millimeter Wave and Terahertz Sensors and Technology II*, vol. 7485, no. 1. , 2009.

[82] http://niremf.ifac.cnr.it/tissprop/htmlclie/htmlclie.htm#atsftag, "web page", 4th April 2014.

[83] Naomi, E.A.; Andrés, C.C.; Gonzalo, R.; "Multispectral mm-wave imaging: materials and images," *Proc. SPIE 6948, Passive Millimeter-Wave Imaging Technology XI*, 694803, April 04, 2008.

[84] Barker, D.H.; Hodges, D.T.; Hartwig, T.S., "Far infrared imaginary", *Proceedings of SPICE*, vol. 67, 1975.

[85] Dallinger, A.; Schelkshorn, S.; Detlefsen, J., "Short distance related security millimeter-wave imaging systems," *German Microwave Conference - GeMIC 2005*, April 2005.

[86] Dallinger, A.; Schelkshorn, S.; Detlefsen, J., "Millimeter-wave imaging of humans - basic experiments", *Infrared and Millimeter Waves, 2004 and 12th International Conference on Terahertz Electronics, 2004. Conference Digest of the 2004 Joint 29th International Conference on* , pp. 521- 522, 27 Sept.-1 Oct. 2004.

[87] Sheen, D.M.; McMakin, D.L.; Collins, H.D.; Hall, T.E.; Severtsen, R.H., "Concealed explosive detection on personnel using a wideband holographic millimeter-wave imaging system", *Proc. SPIE 2755, Signal Processing, Sensor Fusion, and Target Recognition V*, vol. 2755, June 2000.

[88] Ahmed, S.S.; Schiessl, A.; Schmidt, L., "Novel fully electronic active real-time millimeter-wave imaging system based on a planar multistatic sparse array," *Microwave Symposium Digest (MTT), 2011 IEEE MTT-S International*, pp.1-4, 5-10 June 2011.

[89] http://www.microsemi.com/products/screening-solutions/gen-2, "web page", 4th April 2014.

[90] http://www.sds.l-3com.com/advancedimaging/provision.htm, "web page", 4th April 2014.

[91] Constantine A. Balanis, *Antenna Theory Analysis and Design*, Third edition, John Wiley& Sons, Inc., 2005.

[92] Deslandes, D.; K. Wu, "Integrated microstrip and rectangular waveguide in planar form," *IEEE Microwave. Guided Wave Lett*, vol. 11, no. 2, pp. 68–70, Feb. 2001.

[93] K. Wu, "Integration and interconnect techniques of planar and nonplanar structures for microwave and millimeter-wave circuits—Current status and future trend," in 2001 *Asia–Pacific Microwave Conf*., Taipei, Taiwan, R.O.C., Dec. 3–6, 2001, pp. 411–416.

[94] Ke Wu; Deslandes, D.; Cassivi, Y., "The substrate integrated circuits - a new concept for high-frequency electronics and optoelectronics," *Telecommunications in Modern Satellite, Cable and Broadcasting Service, 2003. TELSIKS 2003. 6th International Conference on*, vol.1, pp. PIII-PX, 1-3 Oct. 2003.

[95] Ozturk, AK.; Paknys, R., "Analysis of propagation between rows of conducting cylinders that model solid surfaces using the same surface area rule," *Antennas and Propagation, IEEE Transactions on* , vol. 60, no. 5, pp. 2602-2606, May 2012.

[96] Deslandes, D.; Perregrini, L.; Arcioni, P.; Bressan, M.; K. Wu; et al., "Dispersion characteristics of substrate integrated rectangular waveguide," *IEEE Microwave Wireless Compon. Lett.,* vol. 12, pp. 333-335, Sept. 2002.

[97] Schorr, M.G.; Beck, F.J., "Electromagnetic field of the conical horn", *Journal of applied Physics*, vol. 21, pp. 795-801, Aug. 1950.

[98] Harrington R.F., *Time harmonic electromagnetic fields*, McGraw-Hill Book Company, New York, 1961.

[99] Koop, H.E.M.; Dijk, J.; Maanderes, E.J., "On conical antennas", (technical report).

[100] Plourde, J. K.; Ren, C. L., "Application of dielectric resonators in microwave components," *IEEE Trans. Microwave Theory Tech*., vol. 29, no. 8, pp. 754–770, Aug. 1981.

[101] Long, S. A.; McAllister, M.; Shen, L. C., "The resonant cylindrical dielectric cavity antenna," *IEEE Trans. Antennas Propag*., vol. 31, no. 3, pp. 406–412, May 1983.

[102] Kishk, A.A.; Auda, H.A.; Ahn, B.C., "Accurate prediction of radiation patterns of dielectric resonator antennas," *Electron. Lett.*, vol. 23, pp. 1374–1375, 1987.

[103] Kishk, A.A., "Dielectric resonator antenna, a candidate for radar applications," *Radar Conference, 2003. Proceedings of the 2003 IEEE*, pp. 258- 264, 5-8 May 2003.

[104] Mongia, R.K.; Bhartia, P., "Dielectric resonator antennas-A review and general design relations for resonant frequency and bandwidth," *International Journal of Microwave and Millimeter-wave Computer Aided Engineering*, vol. 4, no. 3, pp. 230-247, 1994.

[105] Luk, K.M.; Leung, K.W., "Dielectric resonator antennas", *Research Studies Press*, June 1, 2002.

[106] Costanzo, S., "Hybrid array antenna for broadband millimeter-wave applications," *Progress In Electromagnetics Research*, PIER 83, pp. 173–183, 2008.

[107] Methfessel, S.; Lorenz-Peter, S., "Design of a balanced-fed patch-excite horn antenna at millimeter-wave frequencies," *Antennas and Propagation (EuCAP), 2010 Proceedings of the Fourth European Conference on*, pp.1-4, 12-16 April 2010.

[108] Kumar, P.; et al., "High gain microstrip antenna capacitive coupled to a square ring with surface mounted conical horn", *IJECT,* vol. 1, Issue 1, Dec. 2010.

[109] Shireen R., "Stacked patch excited horn antenna at 94 GHz", *Microwave and Optical Technology Letters*, pp. 2071-2074, vol. 50, no. 8, August 2008.

[110] Nasimuddin et al., "GAIN enhancement of aperture-coupled dielectric-resonator antenna with surface mounted horn", *URSI Proceeding Proc., general assembly*, 2005.

[111] Bedair, A., "Design and development of high gain wideband microstrip antenna and dgs filters using numerical experimentation approach", *Ph.D. thesis*, Guericke-Universität Magdeburg, June 2005.

[112] ANSYS HFSS, v15, ANSYS Corporation Software, Pittsburgh, PA, USA.

[113] CST Microwave Studio, Ver. 2014, Computer Simulation Technology, Framingham, MA, USA.

[114] T. Weiland, “A discretization model for the solution of Maxwell's equations for six component fields," *Archiv Elektronik und Uebertragungstechnik*, vol. 31; pp. 116-120, 1977.

[115] M. N. O. Sadiku, *Numerical Techniques in Electromagnetics*, Second Edition, CRC Press LLC, 2001.

[116] Courant, R., “Variational methods for the solution of problems of equilibrium and vibrations,” *Bulletin of the American Mathematical Society*, 49 (1943), pp. 1–23, 1943.

[117] Arlett, P.L. ; Bahrani, A.K. ; Zienkiewicz, O.C. , “Application of finite elements to the solution of Helmholtz's equation,” *Proceedings of the Institution of Electrical Engineers*, vol. 115, Issue 12, pp. 1762 – 1766, December 1968.

[118] Yee, K.S., “Numerical solution of initial boundary value problems involving Maxwell's equations in isotropic media,” *IEEE Transaction on Antennas and Propagation*, vol. 14, no. 3, pp. 302-307, 1966.

[119] Taflove, A., "Application of the finite-difference time-domain method to sinusoidal steady-state electromagnetic-penetration problems,” *IEEE Transactions on Electromagnetic Compatibility*, vol. 22, no. 3, pp. 191- 202, Aug. 1980.

[120] Jianxin Liang, “Antenna Study and Design for Ultra Wideband Communication Applications”, *PhD Thesis*, University of London, July 2006.

[121] Bourqui, J.; Okoniewski, M.; Fear, E.C., “Balanced antipodal Vivaldi antenna with dielectric director for near-field microwave imaging”, *Antennas and Propagation, IEEE Transactions on*, vol.58, no.7, pp.2318-2326, July 2010.

[122] Osama Ahmed, “Ultra-wideband antennas and components for wireless communication systems”, *Ph.D. Thesis*, Concordia University, Sept. 2011.

[123] Itoh, T.; Hsu, F.J., “Application of Inverted Strip Dielectric Waveguides for Measurement of Material Properties at Millimeter-Wave Frequencies,” *Microwave Conference, 1978. 8th European* , pp.823,827, 4-8 Sept. 1978.

[124] McCloy, John S.; Korolev, K.A.; Zijing Li; Afsar, M.N.; Sundaram, S.K., “Millimeter-wave dielectric properties of single-crystal ferroelectric and dielectric materials,” *Ultrasonics, Ferroelectrics and Frequency Control, IEEE Transactions on* , vol. 58, no. 1, pp.18-29, January 2011.

[125] Coonrod, J., “Understanding the variables of dielectric constant for PCB materials used at microwave frequencies,” *Microwave Conference (EuMC), 2011 41st European* , pp. 938-944, 10-13 Oct. 2011.

[126] Zhou, Y., "Microwave imaging based on wideband range profiles," *Progress In Electromagnetics Research Letters*, vol. 19, 57-65, 2010.

[127] Conceição, R.C.; O'Halloran, M.; Glavin, M.; Jones, E., “Comparison of planar and circular antenna configurations for breast cancer detection using microwave imaging,” *Progress In Electromagnetics Research*, vol. 99, pp. 1-20, 2009.

[128] AlShehri, S.A.; Khatun S., “UWB imaging for breast cancer detection using neural network,” *Progress In Electromagnetics Research C*, vol. 7, pp. 79-93, 2009.

[129] http://www.lynxmotion.com/c-130-al5d.aspx, “web page”, 7/4/2014.

[130] Aamna, M.; Ammar, S.; Rameez, T.; Shabeeb, S.; Rao, N.I.; Safwat, I., “2D beamforming for through-the-wall microwave imaging applications,” *Information*

and Emerging Technologies (ICIET), 2010 International Conference on , vol., no., pp.1,6, 14-16 June 2010.

[131] Yahya Rahmat-Samii and Fan Yang, *Electromagnetic Band Gap Structures in Antenna Engineering*, Cambridge in microwave engineering series, 2008.

List of Publications

Journal Papers

[J1] Elboushi, A.; Ahmed, O.M.H.; Sebak, A.R.; Denidni, T.A., "Study of elliptical slot UWB antennas with a 5.0--6.0 GHz band-notch capability", *Progress In Electromagnetics Research C*, vol. 16, pp. 207-222, 2010.

[J2] Elboushi, A.; Sebak, A., "High-gain hybrid microstrip/conical horn antenna for mmw applications," *Antennas and Wireless Propagation Letters, IEEE* , vol. 11, no. 11, pp.129-132, 2012.

[J3] Elboushi, A.; Sebak, A.R., Denidni, T., "Through wall gap detection using monostatic radar," *Applied Computational Electromagnetics Society Journal (ACES)*, pp. 411-418, May 2013.

[J4] Elboushi, A.; Sebak, A.R., "MMW sensor for hidden targets detection and warning based on reflection / scattering approach," *Antennas and Propagation, IEEE Transactions on*, *IEEE*, 2014, "*In press*".

[J5] Elboushi, A.; Haraz, O.M.; Sebak, A., "High gain circularly polarized slot coupled antenna for millimeter wave applications ", *Microwave Optical Technol. Lett.,* 2014, "*In press*".

Conference Papers

[C1] Haraz, O.M.; Elboushi, A.; Sebak, A.R., "Analysis and design of UWB elliptical slot antennas", *Antenna Technology and Applied Electromagnetics & the American Electromagnetics Conference (ANTEM-AMEREM)*, 2010 14th International Symposium on, pp.1-4, 5-8 July 2010.

[C2] Elboushi, A.; Haraz, O.M.; Sebak, A.; Denidni, T., "A new circularly polarized high gain DRA millimeter-wave antenna," *Antennas and Propagation Society International Symposium (APSURSI)*, 2010 IEEE , vol., no., pp.1-4, 11-17 July 2010.

[C3] Elboushi, A.; Sebak, A., "High gain MMW hybrid antenna using SIW technology," *Electrical & Computer Engineering (CCECE), 2012 25th IEEE Canadian Conference on* , vol., no., pp.1-4, April 29 2012-May 2, 2012.

[C4] Elboushi, A.; Sebak, A., "High gain microstrip fed slot coupled hybrid antenna for MMW applications," *Radio and Wireless Symposium (RWS)*, 2012 IEEE , vol., no., pp.303,306, 15-18 Jan. 2012.

[C5] Elboushi, A.; Sebak, A., "B14. Active millimeter-wave imaging system for hidden weapons detection," *Radio Science Conference (NRSC), 2012 29th National* , vol., no., pp.111-118, 10-12 April 2012.

[C6] Elboushi, A.; Joanes, D.; Derbas, M.; Khaled, S.; Zafar, A.; Attabibi, S.; Sebak, A.R., "Design of UWB antenna array for through-wall detection system," *Wireless Technology and Applications (ISWTA)*, 2013 IEEE Symposium on , vol., no., pp.349-354, 22-25 Sept. 2013.

[C7] Elboushi, A.; Haraz, O.M.; Sebak, A., "Circularly-polarized SIW slot antenna for MMW applications," *Antennas and Propagation Society International Symposium (APSURSI)*, 2013 IEEE , vol., no., pp.648-649, 7-13 July 2013.

[C8] Elboushi, A.; Briqech, Z.; Sebak, A., "4-elements MMW array with EBG feeding network*," Antennas and Propagation Society International Symposium (APSURSI)*, 2013 IEEE , vol., no., pp.162-163, 7-13 July 2013.

[C9] Elboushi, A.; Sebak, A.R.., "High Gain Hybrid DRA / Horn Antenna for MMW Applications ," *Antennas and Propagation Society International Symposium (APSURSI)*, 2014 IEEE , vol., no., pp.1-4, 6-11 July 2014.

[C10] Elboushi, A.; Sebak, A.R.., "High Gain 4-element antenna array for millimeter wave applications ," 2*014 IEEE International Conference on Communication, Networks and Satellite*, Nov. 2014, (Accepted).

Appendix I

EBG-Based Feeding Network and 4-element Array

Although the ease of designing standard Wilkinson power divider as an antenna array feeding network, it is difficult to be employed at MMW frequencies. This can be accounted to high insertion loss and undesired mutual coupling between the output ports, which results in unbalanced output powers. The modified feeding network with EBG, presented in [C8], is originally based on the standard 4-output Wilkinson power divider with optimized curved line edges to reduce the potential radiation at the discontinuity points. In addition, to reduce the mutual coupling between the output ports and suppress the surface waves, a uniplanar EBG structure is optimized to have a bandstop around 30 GHz. The 2D uniplanar EBG unit cell, presented in [131], is chosen to maintain the low profile and small size of the antenna. Fig. A1 (b) shows the dispersion diagram of the uniplanar 2D EBG unit cell. The dispersion curve illustrates a 2 GHz band-gap between the third and fourth propagation modes around 30 GHz.

The optimized EBG unit cells are distributed around both the input and output terminals of the power divider, as shown in Fig. A2. The power divider is designed on 25 mil thick RO6010 substrate with ε_r =10.2, $tan\delta$ = 0.0023. The EBG unit cell dimensions are shown in Table A1.

In order to design an antenna array based on the hybrid element introduced in Section 5.4.4, it found that the cone height is improper to fit the antenna element within an array with a separation distance less than 10 mm (λ_{30GHz}). To overcome this problem, the

hybrid element is re-designed using a shorter mounted horn sacrificing with almost 2dB of gain. The schematic diagram of 4-element antenna array is shown in Fig. A3.

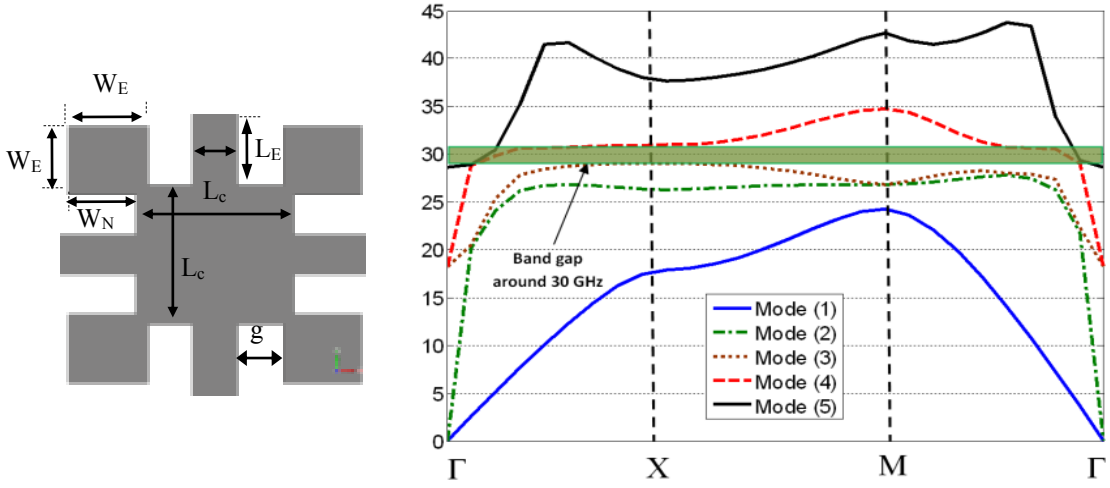

(a) (b)

Figure A1 2D uniplanar EBG unit cell (a) geometry (b) dispersion diagram.

Table A1 Optimized dimensions of EBG unit cell in (mm).

Parameter	W_E	W_N	L_c	L_E	g
Value	*0.4025*	*5.45*	*0.805*	*0.46*	*0.32*

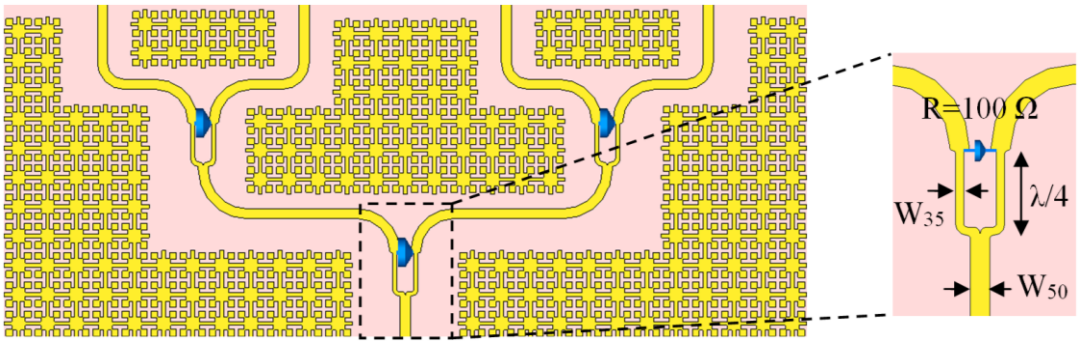

Figure A2 Schematic diagram of the modified Wilkinson power divider with EBG.

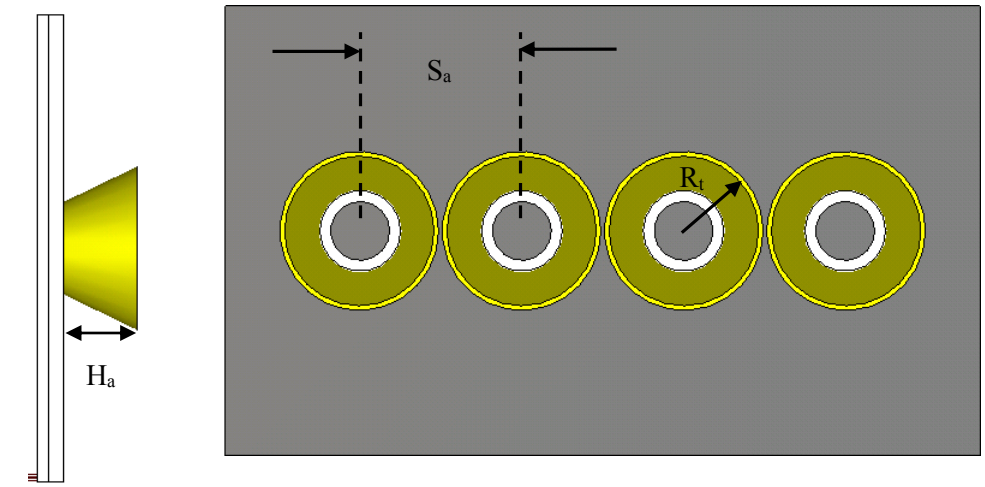

Figure A3 Schematic diagram the proposed 4-elements antenna array (a) side view (b) front view.

The optimized cone height H_a is chosen to be 6 mm, while the top radius R_t =5.5 mm and the separation distance between elements S_a =6 mm. The antenna array integrated with the modified power divider is simulated and optimized using CSTMWS and ADS. As indicated in Fig. A4, adding the EGB unit cells around the power divider has a great effect on stabilizing the power division and enhances the operating bandwidth of the power divider. The insertion loss S_{31} improved from -8.7 dB to -7.5 dB at 30 GHz, while the output port discrepancy enhanced from 0.8 dB to 0.4 dB. There is very small impact on the return loss (S_{11}) of the power divider after and before introducing the EBG. The return loss of the antenna array has almost the same wide bandwidth as the single element, as shown in Fig. A5. The H-plane of the antenna is represented by the yz-plane while the E-plane is represented by the yx-plane. The simulated radiation patterns at 30 GHz for both E and H-plane are introduced in Fig. A6. The antenna exhibits stable broadside radiation characteristics, within the entire operating band. The gain of the antenna array increases by more than 5 dB compared with the single hybrid antenna. In theory the gain should increase

by 6 dB, however, the 1 dB loss can be accounted to the undesired mutual coupling between the antenna elements.

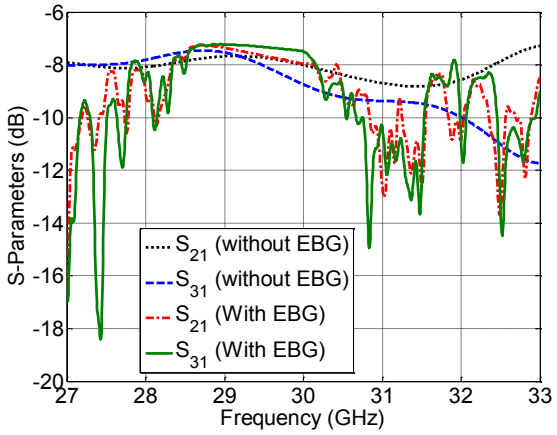

Figure A4 Insertion loss comparison between the power divider with and without EBG.

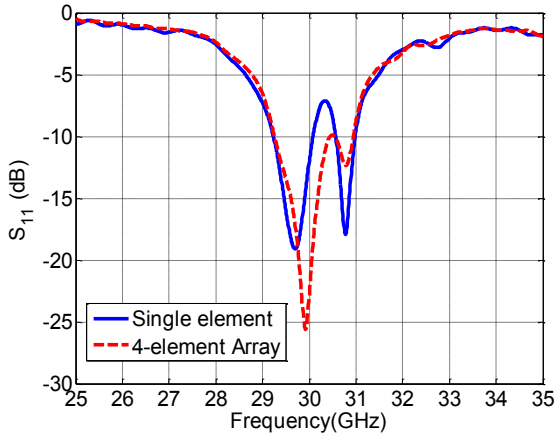

Figure A5 S_{11} comparison between the antenna element and the array configuration.

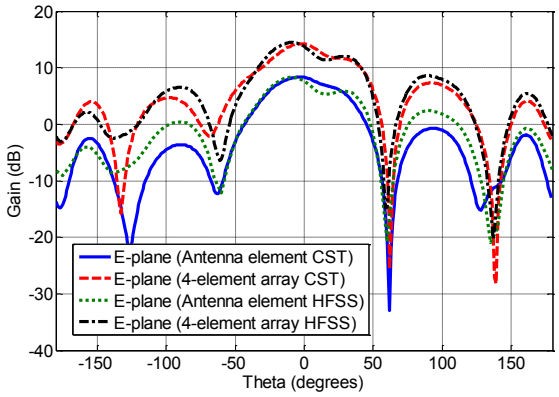

(a)

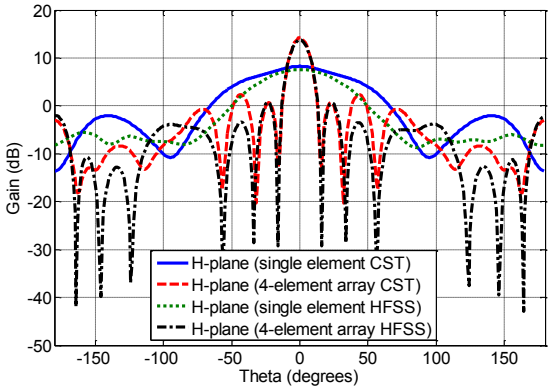

(b)

Figure A6 Radiation pattern comparison between the proposed array and the single element at 30GHz (a) E-plane, and (b) H-plane.